Karlsruher Forschungsberichte aus dem
Institut für Hochleistungsimpuls- und Mikrowellentechnik

Band
20

Julia Hofele

Multi-Physics Modelling towards the Stabilization of PAN Fibers with Microwaves Based on Experimental Data

KIT Scientific Publishing

Julia Hofele

Multi-Physics Modelling towards the Stabilization of PAN Fibers with Microwaves Based on Experimental Data

Karlsruher Forschungsberichte aus dem
Institut für Hochleistungsimpuls- und Mikrowellentechnik

Herausgeber: Prof. Dr.-Ing. John Jelonnek

Band 20

Multi-Physics Modelling towards the Stabilization of PAN Fibers with Microwaves Based on Experimental Data

by
Julia Hofele

KIT Scientific Publishing

Karlsruher Institut für Technologie
Institut für Hochleistungsimpuls- und Mikrowellentechnik

Multi-Physics Modelling towards the Stabilization of PAN Fibers with Microwaves Based on Experimental Data

Zur Erlangung des akademischen Grades einer Doktor-Ingenieurin von der KIT-Fakultät für Elektrotechnik und Informationstechnik des Karlsruher Instituts für Technologie (KIT) genehmigte Dissertation

von Julia Hofele, M.Sc.

Tag der mündlichen Prüfung: 15. Februar 2024
Hauptreferent: Prof. Dr.-Ing. John Jelonnek
Korreferent: Prof. Dr.-Ing. Ralf Moos

Impressum

Scientific Publishing

Karlsruher Institut für Technologie (KIT)
KIT Scientific Publishing
Straße am Forum 2
D-76131 Karlsruhe

KIT Scientific Publishing is a registered trademark of Karlsruhe Institute of Technology.
Reprint using the book cover is not allowed.

www.ksp.kit.edu

Print on Demand 2024 – Gedruckt auf FSC-zertifiziertem Papier

ISSN 2192-2764
ISBN 978-3-7315-1350-6
DOI 10.5445/KSP/1000168942

Foreword of the Editor

Microwave heating is often referred to, when the energy consumption of a process has to be optimized. Microwaves have the advantage to heat directly in the volume, thus compared to conventional heating, not the complete air mass of an oven has to be heated up. Furthermore, microwave heating allows to speed up the heating process, as a finer process temperature control is possible. Those advantages make microwaves an interesting option to use in the production of carbon fibers. Up to date, a significant amount of carbon fibers is produced from polyacrylonitrile (PAN) fibers by using a two stages heating process and large-scale conventional ovens. The stabilization stage takes place at around 200-300 °C considering finely controlled temperature zones due to the exothermic process. The aim of this work is to investigate the first steps towards a microwave assisted stabilization of PAN fibers. Setting up an efficient microwave process starts from understanding the chemical reaction of the material during microwave heating. The in-situ dielectric characterization of the material is thus always the first step. The chemical reactions lead to a change in the dielectric behavior with ongoing reaction progress. Taking this into account, an investigation of the chemical reaction from a dielectric point of view leads to the information on the reaction kinetics. In a process model, the fiber temperature and stabilization degree is calculated, which can be used for the design of an applicator for the microwave heating process. Additionally, the highly temperature dependent chemical reactions are considered in this work. While the process is properly setup, it shows, that, due to the properties of the fiber, a microwave process is only possible in a hybrid heating setting.

Zusammenfassung

Kohlenstofffasern haben gute Eigenschaften für Leichtbauanwendungen, aber ihre Produktionskosten sind immer noch recht hoch, unter anderem wegen des hohen Energiebedarfs und der Materialkosten. Rund 76 % bis 88 % der Gesamtkosten sind die Kosten der verkauften Ware, von denen der Energiebedarf etwa 34 % ausmacht [1] . Eine Möglichkeit, den Energiebedarf zu senken, könnte die Verwendung von Mikrowellen anstelle der herkömmlichen konvektiven Heizung bei der Produktion sein. Ausserdem kann sich die Verwendung von Mikrowellenerwärmung positiv auf die finale Qualität der Kohlenstofffasern auswirken.

In dieser Arbeit liegt der Schwerpunkt auf dem ersten Erwärmungsschritt, der Stabilisierung. Erste Schritte in Richtung einer mikrowellenunterstützten Stabilisierung werden diskutiert.

Zum ersten Mal wurden vollständige in-situ dielektrische Messungen durchgeführt, die die Grundlage für das Verständnis der Herausforderungen bei der dielektrischen Erwärmung bilden. Ein mathematisches Modell, das die Reaktionskinetik mit dem dielektrischen Verlust kombiniert, wird vorgeschlagen. Es erlaubt den dielektrischen Verlust mit dem Stabilisierungsgrad und der Temperatur der Fasern zu verknüpfen. Ein multiphysikalisches Modell der Stabilisierung, das die Mikrowellenerwärmung beinhaltet, wird aufgestellt, um den Einfluss von Prozessparametern wie Lufttemperatur, Fasertransportgeschwindigkeit und Mikrowellenleistung auf die Faser im Vorfeld zu untersuchen. Die experimentellen Ergebnisse werden mit dem Modell verglichen und ausgewertet. Schließlich ermöglicht die Erweiterung eines Streumatrix-Codes eine einfachere Entwurfsoption für zukünftige maßgeschneiderte Applikatoren.

Abstract

Carbon fibers have good lightweight applications properties, but their production costs are still rather high, among other things, due to the high energy demand and material costs. Around 76 % to 88 % of the total costs are the cost of good sold of which the energy demand is around 34 % [1]. One option to decrease the energy demand, could be using microwave heating instead of conventional convective heating during the production. Also, the usage of microwave heating can have a beneficial effect on the final carbon fiber quality. In this work, the focus is on the first heating step, the stabilization. First steps towards a microwave assisted stabilization are discussed.

For the first time, full in-situ dielectric measurements are performed, providing the basis for understanding the challenges encountered with dielectric heating. A mathematical model which combines the reaction kinetics with the dielectric loss is proposed, which allows to connect the dielectric loss to the stabilization degree and temperatures of the fibers. A multi-physics model of the stabilization which contains microwave heating is set up to investigate the influence of process parameters such as air temperature, fiber transportation speed and microwave power on the fiber beforehand. Experimental results are compared to the model and are analyzed. Finally, the extension of a scattering matrix code allows to setup a simpler design option for future custom made applicators.

Table of Contents

Abbreviations and Symbols

Abbreviations

Ar	Argon
ATR	Attenuated Total Reflection
CF	Carbon Fibers
CFRP	Carbon Fiber Reinforced Plastics
CO	Carbon Monoxide
CO_2	Carbon Dioxide
DMA	Dynamic Mechanical Analysis
DSC	Differential Scanning Calorimetry
DUT	Device Under Test
FTIR	Fourier Transformation Infrared
FVM	Finite Volume Method
H_2O	Water
HCN	Hydrogen Cyanide
IA	Itaconic Acid
MA	Methyl Acrylate
N_2	Nitrogen

NH_3	Ammonia
O_2	Oxygen
PAN	Polyacrylonitrile
PANOX	Oxidized Polyacrylonitrile
PID	Proportional Integral Derivative
SMA	Sub Miniature Version A
TGA	Thermal Gravimetric Analysis
VNA	Vector Network Analyzer
WAXD	Wide-Angle X-Ray Diffraction
XRD	X-Ray Diffraction

Operators and Mathematical Symbols

Symbol	Description
Δ	Difference or Change
j	Imaginary unit
ln	Natural logarithm
I	Identity matrix
det	Determinant

Constants

Symbol	Value	Unit	Description
π	3.14159 . . .	-	Pi
e	2.71828 . . .	-	Euler's number, base of natural logarithm
ϵ_0	$8.85418 \cdot 10^{-12}$	$\frac{\mathrm{F}}{\mathrm{m}}$	Vacuum Permittivity
R	$8.31446 \cdot 10^{3}$	$\frac{\mathrm{g\ m^2}}{\mathrm{s^2 mol\ K}}$	Universal Gas Constant
σ_B	$5.67037 \cdot 10^{-8}$	$\frac{\mathrm{W}}{\mathrm{m^2 K^4}}$	Stefan-Boltzmann Constant
p_{01}	2.4048	-	1st Bessel Root of order zero

Latin Symbols and Variables

Large Letters

Symbol	Description
A	Surface area
$A_{C=N}$,$A_{C\equiv N}$	Absorbance peak of FTIR spectra for C=N and C≡N group
A_{cal}	Calibration coefficient for $\varepsilon_r^{'}$
B	Backward traveling wave
B_{cal}	Calibration coefficient for $\varepsilon_r^{''}$
BW	Bandwidth
C_i	Concentration of reactant i (mass related)
D_p	Penetration depth
E	Electrical field
E_a	Activation energy
F	Forward traveling wave
H	Magnetic field
ΔH_{reac}	Specific heat of reaction
L	Length
N	Positive natural number
P_{MW}	Absorbed microwave power
P	Power
Q	Quality factor
Q_{th}	Heat
$\dot{Q}_{th}$	Heat flow
R	Radius
S	Scattering parameters
T	Temperature
V	Volume

Small Letters

Symbol	Description
a	Forward traveling wave
b	Backward traveling wave
$b_{\mathrm{A,B,C}}$	Variable for temperature dependency of ε_r''
$c_{\mathrm{A,B,C}}$	Variable for temperature dependency of ε_r''
c_p	Heat capacity
d	Cavity height or thickness
f	Frequency
$f(\alpha)$	Function of the degree of conversion
k	Rate constant of the Arrhenius equation
k_0	Pre-exponential factor of the Arrhenius equation
m	Mass
r	Radius
r_{th}	Reaction rate
t	Time
$u_{\mathrm{c}}(y)$	Combined standard uncertainty
x_i	Input estimates
x, y, z	Coordinates

Greek Symbols and Variables

Symbol	Description
α_{th}	Heat transfer coefficient
α	Degree of conversion
δ	Diffusion coefficient
$\tan\,\delta$	Dielectric loss tangent
ϵ_{th}	Emission coefficient
ε	Permittivity
ε_0	Vacuum permittivity
ε_r	Relative complex permittivity
$\varepsilon_r^{'}$	Relative dielectric constant
$\varepsilon_r^{''}$	Dielectric loss factor
λ	Wavelength
λ_0	Free space wavelength
λ_{th}	Thermal conductivity
μ	Permeability
ρ	Mass density
σ_{cond}	Electrical conductivity
σ	Uncertainty
ω	Angular frequency

General Indices

Symbol	Description
abs	absorbed
c	cavity
cal	calibration
conv	convective
cond	conductive
diff	difference
exo	exothermic
fib	fiber
hold	holding
i	inner
inc	incoming
liq	liquid
max	maximum value
mean	mean value
MW	microwave
o	outer
rad	radiating
ref	reference
refl	reflected
s	sample
sweep	sweeping
th	thermal

1 Introduction

Carbon Fibers (CF) are increasingly used in lightweight applications as they have superior material properties compared to steel or aluminum [2]. The main advantage of carbon fibers is their low weight to volume ratio but high tensile strength. This makes carbon fibers ideal in applications where a strong but light material is needed [3], for example in cars or airplanes, where a reduction of the weight can lead to fuel savings [4, 5]. Another example is sports equipment, where a lighter boat or bicycle equals to ride faster [6].
Even though carbon fibers were first patented by Thomas Edison in 1880, the interest in carbon fibers began to increase only in the 1950s, and they finally became industrially used starting in the 1960s [3, 5]. Until this day, disadvantages of carbon fibers include the high production costs and the difficulties in recycling [7, 8].
The costs are up to six times higher than for steel which is also due to the high energy amount needed for the carbon fiber production. Although they have superior material properties, steel is still used because of the cheaper production and better recycling capability of the manufactured components [7].
In order to make carbon fibers available for a broader market, a lot of research is ongoing with the goal to reform the carbon fiber production to make it more energy efficient, rise the fiber quality and improve the recycling [7, 8]. In [8], it is stated that energy savings of up to 66 % are possible. Understanding the carbon fiber production to improve the energy efficiency and fiber quality is key and will be explained shortly in the next section.

1.1 Production Stages of Carbon Fibers

Carbon fibers are produced from different starting materials such as pitch, cellulose and Polyacrylonitrile (PAN). Each of those homopolymers have different carbon contents, which also affects the final carbon yield in the carbon

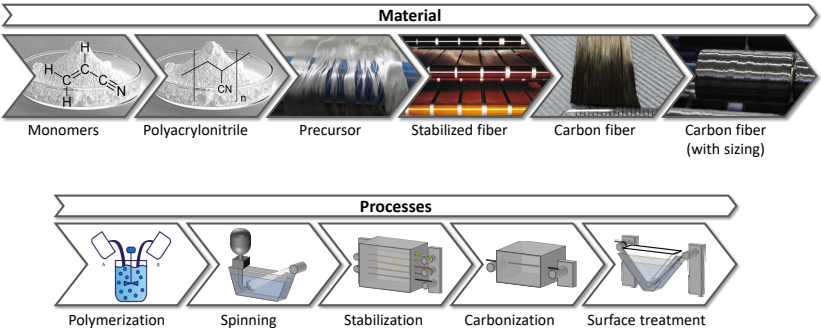

Figure 1.1: Carbon fiber production: material stages and production steps, extended from [9].

fiber. The most common precursor is PAN based, as PAN has a carbon content of already 67.9 %, leading to a higher carbon yield in the final carbon fiber than cellulose based precursors [3]. As this thesis also considers PAN fibers, only the processing of PAN based precursors is described in the following. The change in the material and the process steps leading to the transformation are shown in Fig. 1.1. Each production step influences the final fiber quality which is represented through the fiber modulus and tensile strength [5].

The carbon fiber production starts with the chemical monomers which are transformed into a PAN powder through polymerization. From the powder single filaments are spun, which are then bundled to a fiber. The fiber bundle passes the stabilization stage resulting in a stabilized fiber. The next step is the carbonization in an inert gas atmosphere which results in carbon fibers. Preparing the fibers for further processing e. g. for Carbon Fiber Reinforced Plastics (CFRP) and protecting them e. g. during transport, the final step is a surface treatment which adds a sizing, such as epoxy resins, to the fiber [5].

In the polymerization step, the polymer solution that is mixed defines the chemical composition. The chemical composition influences the later achievable fiber properties as well as the behavior during spinning and stabilization. Often comonomers are added to the chosen homopolymers such as PAN. Their beneficial effects on the spinning process are to enhance the flow properties of the polymer solution, which is important for the spinning step [5]. Also the stabilization process profits from the use of comonomers, such as lowering the

starting temperature of the chemical reactions [3]. In the case of PAN fibers, the comonomers Itaconic Acid (IA) and Methyl Acrylate (MA) are successfully lowering the exothermic reaction heat. Only about 2-10 % of the fiber should be comonomers so that a carbon yield of 50-60 % can be reached [5].

Different spinning techniques are available such as melt, dry, air gap or wet spinning. For PAN fibers, wet spinning is the most used technique, although it gets more and more replaced by air gap spinning [3].
Wet spinning needs a solvent bath with different chemicals to allow the fiber to coagulate, which increases the costs for production and recycling of the chemicals. After the spinning the filaments are washed, stretched and dried. The stretching is needed to align the molecule chains. It reduces the final fiber diameter [3]. In general a single filament has a diameter of about 11 μm and a density of 1.18 g/cm^3. It is then arranged to form a fiber bundle with multiple thousand filaments, which is the so called precursor for the following production steps. Commercially there are bundles available consisting of e. g. 1000 filaments (1k fiber), 3000 filaments (3k fiber), 12000 filaments (12k fiber) [3].

The fiber is going on to the stabilization process, called oxidation, which prepares the fiber for the carbonization. In this stage the fiber is heated up in large scale conventional heating ovens to temperatures around 200-300 °C. Different heating profiles are generally possible. Usually, the fiber is heated up carefully by multiple heating zones with increasing temperatures over one to two hours in order to control the chemical reaction. Three main reactions take place: dehydration, cyclization and oxidation. All of them are exothermic reactions. They change the ladder-polymer to a cyclic structure which is more heat resistant for the next processing step. The stabilization stage will be explained in more detail from a chemical perspective in Chapter 1.1.2.
During the stabilization, chemical and physical shrinkage occur due to the higher mobility of the polymer chains in the material. The physical shrinkage is controlled throughout the oven by stretching the fiber [3, 5, 10].
The chemical reactions lead to the production of gases such as Ammonia (NH_3), Hydrogen Cyanide (HCN), Water (H_2O), Carbon Dioxide (CO_2) and Carbon Monoxide (CO). As some gases are explosive, such as HCN, CO, NH_3, an air exchange is necessary to ensure a safe working space [3]. The density changes to 1.36-1.4 g/cm^3 through the stabilization. When the fiber reaches an oxygen content of 6-12 %, it is ready to go on to the next production step [3].

The carbonization process removes some of the left over elements in the fiber, to increase the carbon content further. The carbonization stage is carried out in an inert gas atmosphere such as Nitrogen (N_2) or Argon (Ar) to avoid any further oxidation. It is often divided in a lower temperature stage around 700-1000 °C and a high temperature stage with up to 1500 °C The fiber passes each stage for a few minutes up to less than an hour [3, Ch.5.8]. The low temperature carbonization removes tar, while the high temperature carbonization increases the fiber modulus. Chemical reactions, such as dehydrogenation and denitrogenation, form a crystalline oriented structure. Again the shrinkage is controlled during the process [3, 5].
The final carbon fiber is electrically conductive and has a diameter of around 5-7 μm and a density around 1.8-1.9 g/cm^3 [11]. Depending on the starting material carbon contents of over 90 % can be achieved [3].

The carbon fiber production is finished with a surface treatment of the fiber to ease the handling and roughen the surface for easier binding with the resin utilized in carbon fiber composites. The treatment can be done by e. g. plasma, electrochemical oxidation, wet chemical or thermal application. Resins are needed to bring the carbon fibers in the final form of the component and harden it in the defined shape, also called curing. Thermosetting and thermoplastic resins are distinguished. Thermosetting refers to the irreversibility of the curing, such as epoxy, polyester, polyimide and vinyl ester resins. Thermoplastic resins can be reused as these can be reheated. Examples are polyethylene (PE), polyetheretherketone (PEEK), polycarbonate (PC) and polypropylene (PP) resins [3, 5, 12].

1.1.1 Energie Consumption of Carbon Fiber Production

In 2016 Ellringmann et al. summarized the carbon fiber production costs of different companies and set up a cost model over the all production stages [1]. Around 76 % to 88 % of the total costs are the cost of good sold according to the manufacturers. The highest costs are due to the energy demand which the model calculated to 34 % of the overall production costs, divided in 16.2 % for the production of the precursor and 17.8 % in the conversion of the stabilization and carbonization process [1]. Thus, concerning energy savings, no more than those 17.8 % can be reduced.

In 2017, a report was released by the U.S. Department of Energy concerning the potential energy saving opportunities of carbon reinforced polymer composites based on data from the US in 2010 [8]. The oxidation and carbonization are considered as one process step with regards to the energy consumption.
In [8], the current typical, the state of the art and the practical minimum energy intensities are explored. The state of the art energy consumption refers to the minimum energy level which can be reached based on the application of the best available technologies worldwide in a single processing line. The practical minimum energy consumption can be reached with improvements from research and development departments. Also it is distinguished between on-site energy and primary energy. The on-site energy is only consumed within the manufacturing plant, whereas the primary energy also includes the offsite consumed energy.
The report states, that the current typical energy consumption, thus industrially applied, is about 427 MJ/kg primary energy and 195 MJ/kg on-site energy [8]. The state of the art level with around 237 MJ/kg primary energy and 108 MJ/kg [8]. According to the report, the practical minimum is around 142 MJ/kg primary energy and 33 MJ/kg [8]. This report shows that from the current typical to the practical minimum energy consumption, energy savings of up to 66 % are possible.

In [13], Sunter et al. present a case study on replacing a conventional steel door of a car with a 50 % composite from carbon fiber and epoxy. They specify in [13] the current typical energy content with 1134 MJ/kg and the practical minimum energy content with 330 MJ/kg for the carbon fiber production. They conclude that a 13 % reduction in the current energy demand would lead to cumulative life cycle energy advantages compared to steel. In comparison, Fruehan et al. state in [14] for liquid steel a practical minimum of 8.2 MJ/kg and actual requirements of around 11.5 MJ/kg. The steel production is thus cheaper in costs, which results in the need for reduced production costs of carbon fibers.

Various options are already being explored, such as increasing the energy efficiency of the conventional ovens or optimizing the materials or process parameters. Another way is using new and innovative technologies altogether, such as microwave heating or plasma heating. Microwave heating is known to improve the efficiency of industrial processes as it allows to heat directly in the volume instead of heating up large air masses. The power can be controlled

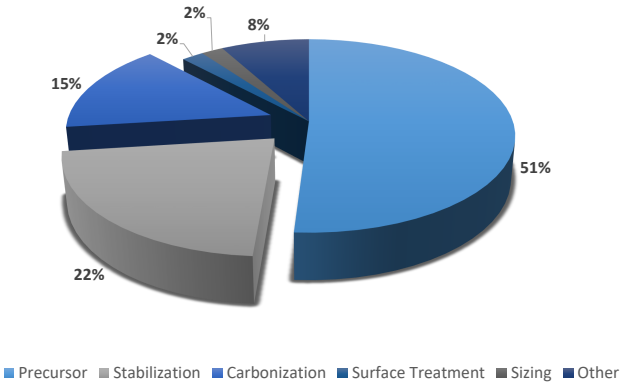

Figure 1.2: Breakdown of production costs for PAN based carbon fiber, adapted from [3, Fig.5.5].

faster than in conventional ovens [15]. According to [3] the stabilization needs around 22 % of the costs while the carbonization takes up 15 % of the costs, see Fig. 1.2.

In this thesis the focus is thus on the exploration of the needed knowledge to use microwave heating as alternative to conventional heating in the stabilization stage, as it is the most time consuming production step [4] and thus leads to higher costs than the carbonization [3]. Also the stabilization can have a large influence on the final carbon fiber properties [16].

1.1.2 Stabilization of PAN Fibers

During the stabilization stage, the precursor is heated up to a temperature between 200 °C and 300 °C, where three main chemical reactions are taking place and form the inflammable fiber which allows the fiber to be heated in the carbonization stage up to 1000 °C. The precursor most commonly used is a copolymer with 95 % PAN and the comonomers MA and IA [3].
The reactions taking place are dehydration, cyclization and oxidation. The dehydration and cyclization are taking place simultaneously whereas the oxidation starts later. The order of reactions and how they change the chemical

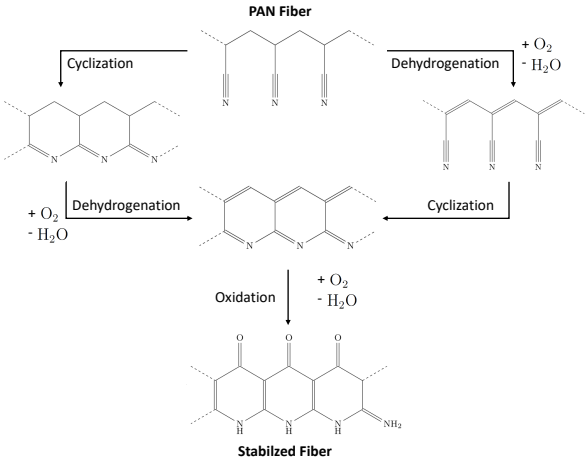

Figure 1.3: Chemical reaction flow during the stabilization stage.

structure can be seen in Fig. 1.3. All of them are exothermic reactions and thus add extra heat when the fiber is heated [10].

The cyclization is the only reaction that can also take place without oxygen. But Badii et al. [17] credit oxygen a catalytic effect on the cyclization. The cyclization breaks the C≡N bonds into C=N bonds which leads to the desired ladder structure. The dehydration forms C=C groups instead of C-H_2 groups. The oxidation is breaking up the C-H_2 groups and forming C=O groups. Oxygen is needed for the reaction as it reacts with the free hydrogen to water. The reduction, the reverse reaction of the oxidation, is added also by Badii et al. [17]. The reaction equations used in this work are based on the ones stated by Badii et al. [17]:

$$\text{Cyclization: (-C} \equiv \text{N)} \overset{O_2,k_1}{\rightarrow} \text{(-C=N-)} \tag{1.1a}$$

$$\text{Dehydration: 2(-CH}_2\text{)} + O_2 \overset{k_2}{\rightarrow} \text{(-C=C-)} + 2H_2O \tag{1.1b}$$

$$\text{Oxidation: (-CH}_2\text{)} + O_2 \overset{k_3}{\rightarrow} \text{(-C=O)} + H_2O \tag{1.1c}$$

$$\text{Reduction: (-C=O)} + H_2O \overset{O_2,k_4}{\rightarrow} \text{(-CH}_2\text{)} + O_2 \tag{1.1d}$$

Based on eq. 1.1 the following reaction rates r for the different species are derived [17]:

$$r_{C\equiv N} = -k_1 C_{C\equiv N} C_{O_2} \tag{1.2a}$$

$$r_{C=N} = k_1 C_{C\equiv N} C_{O_2} \tag{1.2b}$$

$$r_{C=C} = k_2 C_{CH_2} C_{O_2} \tag{1.2c}$$

$$r_{C=O} = k_3 C_{CH_2} C_{O_2} - k_4 C_{C=O} C_{O_2} \tag{1.2d}$$

$$r_{CH_2} = -k_2 C_{CH_2} C_{O_2} - k_3 C_{CH_2} C_{O_2} + k_4 C_{C=O} C_{O_2} \tag{1.2e}$$

$$r_{O_2} = k_4 C_{C=O} C_{O_2} - k_2 C_{CH_2} C_{O_2} - k_3 C_{CH_2} C_{O_2} \tag{1.2f}$$

Resulting from eq. 1.1a, eq. 1.2a and 1.2b are only dependent from each other, meaning C ≡ N is reduced with the rate constant k_1 while C=N is built with the same rate constant. The other reaction rates have multiple terms and thus are dependent on multiple species. This leads to a more complex reaction mechanism and only the cyclization can be separated from the other reactions. In Table 1.1, the values for the kinetic parameters, according to Badii et al. [17], are shown and the calculated released heat for each reaction as well [18]. The reaction kinetic parameters comprise the pre-exponential factor k_0, which influences the speed of reaction and the activation energy E_a, which gives the level of energy which needs to be achieved for a reaction to take place [19, 20]. The prefix of the heat of reaction shows if it is an exothermic or endothermic reaction. If it is an exothermic reaction, heat is released which is marked by a negative prefix [20, 21]. The table shows that the oxidation starts later than the other exothermic reactions but takes place faster and is adding more energy to the process.

Reaction	E_a in J/mol [17]	k_0 in m^3 / (kg s) [17]	ΔH_{reac} in J/mol [18]
Cyclization	$81.59 \cdot 10^3$	$6.85 \cdot 10^6$	$-1.7 \cdot 10^4$
Dehydrogenation	$81.59 \cdot 10^3$	$3.69 \cdot 10^6$	$-1.18 \cdot 10^5$
Oxidation	$126.73 \cdot 10^3$	$2.40 \cdot 10^{11}$	$-4.04 \cdot 10^5$
Reduction	$40.96 \cdot 10^3$	$8.86 \cdot 10^1$	$4.04 \cdot 10^5$

Table 1.1: Kinetic parameters for the reaction rate coefficients adapted from Badii et al. [17] according to [18] and released heat of reaction calculated following [18].

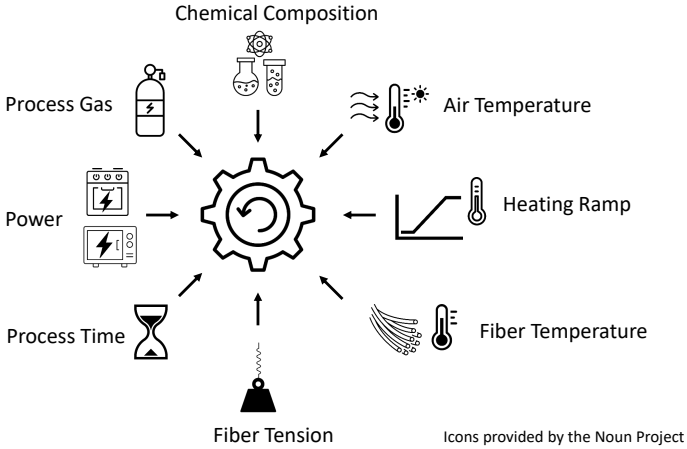

Figure 1.4: Influencing factors on the stabilization process.

There are multiple influential factors on the stabilization process, which are visualized in Fig.1.4, showing the complexity of the stabilization process. They also change the grade of the stabilized fiber and thus later the carbon fiber in the following ways [3, 5]:
The chemical composition is influencing the starting temperatures of the chemical reactions and the final carbon content. The process gas and atmosphere control can have an effect on which reactions take place as well as the final carbon content. When the excess heat from the exothermic reaction is not handled, the fiber temperature can increase too much and the fiber is burnt.

The choice of heating can also influence the process. The skin core structure with microwave heating differs from the conventional one, as the reactions can start in the center of the fiber [22]. The applied fiber tension is of interest, as the fiber becomes soft when heated and first elongates before shortening due to physical and chemical shrinkage [10]. The applied fiber tension influences the shrinking process and thus the final fiber diameter. In the case of hybrid heating, here a combination of conventional heating and microwave heating, the air temperature is also influencing the process. Through the hybrid heating a better temperature control can be achieved as the air flow can be used to heat or cool the fiber [3, 5].

With all those influences, it becomes clear that the stabilization process has many options to influence the fiber quality. For this reason, the knowledge of a stabilization degree is helpful to determine the final fiber quality which can be used as reference for process optimization.
In [3] the most commonly measured quantities of the stabilized fiber giving information on the process are stated as:

- O_2 content,
- density,
- hygroscopy,
- chemical shrinkage,
- stabilization degree.

1.2 State of the Art

The use of microwave and plasma heating in the carbon fiber production process got already an increasing interest in the last couple of years. In the following, the focus will be only on publications and patents concerning the stabilization stage with microwave heating or microwave induced plasma heating or modeling of the stabilization stage. Some patents are published in multiple countries, but they will be referred to only once. Also a short overview of the different measurement methods, used to determine the fiber quality or the stabilization degree, will be given.

Patents

In the patent US6375875B1 [23] by UT-BATTELLE, LLC, Oak Ridge from 2002 Paulauskas et al. proposed a method to monitor the dielectric properties of the fiber during the carbon fiber production process by using a resonant cavity. The invention is able to differentiate between different material compositions, moisture levels and material qualities.

In 2009, patent RU2343235C1 [24] outlined the usage of microwave radiation on the fiber precursor as preparation step before applying plasma heating for the stabilization. They used a non equilibrium plasma in the low temperature range, but did not define it further.

The patent EP2475812B1 [25] by Toho Tenax Europe GmbH from 2012 used an applicator with variable electric field strength in the range of 3 to 150 kV/m. A process gas can be heated in the range of 150 to 300 °C and introduced into the cavity. A fiber consisting of minimum 85 % PAN and comonomers such as vinyl acetate, acrylic acid methyl ester, vinyl chloride, styrene or itaconic acid are used. The patent stated that the presented applicator can be used to stabilize the fiber to a certain degree or finish the stabilization of already pre-stabilized fibers. The example applicators have lengths of 1 m and more.

In the patents US7534854B1 [26] from 2009, US7786253B2 [27] from 2010 and US20150252501A1 [28] from 2015 by UT-BATTELLE, LLC, Oak Ridge, plasma heating is used to stabilize the fibers or at least expose the fiber to the oxidative species. A suitable applicator is proposed and tested. The plasma source for the tested applicator is a microwave power source to sustain the vacuum plasma. But also other energy sources for the plasma are discussed as well as atmospheric plasma.

In 2014, EP2460915B1 [29] proposed an applicator with heated walls in combination with an oxidizing oxygen containing gas and a microwave irradiation of 10 W. For the experiments a 1.5 m long cylindrical waveguide is used with microwave power levels between 10 W to 1 kW at a frequency of 2.4 GHz.

Papers on fiber processing

In 2004 Paulauskas and White presented a measurement system based on a rectangular cavity using the TE_{011} mode to gather data on the temperature dependency of PAN fibers during the stabilization. A hot air flow is used to heat the fiber inside the cavity. The temperature was increased from 25 °C with heating rates from 2 ° to 4 °C up to 250 °C. No information was provided on the effect of higher temperatures or the final stabilization degree. The holding time during the process temperature and the cooling down were not recorded [30].

In the same year Paulauskas, Warren and Carpenter published a report on atmospheric pressure plasma as method to stabilize PAN fibers. The influence of different process gases was investigated. The results show that a more homogeneous stabilized cross section of the fiber while having lower densities is achievable. They also stated that the color change to black occurs after the fiber is about 10-20 % oxidized, so that color is only a progress indicator in the early oxidation. The time of the oxidation could be reduced trough the plasma treatment [31].

In 2009 Paulauskas et al. gave an overview of their research which tackles multiple optimization areas of the carbon fiber production. They presented a low cost precursor. They stated that they can reduce the stabilization time from 90-120 minutes (min) to 35 min with various techniques such as microwave radiation or plasma treatment. The plasma processing reduced the stabilization time by the factor three compared to conventional heating with a line speed of 0.3 m/min [4].

In 2011 Lee et al. showed the influence of radio-frequency plasma treatment on pre-stabilized fibers. Although the fibers could be stabilized further with the plasma treatment, it also damaged the surface of the final carbon fiber [32].

In 2013 Lee et al. presented another paper on plasma assisted stabilization. This time the mechanical properties, here the tensile strength, were higher when plasma treated during the stabilization. As atomic oxygen was predominant in the plasma atmosphere, which is smaller than diatomic oxygen, it diffuses faster into the fiber filaments. This shortens the time needed for the oxidation. The degree of cyclization was adopted to define the extent of reaction. It was the same for a plasma treated fiber for 15 min and a conventionally treated one for 120 min [33].

In 2018 Zhang et al. [34] and Liu et al. [22] presented a comparison between the effects of microwave and conventional heating on the stabilization. In [34] the fibers are heated from room temperature up to 180 °C with multiple heat rates. The fibers are winded around a ceramic rod and placed inside a tubular microwave oven. Dielectric properties are not provided neither for the fibers nor for the ceramic rod. Without that information, it can be assumed that the microwave was heating the ceramic rod. Hence, the fibers were heated via thermal conduction. Depending on the temperature dependent dielectric loss it is possible that the fibers are microwave heated once a threshold value is surpassed. Multiple methods are used to investigate the microwave heating influence on the fiber properties. For example, the surface topography analysis shows the smoother surface of microwave processed fibers. It is explained with the reaction taking place from inside to outside, resulting in a constant and thus more smooth transformation [34].
In [22] a shortening effect of the microwave heating in process time by 35 min and process temperature by 30 °C was achieved. The fibers were again tied to a ceramic rod. The temperatures were elevated up to 240 °C for the microwave stabilized and 270 °C for the conventional heated fibers. No information on the temperature measurement method was provided. The cross section has been investigated into more detail and it is stated that the skin-core structure usually to be found in conventionally produced fibers, is not able to form thus leading to a more homogeneous skin-core structure through the volumetric heating effect [22].

Soulis et al. presented in 2020 a review of the current research state for different alternative strategies for PAN based carbon fibers and their effect on the mechanical properties. The goal was to determine which factors can be influenced to reduce the costs with the same mechanical properties. The focus is mainly on microwave plasma in the carbonization stage to reduce the treatment duration and energy consumption [35].

In 2021 Zhao et al. presented the reaction mechanism and fiber structure of PAN based raw silk fibers with conventional and microwave heating. The fibers are passed through several heating zones and samples are extracted after every zone. Microwave heating is only applied in the last zone of each batch, so that in general pre-oxidized fibers are used. The findings show an overall lower temperature for the starting of the reactions and a reduction of the surface defects for microwave heated fibers [36].

In 2021 Chao et al. presented the dielectric properties of the PAN precursors, stabilized fibers and carbonized fibers. They are measured from two different companies. Although the densities of both fibers were in a similar range, the dielectric properties showed a bigger difference between the two companies [37].

Papers on modeling

An important step to improve the stabilization process is the application of appropriate theoretical models for the stabilization process to avoid costly and lengthy experiment.
In 1991 Dunham and Edie proposed a first heat transfer model to calculate the fiber temperature. The bundle of multiple filaments was modeled as homogeneous filled cylinder with effective properties. The three main reactions were also included in the model. Additionally the reaction kinetics were derived from a number of experiments. The insights gained by the model and validating experiments lead to an optimized temperature profile inside an oven that reduces the process time and leads to more controlled exothermic reactions [38].

In 2009 Das et al. gave an overview on microwave heating applications, with a focus on ceramics, such as drying, sintering, plasma processing, fiber drawing, melting and synthesis. The difficulties and basic modeling approaches regrading microwave heating were discussed. Das et al. concluded that further research is necessary to understand the microwave-material interaction better [39].

In 2015 Khayyam et al. compared multiple dynamic prediction models for the heat of reaction and the mechanical properties. Data was first gathered by Differential Scanning Calorimetry (DSC) and Dynamic Mechanical Analysis (DMA) analyses and used as model input parameters. A Taylor polynomial method lead to the best results [16].

In 2018 Badii et al. presented an extended model which not only takes three main reactions into account, but adds a fourth: the reduction reaction of the C=O group. It is stated that due to the changing chemical composition of PAN e. g. through adding various comonomers, the old model from Dunham

and Edie [38] is not complete any more. For this reason, oxygen is added as catalyst in the cyclization and the reduction reaction [17].

In 2019 Khayyam et al. gave an overview on published models regrading the stabilization with PAN fibers. The overview includes models on reaction kinetics and heat transfer models. No information on models regarding microwave heating are provided [40].

In 2021 Terra et al. showed that through neural networks a good simulation of the stabilization stage could be obtained. The authors investigated which process parameters are most appropriate for the control of the fiber quality and selected the volumetric density and the Fourier Transformation Infrared (FTIR) conversion index [41].

Methods for quality determination

Different methods are available and used for the evaluation of the fiber properties. They give insights in the fiber quality, the stabilization degree and are used to optimize the influence of different process parameters on the fiber [3]. The fiber quality after the stabilization is important as it influences the final carbon fiber quality [42]. Some of the proposed methods are:

- Fourier-transform infrared spectroscopy (FTIR):
  The measurement of the absorbance spectrum is able to provide information on different chemical bonds. It is used to define a stabilization degree. Often the cyclization or dehydration index is used. Also it can give information on the reactions mechanisms through the functional groups of interest [17, 32–34, 36, 41, 43, 44].
- Differential scanning calorimetry (DSC):
  It is used to determine the heat of reaction through comparison of the heat flow from the sample and a reference. Through the heat of reaction the stabilization degree can be evaluated [16, 17, 33, 38, 43–45].
- Dynamic mechanical analysis (DMA):
  It is used to measure the fiber tension level [16].

- Density measurements:
  The density is an indicator if the fiber is stabilized enough to go on to the carbonization [34, 36, 41].
- Thermal gravimetric analysis (TGA):
  It is used to track the weight loss during thermal treatments [44, 45].
- X-ray diffraction (XRD) and wide-angle X-ray diffraction (WAXD):
  The crystallinity can be measured and structural changes detected [34, 36, 42, 44, 45].

Other tools providing information are the color or shrinkage of the fiber [46–50]. In [31], it is stated that the fiber is black after it is about 10-20 % oxidized. In [45] the color change is an indicator for an earlier reaction of two different precursors, similar to [44] which states that the color change is evidence that the reactions took place.

Some papers outline the benefits of plasma heating on the stabilization stage. However, fewer papers describe the influences that microwave heating has on the stabilization process. For this reason, the focus in this work is on microwave heating.
Although some measurements on the dielectric properties of PAN fibers are published, the data is not sufficient for the design of a microwave applicator for the stabilization as each individual chemical compositions affects the dielectric behavior. Furthermore, no data for the complete reaction is available. So far, except for the results presented in the patent [23], the dielectric properties have not been used in combination with PAN fibers neither as a tool for the determination of the degree of stabilization nor the reaction kinetics. In the modeling of the stabilization with PAN fiber, the influence of microwave heating has so far not been considered. A detailed analysis on the applicator design for the stabilization with PAN fibers could not be found in literature.

1.3 Objective of this Work

So far only limited knowledge on the dielectric heating of PAN fibers is available. For the first time, here a systematic analysis of the stabilization process of PAN fibers with microwave heating for the carbon fiber production is per-

formed as part of this thesis.
For the stabilization of PAN fibers with microwaves, three heat sources have to be taken into account: the reaction heat, the heat induced by microwaves and the heat transfer, which also includes conventional heating. Understanding how the microwave heating affects or behaves in each step is key to setting up a successful process. The objective of this work is to show methodically the impact of microwave heating in combination with the other heat sources in the stabilization stage. Part of the research was conducted in the scope of the project REINFORCE (ZF4204603SY7) which was funded by the Federal Ministry for Economic Affairs and Energy of Germany. The project partner KCTECH provided the utilized fiber in this work.

For the successful design of an appropriate dielectric heating system, the knowledge of the temperature-dependent dielectric properties of the raw material and the change during the chemical transformation are mandatory. It is required for the determination of the response to microwave heating, and gives first information on the design of an appropriate heating system. Thus, the first objective is the measurement of the temperature-dependent dielectric properties during the course of the stabilization reaction.

Additionally, the understanding of the reaction kinetics is a key element to be able to control the exothermic behavior during the process. The second objective is to understand the reaction kinetics from a dielectric point of view. This novel approach also allows for the first time to gather information on the final fiber quality depending on the dielectric properties. The knowledge gained can be used for microwave heating, and it is utilized for a simple online quality control tool.

The next step towards the microwave assisted stabilization is to collect information on the needed process parameter ranges, which can be done by simulation. This is a helpful step to investigate the process stability and avoid thermal runaways, thus overheating and destroying of the fiber. The third objective is to setup a multi-physics model which allows to calculate the fiber temperature based on the mentioned heat sources. The model enables a theoretical optimization of the process before running any experiments, so that the process parameter ranges needed can be kept in mind when the equipment for the experiments are chosen.
The insights gathered from this objective are also tested experimentally to provide even further insights in the practical approach.

Next an applicator which is suitable for the microwave assisted stabilization is needed. A linkage of the multi-physics model with a code to calculate stepped resonators provides the necessary tool. The last objective is to provide the optimization setup to plan an appropriate applicator for a desired heating profile.

In Chapter 2, the methods for the measurement of the dielectric properties and reaction kinetics are presented. The measurement systems to determine the in-situ temperature dependent dielectric properties during the complete stabilization stage and for the continuous processing are introduced. Finally, the setup for the mathematical model is given.

In Chapter 3, the results of the first in-situ measured dielectric properties of the stabilization with PAN fibers are shown. Also, the results obtained with the complete multi physics process model, to describe the thermal development during stabilization stage and thus allowing to do fundamental simulations before starting any experiments, are given. The results of the continuous process are displayed.

In Chapter 4, the connection of the reaction kinetics with the dielectric properties is discussed and the extracted reaction kinetics parameter are used in a pioneering reaction model. The different methods to obtain the stabilization degree are also examined.

Finally, in Chapter 5, the process model is used in combination with an extended matrix scattering code to design and optimize a new applicator allowing to stabilize the fiber through microwave heating.

2 Materials, Methods and Experimental Setups

2.1 Materials

2.1.1 PAN Precursor

The PAN precursor is provided by KCTECH, Korea. It consists of 3000 (3k) filaments. They are composed of 95 % Polyacrylonitrile with a 5 % mixture of the comonomers MA and IA. For the experiments, the fibers are bundled again to a 12k fiber.

2.1.2 Further Materials

A quartz tube, with an inner diameter of 8 mm and an outer diameter of 10 mm is chosen and modified to decrease in diameter at one side. For this customized quartz tube, a tube with a diameter of 8 mm is melted together with a decreasing diameter transition to a tube with an inner diameter to around 6 mm. Also a side stub, with an inner diameter of 4 mm, is added through which the air is introduced. The material parameters used in this thesis for air and quartz can be found in Table 2.1.

Parameter	Air	Quartz	Unit
Thermal conductivity λ_{th} at 20 °C	0.026	1.318	W/(m K)
Density ρ	1.19	2200	kg/m^3
Heat capacity c_p	1000	750	J/(kg K)
Emission coefficient ϵ_{th}	-	0.93	-

Table 2.1: Material parameters for air and quartz [18, 51, 52].

2.2 Methods

2.2.1 Fundamentals on Dielectric Properties

For the interaction with an electromagnetic wave, three material properties are important to know as they influence the interaction mechanism that will take place: permittivity ε (dielectric), permeability μ (magnetic) and conductivity σ_{cond}. If an electromagnetic wave interacts with non-conducting materials the result will be a polarization inside the material [53]. Different polarization mechanisms exist but the most relevant one for dielectric materials are the electrical polarization mechanisms. Broadly they can described by a displacement of electron, ions or orientation of dipoles inside the material due to an applied electric field [53, 54].

The electron polarization describes the displacement of the positive atom nucleus from their center position. On the material surface appears a so called polarization charge. Similarly the shift of positive ions in electric field direction and negative ions in the opposite direction is called Ion Polarization. The third electric polarization mechanism is the orientation polarization. It can only take place when the material consists of molecules with a permanent dipole. Usually, without the electric field, the randomly distributed dipole moments chancel each other out, so that no polarization is noticed on the material surface. The electric polarization is usually proportional to the electric field strength. Due to the different mass of the particles, the frequency of the electric field has an impact on which polarization mechanisms are responding faster to it [15, 53, 54].

If an electric field is applied to a dielectric material, its polar molecules align to the field. As electromagnetic wave is changing the orientation, the particles rotate to follow the field. This forced spin of the molecules leads to friction losses inside the material which generates heat [15, 53].
The permittivity which quantifies the electrical polarization is defined as [55]:

$$\varepsilon = \varepsilon_0 \cdot (\varepsilon_r^{'} - j\varepsilon_r^{''}) \tag{2.1}$$

where ε_0 is the permittivity of vacuum and $\varepsilon_r^{'}$ the relative dielectric constant describing how much energy can be stored in the material through polarization. The loss factor $\varepsilon_r^{''}$ defines how much energy can be converted into heat. Together they are referred to as dielectric properties.

The ratio of $\varepsilon_r^{''}$ to $\varepsilon_r^{'}$ is defined as loss tangent [15]:

$$\tan\delta = \frac{\varepsilon_r^{''}}{\varepsilon_r^{'}} \tag{2.2}$$

Dielectric Heating

The temperature and frequency-dependent dielectric properties of a material are the most important information needed when interaction with microwaves is taking place. In a constant electric field, the power absorbed inside the material is given by [53]

$$P_{\mathrm{MW}} = \omega \cdot \varepsilon_r^{''} \cdot \varepsilon_0 \cdot |E|^2 \cdot V \tag{2.3}$$

where ω is the angular frequency, $\varepsilon_r^{''}$ the dielectric loss, ε_0 the vacuum permittivity, $|E|$ the effective electric field strength and V the volume. As the dielectric properties can vary for different temperatures and frequencies, it is helpful to measure the dielectric properties of the material beforehand for the desired temperature range and at the chosen frequency.

The heating efficiency, thus how well the electromagnetic energy is absorbed inside the material and transferred to heat, is determined by the dielectric loss and it is also influenced by the penetration depth. The penetration depth defines how far the electromagnetic wave can pass through the material. The distance

at which the power level is reduced to $1/e$ of its initial value, where e is the Euler's number, can be estimated as follows [15]:

$$D_{\mathrm{p}} = \frac{c}{4\pi f} \sqrt{\frac{2}{\epsilon_r' \left(\sqrt{1 + (\frac{\epsilon_r''}{\epsilon_r'})^2} - 1 \right)}} \tag{2.4}$$

where c is the speed of light in free space. It is thus dependent on the chosen frequency and the dielectric loss of the sample material. Eq. 2.3 and eq. 2.4 show although lower frequencies lead to higher penetration depths, the lower energy conversion can make it necessary to go to higher frequencies e. g. for smaller samples [15].

Thermal Runaway Effect

The influence of the dielectric loss factor can lead to a thermal runaway effect. When more microwave power is absorbed in the material due to an increase in the loss factor with higher temperatures it gets easier for the microwaves to be absorbed in this spot [15].
Fig. 2.1 shows a flow chart of a hybrid heating system with microwave power P_{MW} and conventional heating. The conventional heat transfer and losses are represented by $\dot{Q}_{\mathrm{conv}}$. Optionally the heat flow from an exothermic reaction $\dot{Q}_{\mathrm{exo}}$ can get added (see dashed lines). Together they sum up to change the fiber temperature ΔT_{fib} over time. The higher temperature results in an increase in the dielectric loss, which then makes it easier to add more heat through microwave heating. At one point the activation energy of the reaction is reached and the exothermic reactions start to add another heat flow $\dot{Q}_{\mathrm{exo}}$ resulting in a higher temperature increase which then leads to an even bigger change in the dielectric loss. The underlying equations are explained in more detail in Chapter 2.4.

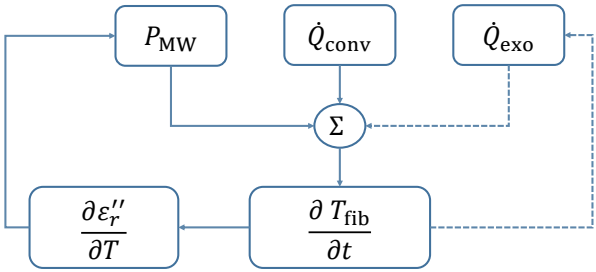

Figure 2.1: Temperature increase due to microwave heating and exothermic reactions which can lead to a thermal runaway effect.

2.2.2 Measurement of Dielectric Properties

Perturbation Method

As shown in eq. 2.3, the dielectric loss ϵ_r'' is needed in order to calculate the energy absorbed by microwaves inside a material. This material property is not always given in literature for the desired frequency range or aggregate state of the material. Hence, it needs to be measured. In [30], Paulaskas and White did measure the dielectric properties during the heating-up stage, but not during the full chemical reaction. The chemical composition of the fiber used in this work compared to the fiber in [30] is not known. This results in the need to setup a system for measuring dielectric properties in order to be able to follow them during the chemical change.

Various measurement techniques are available for the measurement of dielectric properties, such as: free space method, transmission-reflection method and resonance method. The choice of method is usually based on the expected range of dielectric properties, the desired frequency interval, the sample geometry and the aggregate state [15]. The open end of the coaxial probe requires a precise and reproducible contact with the device under test. This means that a defined section of the probe can directly contact the material. It is thus best for bulk materials larger than the probe diameter, powders or liquids. A

reproducible contact is not feasible with PAN fibers, as the individual filaments are difficult to hold in place, so that the coaxial probe is not an option. The free space method is not suitable due to the requirement of large bulk or gaseous samples. Also the measurement accuracy of the free space method depends on the measurement environment such as changes of the room temperature or movement of the measurement equipment [15]. In [30], the permittivity range $\epsilon_r^{'}$ for PAN is around 2.7 and 4.5 for the dielectric constant from room temperature up to 250 °C. The dielectric loss $\epsilon_r^{''}$ started below 0.1 and went up to 1 when heated to 250 °C. This results in the need for a measurement tool which can measure a larger range of dielectric losses. The transmission-reflection method is not suitable for the measurement of low losses.

The most suitable measurement technique, due to sample geometry, low losses at room temperature [30, 37], and environmental influences is the resonance method. The cavity perturbation method, which bases on a simple comparison of the resonance frequency and quality factor of the empty cavity compared to the cavity with the inserted material, is used to calculate the dielectric properties [56]. The dielectric properties of the fibers are calculated from the changes in resonance frequency and quality factor as follows [56]:

$$\varepsilon_r^{'} = \frac{1}{A_{\mathrm{cal}}} \frac{f_{\mathrm{r}} - f_{\mathrm{s}}}{f_{\mathrm{r}}} \frac{V_{\mathrm{c}}}{V_{\mathrm{s}}} + 1 \tag{2.5}$$

$$\varepsilon_r^{''} = \frac{1}{B_{\mathrm{cal}}} \frac{Q_{\mathrm{r}} - Q_{\mathrm{s}}}{Q_{\mathrm{r}} \cdot Q_{\mathrm{s}}} \frac{V_{\mathrm{c}}}{V_{\mathrm{s}}} \tag{2.6}$$

where $\varepsilon_r^{'}$ is the relative dielectric constant, $\varepsilon_r^{''}$ is the relative dielectric loss factor, f_{r} and f_{s} are the resonance frequencies of the unperturbed (reference) and perturbed cavity (with sample), respectively, Q_{r} and Q_{s} are the corresponding quality factors. V_{c} and V_{s} are the volumes of the cavity and the sample. The calibration factors A_{cal} and B_{cal} depend on the sample and cavity geometries, the sample permittivity as well as on the final cavity wave pattern. The calibration of A_{cal} and B_{cal} is done with the help of simulations in CST Microwave Studio [51] within the range of the expected dielectric properties. The resonance frequency and the quality factor can be determined via measurements of the scattering parameters (S-Parameters) with the help of a vector network

analyzer (VNA). The scattering matrix defines the relation between incident and reflected waves [55].

Measurement Uncertainty

An error contemplation is mandatory, as a reported data without specifying the error range is to be considered incomplete [57]. Any error contemplation is resulting in a certain level of uncertainty [58]. Even though error and uncertainty do not have the same definition according to [58], these will be used as synonyms in this work. Systematic errors are resulting from a known thus methodical or controllable influence, e. g. the measurement equipment. They can be reduced e. g. through calibration of the devices. Random errors are occurring when a measurement is repeated under the same conditions. The uncertainty of random errors can be quantified by repeating measurements and e. g. building the mean value. Further details can be found in literature [57,58].

In this work, the general calculation of the error follows the calculation of the combined standard uncertainty $u_\mathrm{c}(y)$ [58]:

$$u_\mathrm{c}^2(y) = \sum_{i=1}^{N} \left(\frac{\partial \mathrm{fun}}{\partial x_i} \right)^2 u^2(x_i), \tag{2.7}$$

where fun is the function of interest, N the number of terms in the function, x_i the input estimates and $u(x_i)$ the standard uncertainty for the respective input estimates.

Applied to the determination of the dielectric properties, the uncertainty of the dielectric constant $\sigma_{\varepsilon_r'}$ is calculated as follows:

$$\begin{aligned} \sigma_{\varepsilon_r'} = \sqrt{\left(\frac{\partial \varepsilon_r'}{\partial f_r} \sigma_{f_r} \right)^2 + \left(\frac{\partial \varepsilon_r'}{\partial f_s} \sigma_{f_s} \right)^2 + \left(\frac{\partial \varepsilon_r'}{\partial V_c} \sigma_{V_c} \right)^2} \\ \overline{+ \left(\frac{\partial \varepsilon_r'}{\partial V_s} \sigma_{V_s} \right)^2 + \left(\frac{\partial \varepsilon_r'}{\partial A} \sigma_A \right)^2}. \end{aligned} \tag{2.8}$$

σ_{f_r} and σ_{f_s} are the error of the measurement of the resonance frequencies of the unperturbed (reference) and perturbed cavity (with sample), respectively.

σ_{V_c} and σ_{V_s} are the errors in calculating the volumes of the cavity and the sample. σ_A is the error due to the simulation. Thus, σ describes the error of the respective indices introduced in eq. 2.5.
The uncertainty of the dielectric loss can be calculated accordingly:

$$\sigma_{\varepsilon_r''} = \sqrt{\left(\frac{\partial \varepsilon_r''}{\partial Q_r}\sigma_{Q_r}\right)^2 + \left(\frac{\partial \varepsilon_r''}{\partial Q_s}\sigma_{Q_s}\right)^2 + \left(\frac{\partial \varepsilon_r''}{\partial V_c}\sigma_{V_c}\right)^2 + \left(\frac{\partial \varepsilon_r''}{\partial V_s}\sigma_{V_s}\right)^2 + \left(\frac{\partial \varepsilon_r''}{\partial B}\sigma_B\right)^2}. \tag{2.9}$$

σ_{Q_r} and σ_{Q_s} are the error of the measurement of the quality factor of the unperturbed (reference) and perturbed cavity (with sample), respectively. σ_B is the error due to the simulation.

Overall Quality Factor of the System

The complete quality factor of a system can be expressed by a combination of the individual quality factors [55]:

$$\frac{1}{Q} = \frac{1}{Q_{\text{cavity}}} + \frac{1}{Q_{\text{s}}} + \frac{1}{Q_{\text{coupling}}}, \tag{2.10}$$

where Q_{cavity} is the quality factor of the empty cavity, Q_{s} is the sample quality factor. Q_{coupling} represents the coupling influence, the quality factor due to coupling.

For the experimental setup, a cylindrical cavity and the TM_{010} mode is chosen. The TM_{010} mode has the maximum electric field along the length of the cavity. It allows for a sample to be placed in the center of the cavity and thus results in a perturbation of the electric field as it is needed for the perturbation method. Also, it enables for continuous experiments a longer processing time inside the cavity as the full length is utilized for heating.

The quality factor Q_{cavity} of a completely closed and empty cylindrical cavity and a TM_{010} mode can be calculated according to the following equation [59]:

$$Q_{\text{cavity}} = \frac{\lambda_0}{\delta_s} \frac{\mathrm{p}_{01}}{2\pi(1 + r/d)} \tag{2.11}$$

where λ_0 is the free space wavelength, δ_s the skin depth, p_{01} the first root of the Bessel function of zero order, r the radius and d the height of the cavity. The chosen cavity has a height and radius of 45 mm to lead to a resonance frequency of around 2.5 GHz, to stay within the ISM-band, as any material leads to a shift to lower frequencies. Copper is chosen as material to increase the quality factor. Copper has a higher electric conductivity than Aluminium [55] resulting in a lower skin depth and wall losses. With eq. 2.11, a quality factor of nearly 14000 for the empty cavity is possible.
The quality factor of the coupling Q_{coupling} is included in the calibration factors A_{cal} and B_{cal} which are determined with the help of a simulation using the software CST [51]. The quality factor of a sample Q_{s} can be approximated by [15, 55]:

$$Q_{\text{s}} \propto \frac{1}{\tan\delta}. \tag{2.12}$$

2.2.3 Fundamentals on Reaction Kinetics

In this section, the essential knowledge on the reaction kinetics is presented. A chemical reaction of any compound 'i', also called reactant, can be described by the reaction rate r_{rate} which is the time dependent change of the concentration C_{i} of the compound 'i' [19]:

$$r_{\text{rate}} = \frac{\partial C_{\text{i}}}{\partial t} = -k \cdot C_{\text{i}}, \tag{2.13}$$

where k is the rate constant. The reaction rate is influenced by different parameters, such as the temperature T, the pressure p or the number of reactions and reactants involved, also called order of reaction [19, 20]. The temperature dependency of a reaction is included in the rate constant via the Arrhenius equation [19]:

$$k = k_0 \, e^{\frac{-E_a}{R \cdot T}}, \tag{2.14}$$

with the pre-exponential factor k_0, the activation energy E_a and the universal gas constant R. The pre-exponential factor influences how fast a reaction takes place. The activation energy influences when a reaction will take place, as it quantifies the minimum amount of energy needed. Only when the activation energy is reached, it takes place [19].

When multiple reactions are taking place, they can be classified in serial and parallel reactions depending on the reaction mechanism [21]. Nevertheless each reaction can be described with a reaction rate. Eq. 2.13 is also called a first order reaction. The order of reaction is defined by the sum of the exponents 'n' of all involved species or reactants. The reaction rate can be expressed in general as [19]:

$$r_{\text{rate}} = -k \cdot \prod_{i=1}^{N} C_i^n. \tag{2.15}$$

So if two compounds are part of the reaction or one concentration has the exponent to the power of two, it is a second order reaction [19, 20].

Degree of Conversion

In general, the degree of conversion α, hence the reaction progress, can be described as [60]:

$$\frac{\partial \alpha}{\partial t} = k \cdot f(\alpha), \tag{2.16}$$

where $f(\alpha)$ is a function of the degree of conversion [19, 60].
Different functions $f(\alpha)$ can be found in literature, for example in the ICTAC Kinetics Committee recommendations [60]. The most simple solution is a linear dependency:

$$f(\alpha) = 1 - \alpha. \tag{2.17}$$

Under the assumption that the process temperature is constant, the first order differential equation eq. 2.16 can be transformed together with eq. 2.14 to:

$$\alpha = 1 - e^{-t \cdot k}. \tag{2.18}$$

Calculations of Exothermic Reactions

Once a chemical reaction takes place, it can be either endothermic or exothermic. Exothermic reactions produce additional heat, while endothermic reactions need energy to continue. The released heat flow for a reaction can be calculated by [21]:

$$\dot{Q}_{\text{exo}} = r_{\text{rate}} \cdot (-\Delta H_{\text{reac}}), \tag{2.19}$$

with the reaction rate r_{rate} of the considered reaction and ΔH_{reac} the specific heat of reaction. The specific heat of reaction can either be calculated from the molecular bonds that are broken and formed or can be determined with the help of DSC measurements [20, 21]. Through the calculation of the broken and formed bonds, the specific heat for the reactions are calculated to be for the cyclization $-0.6533 \cdot 10^6$ kJ/kg, for the dehydrogenation $-4.933 \cdot 10^6$ kJ/kg, for the oxidation $-14.42 \cdot 10^6$ kJ/kg and for the reduction $28.80 \cdot 10^6$ kJ/kg [18].

Diffusion of O_2

As the stabilization takes place in an oxygen atmosphere, the diffusion of the oxygen between the filaments inside the bundle is also of interest. The radial mass transfer by diffusion for a cylindrical coordinate system can be calculated as follows [21, 61]:

$$\frac{\partial C}{\partial t} = \frac{1}{r} \frac{\partial}{\partial r} \left(r \delta \frac{\partial C}{\partial r} \right), \tag{2.20}$$

where C is the concentration of O_2 and r the radius. In a conventional heating oven, the fiber is heated on the surface first, so that is the place where the reaction starts first. This leads to the effect that at some point of the reaction no more oxygen can diffuse inside the fiber bundle between the filaments. In [22], it is shown that the advantage of the microwave, which is heating the volume and thus starting the reaction in the middle first, can lead to better quality grade fibers.

2.2.4 Measurement of Stabilization Degree

To collect more information about the quality and changes of the fiber after the reaction, additional measurements are performed. The density is measured

to compare the self-stabilized fibers with industrial values. The knowledge of the stabilization degree can be very helpful in order to know which grade of carbon fiber will be produced. A certain amount of oxidation is needed (8-14 %) [3, 10, 49], but an over-oxidation leads to poor grade carbon fibers [3]. Multiple options are used in literature to evaluate the degree of stabilization of a fiber, see Chapter 1.2. The establishment of a model can help in determining the stabilization degree as well. Here FTIR measurements and color are utilized.

Density

The density is measured with a scale from Sartorius Lab Instruments GmbH [62] which uses a gravimetric displacement method for the evaluation of the density. The stated accuracy of the scale is 1 mg. The density of the sample can determined by measuring the mass of the sample in air m_{air} and in a reference liquid m_{liq} with a known density ρ_{liq}. If the density is not known it can be worked out with a basic calibration block of which the volume and weight mass are known. The density of the sample ρ_{s} can be determined through [63]:

$$\rho_{\mathrm{s}} = \rho_{\mathrm{liq}} \cdot \frac{m_{\mathrm{air}}}{m_{\mathrm{air}} - m_{\mathrm{liq}}}. \tag{2.21}$$

The measurement uncertainty of the sample σ_{ρ_s} is calculated according to [58, 63] as follows:

$$\sigma_{\rho_{\mathrm{o}}} = \sqrt{\left(\frac{\partial \rho}{\partial m_{\mathrm{air}}}\sigma_{m_{\mathrm{air}}}\right)^2 + \left(\frac{\partial \rho}{\partial m_{\mathrm{liq}}}\sigma_{m_{\mathrm{liq}}}\right)^2 + \left(\frac{\partial \rho}{\partial \rho_{\mathrm{liq}}}\sigma_{\rho_{\mathrm{liq}}}\right)^2}, \tag{2.22}$$

where $\sigma_{m_{\mathrm{air}}}$ and $\sigma_{m_{\mathrm{liq}}}$ are the errors in measuring the mass of the sample in air and in liquid, respectively and $\sigma_{\rho_{\mathrm{liq}}}$ the error in the density of the reference liquid.

FTIR

In the scope of this work, a FTIR spectrometer type Vertex 70 from Bruker is used for measurements to determine the stabilization degree. The fibers

are placed in an Attenuated Total Reflection (ATR) module inside the FTIR spectrometer. Here, the MIRacle module from PIKE Technologies is utilized. An ATR module allows to place the sample directly on top of a crystal, through which the IR light beam is guided towards the sample. At the boundary surface part of the light is absorbed and part absorbed in the sample [64]. The reflected light is reduced by the absorbed light and can be evaluated at the detector. The absorbance spectrum is given in ATR units. A good contact between the sample and the crystal is necessary, which is provided by a pressure clamp which pushes the sample onto the crystal.
The FTIR measurements allow to compare the spectra of an untreated PAN precursor (in blue) and a stabilized fiber (in red) to visualized the chemical changes that took place during the stabilization, see Fig. 2.2. The stabilized fiber was industrially produced from the same PAN precursor. The most significant bonds are marked and labeled at their occurring wavenumber [32, 64].

The progress of the cyclization can be best seen on the peak of the C≡N at a wavenumber of $2240\,\mathrm{cm}^{-1}$ which is reduced with an increasing degree of stabilization, while the peak of the C=N bonds at $1595\,\mathrm{cm}^{-1}$ increases. Similarly, the dehydration and oxidation reduce the C-H_2 peak at $1450\,\mathrm{cm}^{-1}$ while the C=O peak and the C=C peak increase at $1660\,\mathrm{cm}^{-1}$ and $1640\,\mathrm{cm}^{-1}$, respectively [32, 64]. C=O bonds are produced through the oxidation and C=C bonds through the dehydration, see eq. 1.1. As the C=O and C=C peaks are very close together, they overlap and form one larger peak in the spectrum [43] only the C=O spectra line is labeled.

From the change in peak heights the stabilization degree can be defined and calculated. As most peaks tend to overlap only the cyclization is extractable easily when the processing is performed in nitrogen. Of course also other lines in the spectra can be used for the definition of a stabilization degree. In this work, the cyclization stabilization degree is determined according to [32, 36, 65, 66] as

$$\alpha_{\mathrm{cycl}} = \frac{A_{\mathrm{C=N}}}{A_{\mathrm{C=N}} + A_{\mathrm{C\equiv N}}} \tag{2.23}$$

$A_{\mathrm{C=N}}$ is the height of the absorbance spectra line of the C=N bond and $A_{\mathrm{C\equiv N}}$ accordingly for the C≡N group.
The measurement uncertainty is evaluated according to [58], see eq. 2.7.

2.3 Experimental Setup

In this section, first the experimental setup of the stationary dielectric measurements is presented. Afterwards the continuously working setup with a propagating fiber bundle is explained and which parts are different to the stationary measurement system.

2.3.1 Stationary In-situ Dielectric Measurement System

Fig. 2.3 shows a schematic representation of the measurement setup, which is developed as part of this thesis. The TM_{010}-mode cylindrical cavity, with a radius and height of around 45 mm, is placed horizontally to be able to place a 12k PAN fiber within a quartz tube along the maximum of the electric field. A N-type connector in combination with aluminum pin act as coupling element for the input port and a SMA (SubMiniature Version A) connector with another aluminum pin as output port. The pins are inserted through the cavity wall, inside the cavity. The high frequency cables are displayed in blue. The scattering parameters are measured by a Vector Network Analyzer (VNA) and the quality factor and resonance frequency are extracted. The stationary measurements are done with a HP 8720D from Hewlett-Packard. The VNA

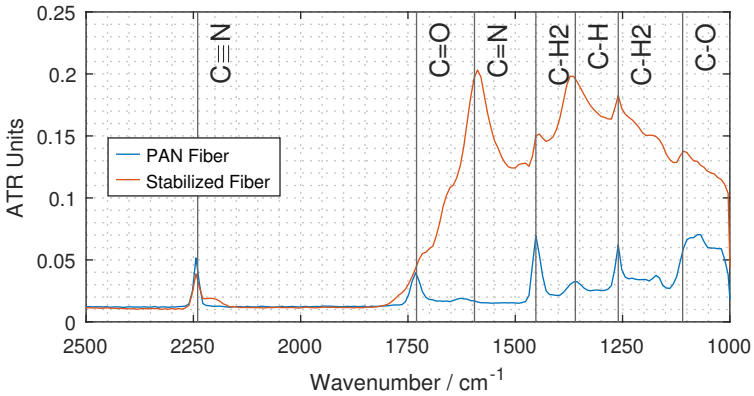

Figure 2.2: FTIR spectra from PAN precursor and an industrially stabilized fiber.

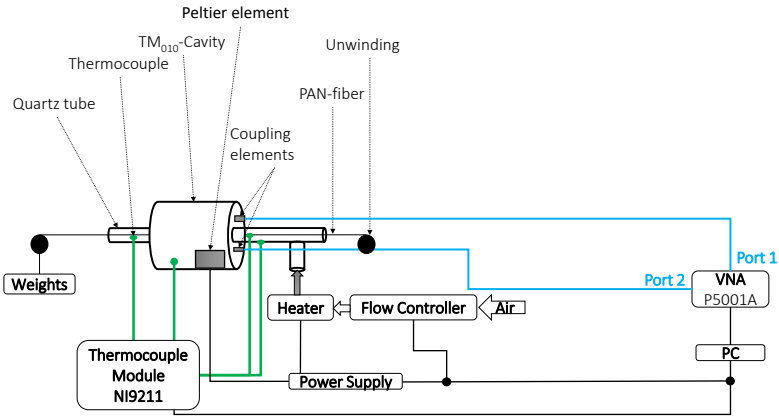

Figure 2.3: Schematic of dielectric measurement setup, adapted from [67].

is set to 5001 points. The pins joined to the connectors are adapted, so that a quality factor of about 10000 of the empty cavity is reached.

The quartz tube is added for three main reasons. First, to protect the cavity from the gases, that are produced during the stabilization. Second, to help guide the hot air flow for the conventional heating, without losing to much temperature over the length of the cavity. Third, to protect the cavity from any residue of an overheated fiber. The tube has an inner diameter of 8 mm and an outer diameter of 10 mm. The quartz tube position is fixed with the help of a Teflon insulation ring. The fiber tension is realized on one side through the fixed spool from which the precursor is coming and weights on the other side.

In a first step, the fiber is heated conventionally, to follow the industrial process as close as possible. The industrial processes are already optimized to produce good quality grade fibers. In order to be later on able to produce the same quality grade fibers with microwave heating, it is essential to use process parameters similar to the industrial ones. The adaptation from a conventional heating source is achieved with the help of pressurized air, a flow controller and a heater. The heater, type MK-45R from Zinser GmbH is installed together with a flow controller of the red-y smart series from Voegtlin GmbH. The

heater is modified to be able to use an analog control via the power supplied. This helps to setup the control loop for the hot air temperature. Pressurized air of one bar is used as input air flow to the flow controller, which is set to 100 ln/min. It then passes the heating cartridge and is channeled into the quartz tube where it heats the PAN fiber.

The temperature is measured by a NI-9211 thermocouple input module from National Instruments together with type K thermocouples, marked in green in Fig. 2.3. According to [68], type K thermocouples have an accuracy of +/- 2.2 °C and a measurement sensitivity of 0.07 °C. Two thermocouples are placed inside the quartz tube right in front of the entry and the exit point of the cavity to measure the air flow temperature. The thermocouples can not be placed further inside the cavity, as their metal tip disturbs the electric field profile and thus the mode. Also it acts as an antenna which leads to microwave leakage. A third one is used to measure the temperature of quartz tube from the outside, in order to know when the system is completely cooled down. A fourth is placed on top to measure and control the cavity temperature.

The hot air in the quartz tube, also over time heats the air inside the copper cavity. This affects the temperature of the cavity, and results in an expansion which changes the resonance frequency of the system. Thus, a temperature stabilization of the cavity is necessary to reduce the resonance frequency variation and improve the measurement uncertainty.
Using a 180 W Peltier element the cavity temperature is stabilized to a preset value of typically 20 °C. Through the Proportional Integral Derivative (PID) controller, an accuracy of the control loop of +/- 0.3 °C is possible. The frequency shift due to thermal expansion is thus limited to 11.6 kHz. A temperature change of the quartz tube also leads to a shift of the resonance frequency, but not the quality factor, as the dielectric loss of the quartz tube is too low [69] to see any temperature dependent effect in the utilized temperature range. Differentiating the influence of the stabilization reaction on the PAN fiber from the mentioned sources can be achieved through calibration. The system is heated up multiple times without a fiber, but with the quartz tube and the changes in resonance frequency are correlated to air and quartz temperature.

Scattering Parameter Measurement

The scattering parameters are needed to determine the resonance frequencies and quality factors of the empty system, as well as with the sample, see eq. 2.5 and eq. 2.6. A VNA allows to measure the S_{21} parameter from which the resonance frequency and quality factor are extracted. In Fig. 2.3 the measurement ports are labeled. The mode of operation allows to specify with how many frequency steps, thus measurement points and in which frequency range the scattering parameter is obtained. Here, the frequency range is defined through the resonance frequency f_r as center frequency, the bandwidth BW and the number of frequency points. The VNA sweeps through the desired frequency range over time at Port 1, see Fig. 2.4a. The wave passes through the network, in this case, the cables and the cavity to be transmitted to Port 2. The transmitted wave contains information on the network, which can be displayed. An exemplary S_{21} curve for a resonator can be seen in Fig. 2.4b. The point where the S_{21} parameter has decreased 3 dB from its maximum value S_{max} is used to determine the 3 dB bandwidth BW_{3dB}. The quality factor can be then be determines through [70]:

$$Q = \frac{f_r}{BW_{3dB}}. \tag{2.24}$$

In order to get good results, it can be necessary to adjust the measurement bandwidth to have enough measurement points in this range. After one frequency sweep is done, depending on the settings the VNA starts directly with the next one or waits until it gets a new trigger to start the sweep.

CST Model

As mentioned before, a simulation is necessary in order to evaluate the factors A_{cal} and B_{cal} in eq. 2.5 and eq. 2.6. The sample has to be included in the model. A 12k PAN fiber consisting of 12000 filaments that are bundled together is used for the dielectric measurements. A filament diameter is about 10 μm. Simulating single filaments in the CST calibration is not suitable. It leads to a strongly increased simulation time. However, the knowledge of the sample volume is an important key parameter to evaluate the dielectric properties. For this reason as a simplification is introduced. The filaments are formed into one cylinder, building one fiber with an effective diameter, see Fig.2.5. It

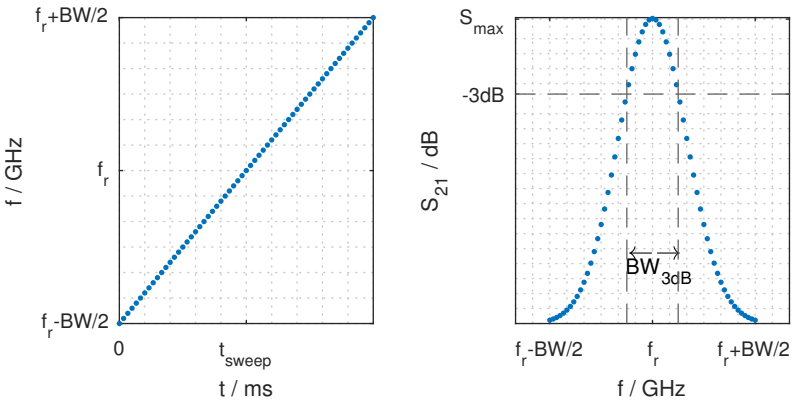

(a) Schematic of the frequency points sent over time from the VNA

(b) Schematic of S_{21} parameter over the frequency as measured from the VNA

Figure 2.4: Exemplary schematics to explain the measurement of scattering parameters.

is assumed that the fiber is always under tension and therefore the fibers are stretched. The effective diameter d_{fib} can be calculated as from the assumption that each filament as the same volume and the sum of all filament volumes together are equal to the effective volume of one larger fiber. Assuming there are N filaments to form a fiber bundle the effective diameter can be calculated as follows:

$$V_{\text{eff}} = V_{\text{fil}} \cdot N \tag{2.25a}$$

$$\pi \cdot h \cdot r_{\text{fib}}^2 = \pi \cdot h \cdot r_{\text{fil}}^2 \cdot N \tag{2.25b}$$

$$r_{\text{fib}}^2 = r_{\text{fil}}^2 \cdot N \tag{2.25c}$$

$$r_{\text{fib}} = r_{\text{fil}} \cdot \sqrt{N} \tag{2.25d}$$

$$\text{with } d = 2 \cdot r \text{ follows } d_{\text{fib}} = d_{\text{fil}} \cdot \sqrt{N} \tag{2.25e}$$

Two options are possible to calculate the effective fiber diameter based on measurements. The first option is to calculate the fiber diameter from the filament diameter which is measured before under a microscope. The second option is to use density, weight and length measurements. The effective diameter is determined using both options and building the mean value of both

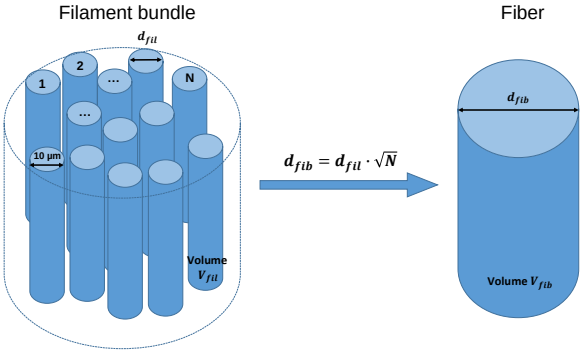

Figure 2.5: Approximation of effective fiber diameter, adapted from [67].

and multiple measurements. Of course these measurement methods lead to new sources of uncertainties. The weight measurements are done with a Kern PFB 300-3 scale which can measure with an accuracy of 1 mg. The length measurements are done with a simple ruler. The effective fiber bundle radius is calculated to be 0.54 mm±0.05 mm.

2.3.2 Effective Material Properties of PAN

As the fiber consists of multiple filaments with air gaps in between, effective material properties are calculated according to the porosity of the fiber [18]. First the porosity is calculated with the help of a microscopic view of the fiber bundle. In order to be able to do that the fiber is stretched and embedded in epoxy resin, see Fig. 2.6. The embedded fiber sample is whetted and polished to see the filaments in the optical micro graphs with good contrast. An Olympus BX60M microscope and different magnification levels are utilized to obtain the micro graphs. Fig. 2.7a shows that the fiber is stretched out instead of building a round shape. Also the air holes are irregular which appear as black holes. The root cause might be the manual stretching via a rectangular rod when embedded in the resin. With each magnification the individual filaments can be seen better as shown in Fig. 2.7. The largest magnification in Fig. 2.7d shows clearly the individual filaments and the space in between. At this magnification level, the diameter of a filament is measured as 12.49±0.63 μm.

Parameter	PAN fiber	Unit
Axial thermal conductivity λ_{th}	0.1461	W/(m K)
Radial thermal conductivity λ_{th}	0.069	W/(m K)
Density ρ	616	kg/m^3
Heat capacity c_p	1310	J/(kg K)
Emission coefficient ϵ_{th}	0.95	-

Table 2.2: Effective material parameters for PAN fiber [18, 71].

In order to determine the porosity, a rectangular area is defined. It is placed at different locations of the microscope images. In each area, the fiber content is determined manually and the porosity with the filament diameter 12.5 μm. The final porosity is calculated as the mean value of the porosity of the different areas to be 46 %. Then, the porosity is used to calculate the effective thermal conductivity, density and specific heat capacity as shown in Table 2.2.

2.3.3 Measurement Uncertainty of Dielectric Properties

The accuracy of the measured dielectric properties is influenced primarily by the following main parameters: temperatures of the cavity and the quartz tube, positioning of the quartz tube and sample, and the sample volume used in the calibration. Other influencing factors include the accuracy of the VNA measurement and the accuracy of the applied simulation for the calibration. A collection of influences on the uncertainty are summed up in an Ishikawa diagram, see. Fig. 2.8. Eq. 2.8 and eq. 2.9 show the needed uncertainties for the calculation and in the following their determination will be shortly presented.

The sample volume error σ_{V_s} is determined by using the mean value of the effective fiber radius as mentioned in the CST model setup. This results in a fiber volume with an uncertainty of 41.93±0.83 mm^3. The cavity volume error σ_{V_c} is influenced by the temperature of the cavity and the exact geometric properties. The CST model is adapted to fit the measured reference frequency and quality factor to the simulated ones for the TM_{010} mode. The cavity is cooled to reduce the temperature influence. Nevertheless, it is assumed that a maximum of 3 °C change of the cavity temperature can occur in order to

(a) Stretching

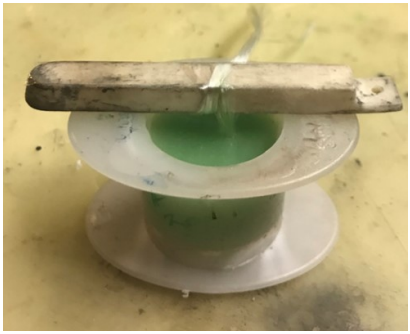

(b) Embedding

(c) Final sample

Figure 2.6: Preparation of fiber probe for an investigation of the filament diameters and distribution in the bundle under a microscope: stretching, embedding in epoxy resin, hardening and abrasion [18].

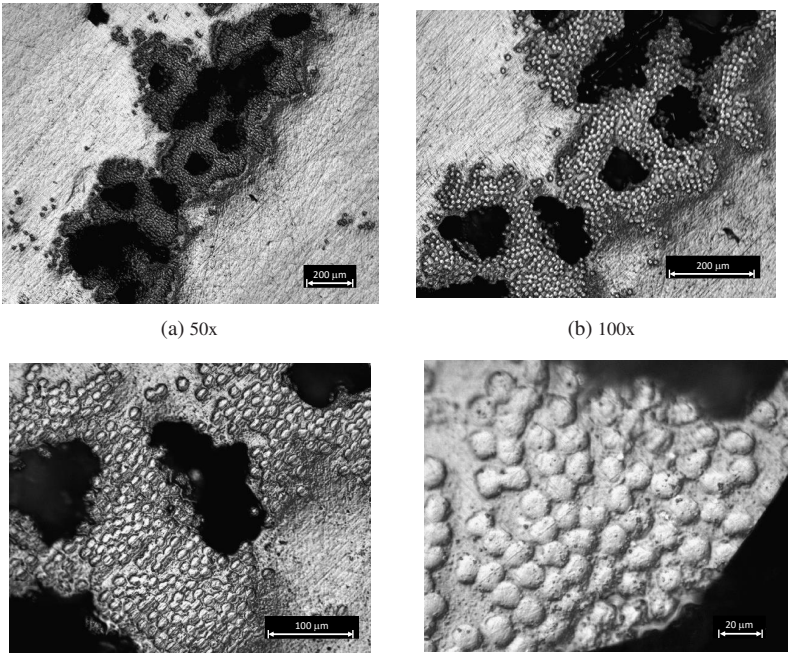

(a) 50x (b) 100x

(c) 200x (d) 500x

Figure 2.7: Fiber bundle with filaments in microscopic view with different magnifications [18].

quantify the uncertainty. With the thermal expansion coefficient of copper of $16.7 \cdot 10^{-6}$ m/°C [72], this results in a cavity volume of $286 \cdot 10^3 \pm 239\,\mathrm{mm}^3$. The uncertainties due to the frequency measurements σ_{f_r} and σ_{f_s}, as well as due to the quality factor measurements σ_{Q_r} and σ_{Q_s}, depend not only on the settings and accuracy of the network analyzer but also, on the temperature of the cavity, the position and temperature of the quartz tube. For the dielectric constant the error of the resonance frequency σ_{f_r} is of interest. Since the cavity perturbation with the PAN fiber is rather small at room temperature, the precise measurement of the dielectric constant depends strongly on the error of the measured resonance frequency of the empty cavity. With the help of a PID controller, the cavity temperature can be controlled in the range of 20±0.3 °C due to the controller. It has to be considered that the uncertainty of

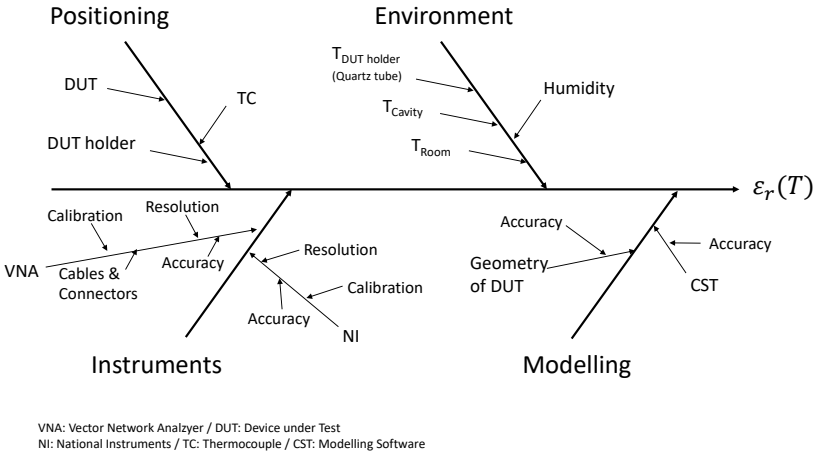

Figure 2.8: Ishikawa diagram for measurement uncertainties for dielectric loss.

the thermocouple is still in the range of ±2.2 °C. With the thermal expansion coefficient, this leads to a frequency shift due to the thermal variations of ±293 kHz in the empty cavity. The error of the quality factor measurement σ_Q is determined by calculating the mean quality factor of repeating measurements at room temperature. Thus for the overall measurement uncertainty, it is assumed that the quality factor can be measured ±50.

The position of the quartz tube has an impact on the resonance frequency and quality factor as small material deviations can occur. In order to avoid this influence, the tube position is fixed. The junction of the quartz tube is used as a stopping mechanism when inserted into the cavity. Also Teflon insulation rings are inserted in the cavity wall to keep it fixed around the field maximum to avoid movement when the fiber is inserted. Due to the fixation of the position, it is possible to neglect errors from this source. The temperature of the quartz tube has an effect on the resonance frequency too, while the quality factor of the system is not affected as the dielectric loss of the quartz tube stays constant over the desired temperature range. The heated air, flowing through the quartz tube, also heats up the tube. An increase of the temperature of the air inside the quartz tube up to 235 °C leads to a shift in the resonance frequency of about 275 kHz. A calibration is conducted to separate this effect for the determination of the dielectric properties. The temperature dependent

frequency shift of the empty quartz tube is measured separately for each set of process parameters and used as reference.
As a simulation is used to evaluate the dielectric properties, the simulation errors σ_A and σ_B have to be taken into account as well. They depend on the chosen mesh size and simulation accuracy. A trade-off between the accuracy, mesh size and the simulation time has to be made. For the determination of the simulation error, different mesh sizes are applied. The simulation factors A and B are calculated based on the simulation results. After the mean value of the factors A and B is calculated for different mesh sizes, the error to the actual used size can be calculated. This leads to an error for the calibration factors of $\pm 3\,\%$. The resulting calibration factors can be seen over the difference between quality factor and resonance frequency in Fig. 2.9. This simplified display was chosen to get faster an idea of the resulting dielectric parameters through approximation during the measurements.

Thermocouple Placement

Fig. 2.10 shows schematically the difference between two thermocouples, one in green and one in yellow. From the outside, optically, both seem to be at the same place, but inside the quartz tube, both vary slightly, by being a little bent or a or a little further inside the tube. In reality, only one thermocouple is used and is put back in place e. g. when the fiber has to be threaded again. Even though, measures are taken to ensure a replacement as precise as possible, it can affect the overall measurement. If the thermocouple placement is not reproducible and if two data points show the same temperature, they do not necessarily refer to the same position. Its influence on the measurements will be shown in Chapter 3 and discussed in Chapter 4. In future work, the uncertainty of the thermocouple placement could be determined e. g. with a series of measurements along the radius.

2.3.4 Continuous Experimental System

In Fig. 2.11, a picture of the experimental setup of the continuous process is shown and in Fig. 2.12 the utilized devices are shown schematically. The green lines are the thermo couples and the blue lines are high frequency cables and in orange the cables used to transmit the trigger signal. Devices and components

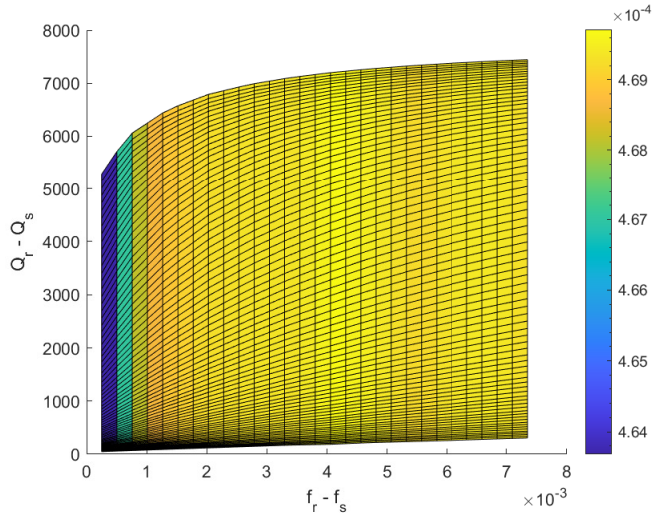

(a) Calibration factor A

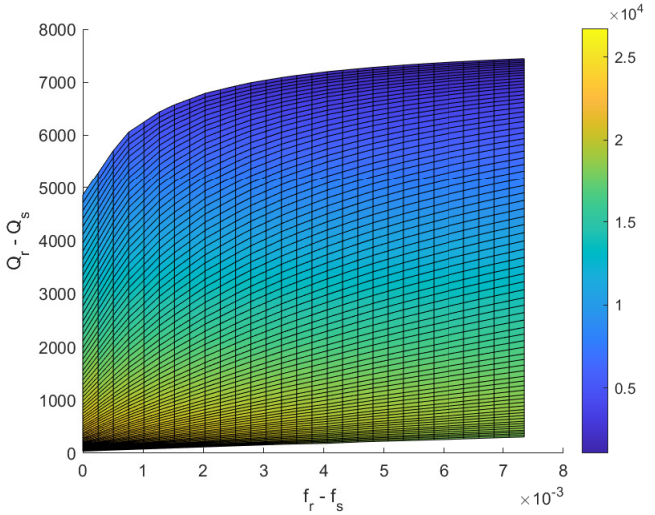

(b) Calibration factor B

Figure 2.9: Calibration factors A and B depending on the differences between resonance frequency f_r and sample frequency f_s and quality factor of empty cavity Q_r and with sample Q_s.

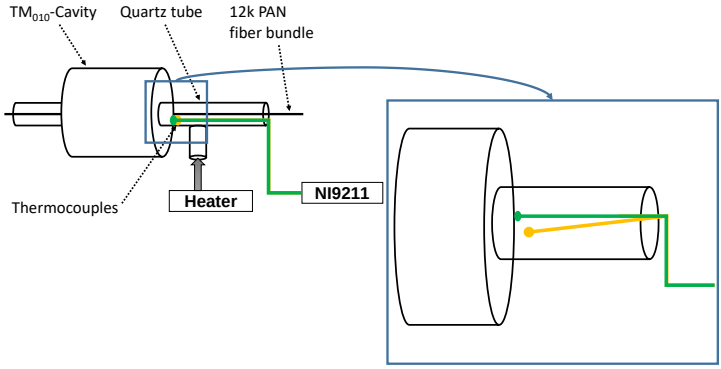

Figure 2.10: Differences in thermocouple placement.

are given in bold letters to distinguish from the labels.
A winder system is used to guide the PAN fiber through the cavity where the microwave heating takes place. The winders can be seen at the left and right, in between the cylindrical TM_{010} cavity is placed. The winder system made by Supertek, Germany, is able to pull the fiber with a variable tension of 5 N to over 20 N and a speed of 0.64 mm/s up to more than 100 mm/s.
A heater system, type MK-45R from Zinser GmbH, is used for the temperature dependent dielectric measurements together with an air flow controller of the red-y smart series from Voegtlin GmbH. A microwave amplifier MP2350/700/50MK-A of G-WAY Microwave with a 50 dB gain and a saturated power level of 100 W is inserted between the the P5001A network analyzer from Keysight and the circulator. The network analyzer operates as frequency synthesizer. The circulator from Philips type 2722 is added to protect the amplifier from any reflected power. After the circulator, a bidirectional coupler type PNR CHP274-30F-30R from Narda ATM is placed before the applicator. The coupler is used to measure the forward and reflected power. This allows the calculation of the absorbed microwave power in the system. To measure the power, two power meters from Anritsu are used of type ML2487B and ML2495A together with Anritsu sensors of type MA2440D. Before each power sensor, a 10 dB attenuator is placed to protect the sensor from too high power levels. The pin coupling of the cavity is adapted to allow a stronger

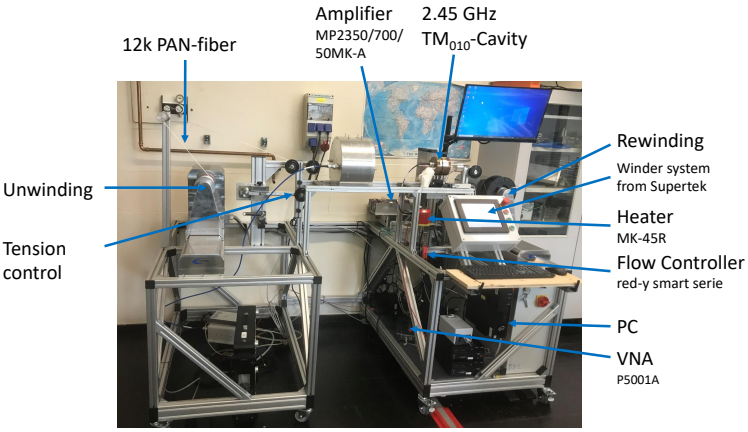

Figure 2.11: Experimental setup.

heating. The quality factor of the empty cavity after the adaption of the pin lengths is about 8000.

Power Measurement Analysis

The microwave power is measured with help of the power meters measuring the reflected and transmitted power. However in order to obtain correct power levels it is important to explain shortly the setup in more detail. The microwave power is provided by an amplifier which is connected to a VNA, see Fig. 2.12. The VNA measures the scattering parameter over the frequency, as explained before, see Fig. 2.4. It continues to sweep through the desired frequency range over time, see Fig. 2.13a. The amplifier provides microwave power at every sweeping point, depending on the amplification factor, here 50 dB. However, depending on the quality factor and coupling into the TM_{010} cavity, different power levels are reflected. The absorbed power in the cavity can be calculated from the measured incident power provided by the amplifier minus the measured reflected power. Closer to the resonance frequency, more power is absorbed in the system. This setup leads to a varied power input over time and the mean power level can be calculated.

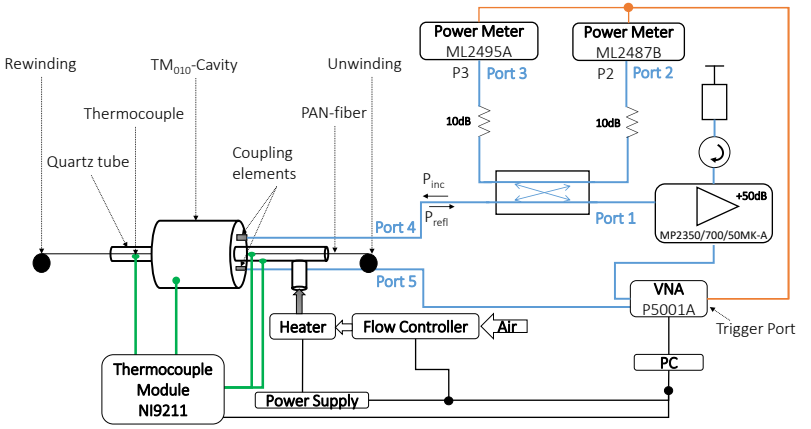

Figure 2.12: Schematic of experimental setup.

The absorbed power results in a temperature change of the fiber, which is followed by a change of the resonance frequency and quality factor due to the temperature dependency of the dielectric properties and the chemical reaction. These changes influence the mean power level. In order to keep it constant or even increase the heating, the frequency bandwidth has to be adapted by reducing it. In Fig. 2.13 this is schematically indicated through the green curve and areas of a smaller bandwidth compared to a larger bandwidth in blue. It is reduced so that a smaller frequency range is in the focus, leading to a higher mean power level, see $P_{m,BW2}$ in green in Fig. 2.13b. More power is introduced in the system in case of a smaller bandwidth as more frequency points closer around the resonance frequency are covered in the same sweeping time $t_{s,\,BW2}$, see green area in Fig. 2.13b, than for the case of a larger bandwidth $t_{s,\,BW2}$(see blue area).
Even though this approach relies on the manual adaptation of the bandwidth, it is chosen in a first step. It allows to verify the influence of each change on the resonance frequency and color of the fiber before adapting it further. Port 5 in Fig. 2.12 is only used to allow the adaptation of the bandwidth. The absorbed power over time in the system is measured seperatly to gather further insights in the process and the energy uptake.

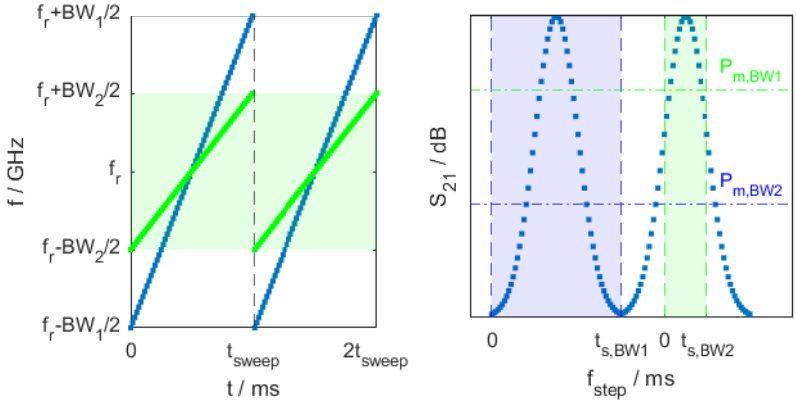

(a) Schematic of the frequency over time as generated from the VNA

(b) Schematic of the absorbed power in the system over time

Figure 2.13: Schematics to explain the power measurements depending on the frequency.

In Fig. 2.12, it can be seen that the power meters are attached to a coupler and attenuators. For a precise calculation of the absorbed power, the attenuation from the high frequency cables, the coupler and attenuators need to be taken into account. This is done via a separate calibration process, that is described in the following.

The network between the ports one to four can be described by the S-parameters. In Fig. 2.12, the ports one to four are labeled. They need to be obtained before the power measurements. First, the network analyzer is calibrated in the desired frequency range including the measurement cables. Next, the S-parameters between all 4 ports are measured and saved. After the S-parameters are obtained, they can be used to correct the measured power levels after measuring the uncorrected incoming P_2 and reflected power P_3 at Port 2 and 3, respectively. The corrected incoming P_{inc} and reflected power P_{refl} can then be calculated according the following equations:

$$P_{\text{refl}} = \frac{P_3 \cdot S_{21}^2 - P_2 \cdot S_{31}^2}{S_{43}^2 \cdot S_{21}^2 - S_{42}^2 \cdot S_{31}^2}, \tag{2.26}$$

$$P_{\text{inc}} = \left(P_2 - P_{\text{refl}} \cdot S_{42}^2\right) \frac{S_{41}^2}{S_{21}^2}, \tag{2.27}$$

where S_{xy} describe the measured S-parameters for the respective ports with values for x and y from 1 to 4, see Fig. 2.12. The derivation of the equations can be found in the appendix A.1.
The power meters are set to capture the same time as the sweeping time of the network analyzer. They get a trigger signal from the VNA to start the measurement at the same time, as the frequency sweep. This allows to calculate the mean power by integration over the sweeping points and division through the sweeping time t_{sweep}. The absorbed mean power P_{mean} in the system can be calculated by:

$$P_{\text{mean}} = \frac{1}{t_{\text{sweep}}} \int_{t=0}^{t_{\text{sweep}}} \left(P_{\text{inc,t}} - P_{\text{refl,t}}\right)\, dt \tag{2.28}$$

It was chosen to focus on the mean power level in the results, as the influence of each change in power level was observed for a longer time than the processing time. The sweeping time of the network analyzer was much smaller than the processing time of the fiber trough the applicator, so that a stationary process can be assumed allowing a power contemplation instead of an energy consideration in the results.
The measurement uncertainty for the power measurement is influenced by the accuracy of the measurement of the scattering parameters with the network analyzer and of the power levels of the incoming and reflected power. In [73] the uncertainty of the power meters together with the used sensor can be calculated at the used frequency. With the mentioned equipment, this leads to an expanded combined standard uncertainty (95 % confidence interval) of 6.02 %. The overall power measurement uncertainty is calculated according to the combined standard uncertainty [58], see eq. 2.7.

2.4 Process Model

Although some models exist that are calculating the heat or stabilization progress with PAN fibers, to the knowledge of the author, they do not include microwave heating. Considering microwave heating in combination

with all relevant heating mechanisms such as convective heating, heat transfer, and heat generated by the exothermic reactions is the goal of the model that is set up in this section. It provides insights in the stability of the process and the range of process parameters needed for reaching a certain temperature range. After the explanation of the setup, a comparison of the mathematical model to the commercial software tool Comsol [74] is shown.

2.4.1 Heat Transfer

In general, a temperature change ΔT is the result of an energy Q_{th} that is introduced into the material. The amount is dependent on the mass m and the heat capacity c_p of the material [53]:

$$\Delta T = \frac{Q_{\text{th}}}{m \cdot c_p}. \tag{2.29}$$

The energy is not transferred instantly but over a certain time. The power, or energy flow $\dot{Q}_{\text{th}}$, describes the amount of thermal energy Q_{th} added over time t [52]:

$$P = \frac{\partial Q_{\text{th}}}{\partial t} = \dot{Q}_{\text{th}}. \tag{2.30}$$

Combining eq. 2.29 and eq. 2.30 leads to the equation:

$$\frac{\partial T}{dt} = \frac{\dot{Q}_{\text{th}}}{m \cdot c_p}. \tag{2.31}$$

It describes the change of temperature during a certain time period dependent on the heat provided in that period. An integration of eq. 2.31 over time delivers the temperature at the desired time step.

In the scope of the work relevant heat transfer mechanisms are thermal convection, thermal conduction and thermal radiation. A flowing fluid such as water or air can transport energy in the form of heat which is called thermal convection $\dot{Q}_{\text{th,conv}}$:

$$\dot{Q}_{\text{th,conv}} = \alpha_{\text{th}} \cdot A \cdot (T - T_0), \tag{2.32}$$

where α_{th} is the heat transfer coefficient, A the area over which the heat transfer is considered, T the surface temperature of the object, T_0 the ambient

temperature of the fluid. Thermal conduction $\dot{Q}_{\mathrm{th,cond}}$ is characterized by the heat transport inside a material to balance an internal temperature difference:

$$\dot{Q}_{\mathrm{th,cond}} = \lambda_{\mathrm{th}} \cdot \frac{A}{d} \cdot (T - T_0), \tag{2.33}$$

where λ_{th} is the thermal conductivity and d the thickness of the material. Thermal radiation $\dot{Q}_{\mathrm{th,rad}}$ describes the emission of an electromagnetic wave [52] [61],

$$\dot{Q}_{\mathrm{th,rad}} = \epsilon_{\mathrm{th}} \cdot \sigma_{\mathrm{B}} \cdot A \cdot (T^4 - T_0^4), \tag{2.34}$$

where ϵ_{th} is the emissivity and σ_{B} the Stefan-Boltzmann constant. The temperature of the individual mesh cells is calculated according to eq. 2.31. Step by step all heat sources are included so that in the end $\dot{Q}_{\mathrm{th,sum}}$ is equal to:

$$\dot{Q}_{\mathrm{th,sum}} = \dot{Q}_{\mathrm{th,conv}} + \dot{Q}_{\mathrm{th,cond}} + \dot{Q}_{\mathrm{th,rad}} + \dot{Q}_{\mathrm{th,exo}} + P_{\mathrm{MW}}, \tag{2.35}$$

where the individual heat sources are defined by eq. 2.32 to 2.34, $\dot{Q}_{\mathrm{th,exo}}$ through eq. 2.19 and P_{MW} the microwave power absorbed inside a material through eq. 2.3.

2.4.2 Setup of the Process Model

As the fiber, quartz tube and resonator are all cylindrical structures, the system is axially symmetrically. This means that the 3D model of the system can be simplified to a 2D model, which can be simplified further through a 2D-cut along the the center of the fiber, as the system is rotational symmetric, see Fig. 2.14. The 2D-cut only considers half of the fiber, starting in the fiber center, which can be seen in the mesh. The relevant elements, which are considered for the temperature calculation, are the fiber, the air gap and the quartz tube. The cavity used for the dielectric measurements serves as starting point for the model. Its geometrical properties are used for modeling to allow later on a comparison with experimental results.
It is assumed that the cavity has a constant temperature of 20 °C which is set as boundary condition to the outside of the quartz tube. Only the parts inside the cavity are considered. Exemplary, a mesh with six cells in axial direction and in radial direction with four cells for the fiber, two cells for air and two cells for quartz, can be seen in Fig. 2.14. The accuracy of the modeled

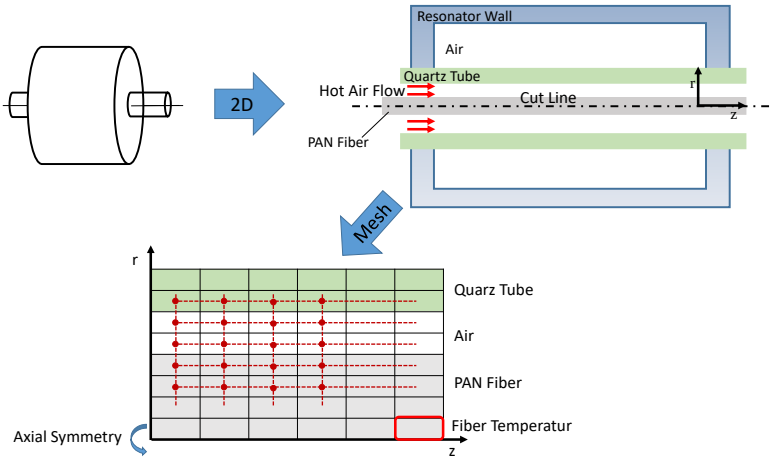

Figure 2.14: Simplified 2D mesh for the rotational symmetric setup.

results can be adapted by increasing the number of cells in axial and radial direction. Although a trade off has to be made between calculation time and accuracy, which will be discussed in a later section. Each cell is connected to the individual material properties, see Chapter 2.1. The most inner mesh cell, in the center of the fiber is marked, as its temperature is used in the discussion of the simulation.

Finite Volume Method

As numerical approach the Finite Volume Method (FVM) [75] is used for the discretization of the conservation laws namely the law of conservation of energy. The substrates of interest are divided into smaller cells with a constant volume. It is assumed that the whole volume of the cell has a homogeneous temperature and constant material properties. As the temperature of one cell affects the temperatures of the surrounding cells, the heat transfer is calculated for every cell. The differential equations are solved with the help of the ordinary differential equations (ODE) solver in Matlab [76]. The used Matlab ODE solver implements a variable-step, variable-order (VSVO) solver based on the numerical differentiation formulas (NDFs) with variable time-step.

Furthermore, it allows the specification of error tolerances and implements optimized logarithms to avoid oscillations occurring from numerical effects [18, 21, 75, 76].

Adaptation of Heat Transfer Equations

Even though the mesh representation is simplified to a 2D section, the heat transfer equations are taken into account the cylindrical shape of both, the fiber and the quartz tube. The heat transfer equations are adapted for a cylindrical coordinate system. The calculation of the thermal conductivity for circular cylindrical tube can be calculated with [52]:

$$\dot{Q}_{\mathrm{cond,gap}} = -\lambda_{\mathrm{th}} 2\pi r L \frac{\partial T}{\partial r}. \tag{2.36}$$

Solving the equation for a pipe, thus solving the integration over two rods inserted in each other, leads to [52]:

$$\dot{Q}_{\mathrm{cond,gap}} = \frac{\lambda_{\mathrm{th}} 2\pi L}{\ln\left(\frac{r_{\mathrm{o}}}{r_{\mathrm{i}}}\right)} \Delta T, \tag{2.37}$$

where r_{i} and r_{o} are the outer radius of the inner rod and the inner radius of the outer rod, thus describing the gap distance, L is the length of the rod and λ_{th} the thermal conductivity.
Similarly the radiation is adapted as follows [52]:

$$\dot{Q}_{\mathrm{rad,gap}} = \frac{\sigma_{\mathrm{B}}}{\frac{1}{\epsilon_{\mathrm{th,i}}} + \frac{A_{\mathrm{i}}}{A_{\mathrm{o}}}\left(\frac{1}{\epsilon_{\mathrm{th,o}}} - 1\right)} A_i (T_i^4 - T_o^4), \tag{2.38}$$

where A_{i} is the outer area of the inner rod, and A_{o} the inner area of the outer rod, the space between both is also called annular gap, and,ϵ_{th} the emissivity of the respective areas.

Electric Field Strength

In a first step a constant electric field over the length of the applicator is assumed. This allows to base the process model on the CST [51] model of the

cavity, that is used for the dielectric measurements. Thus, in a first step the effective electric field strength is extracted from the CST model and adapted according to the input power level of the microwave. Finally, it is assumed that the electric field profile is constant over time and only affected by the amplification level. Any changes due to the coupling are neglected.

Comparison with Comsol

After the setup of the process model, the result in temperature change due to each contribution to the overall heat, see eq. 2.35, is compared to a model set up in the software Comsol [74]. This allows a verification of the setup and programming. Exemplary, in Fig. 2.15 the temperature profile of a mesh cell is shown over the time. In this case it is the last mesh cell before the cavity wall at the outlet on the surface of the fiber. Only the heat transfer in a stationary case with an air temperature of 200 °C is considered. In total 30 cells in axial direction, 20 cells in radial direction for the fiber, 15 cells for air and 15 cells for the quartz are chosen.
The indices ‘m‘ and solid lines signify the data acquired through the process model in Matlab and ‘c‘ and dashed lines the data acquired through the Comsol model. It shows a good agreement. The same is true for the temperature profile over the radius, see Fig. 2.16. It shows the radial profile of the last mesh cells before the cavity wall at the outlet for the last simulation time step at 720 s. The meshgrid to be seen in Fig. 2.16 does not represent the simulated mesh cells. The difference between the fiber temperature in Comsol and Matlab is due to the fact, that in Comsol it is not differentiated between the radial and axial thermal conductivity.

2.4.3 Accuracy and Processing Time

As mentioned before, the number of mesh cells can be adjusted in the model but that has an influence on the simulation time. In Fig. 2.17, the simulation time is displayed versus the number of radial elements for the fiber. The air temperature is set to 260 °C and a processing time of 12 minutes is chosen to model. Different numbers of axial elements are coded in different colors. It becomes evident that with increasing number of axial cells the simulation times changes from the range of a few minutes to over 20 min exponentially.

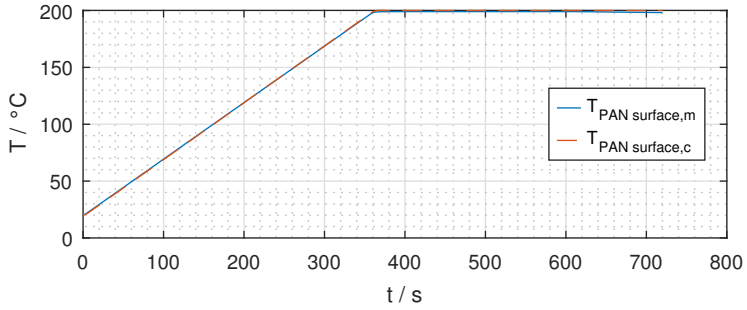

Figure 2.15: Comparison between the temperature profile of the process model in Matlab and a Comsol Model over time for the last mesh cell column at the end of the fiber.

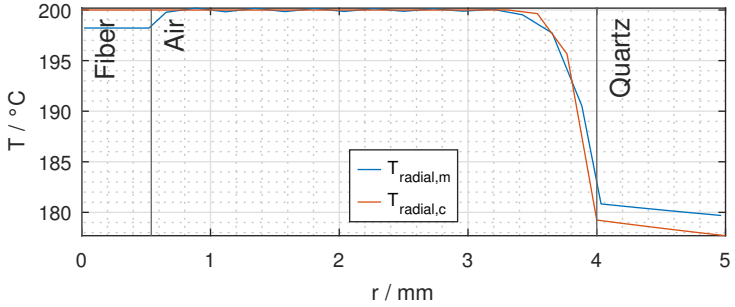

Figure 2.16: Comparison between the radial temperature profile of the process model in Matlab and a Comsol Model.

The number of the radial cells has less influence on the simulation time. To get a result which converges in a reasonable time, in Fig. 2.18 the influence of the mesh cells on the temperature is displayed for the fiber cell at the end of the fiber. The temperature of the air is not completely reached by the fiber temperature as the chosen emission coefficient is high enough to prevent it. The radial elements have no influence on the simulated temperature for a constant value of the axial cells. For the axial cells it becomes clear, that at least 30 cells are needed until the fiber temperature convergence is within 1 °C even for a higher number of axial cells. As the accuracy of the thermocouple utilized in the experiments is in the range of 2.2 °C, it is decided that this accuracy is

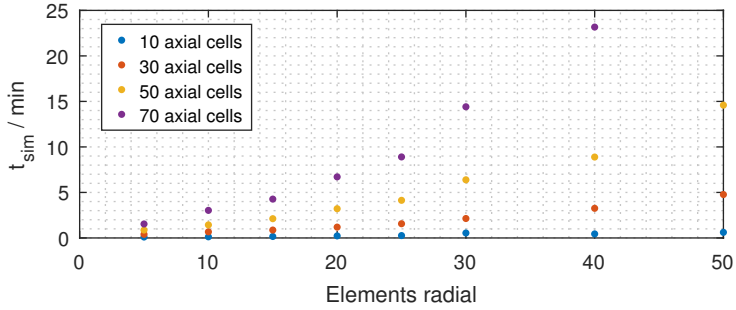

Figure 2.17: Simulation time with increasing number of mesh cells in radial and axial direction.

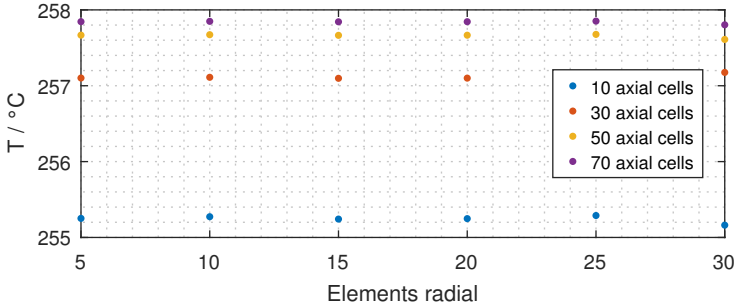

Figure 2.18: Influence of the number of mesh cells in radial and axial direction on the fiber temperature, given for the last mesh cell before the cavity wall at the exit for the surface cell of the fiber.

enough for the modeling. From the results a combination of 30 cells in axial direction and 10 cells in radial direction is chosen.

3 Results

In the following sections, the results of the measurements and modeling obtained in the scope of this thesis are presented. They are divided in results obtained in a batch or stationary process, and the continuous process with a moving fiber.

3.1 Results of Stationary Measurements

Temperature profile over the length

As the thermocouple is later on placed outside of the cavity to not disturb the mode, at first the temperature along the length of the cavity is measured without measuring the quality factor or frequency to verify that a constant temperature is assured inside the cavity. In Fig.3.1, the results for four runs are displayed. In light gray the cavity walls are marked. The temperature drops at the beginning of about 10 °C and at the end of the cavity of even more than 10 °C are due to the cavity wall, the Teflon insulation ring around the quartz tube and the surroundings. For all runs the input temperature is set to 260 °C. Run 1 and Run 2 are done consecutively, as well as Run 3 and 4 one day later. Although the thermocouple is fixed at one end, the tip is able to move slightly in the air flow. This means that the positioning is not completely reproducible, which explains the small differences in the measured temperatures. The temperature shift inside the cavity stays under 10 °C and the process temperature is assumed to be constant in the following.

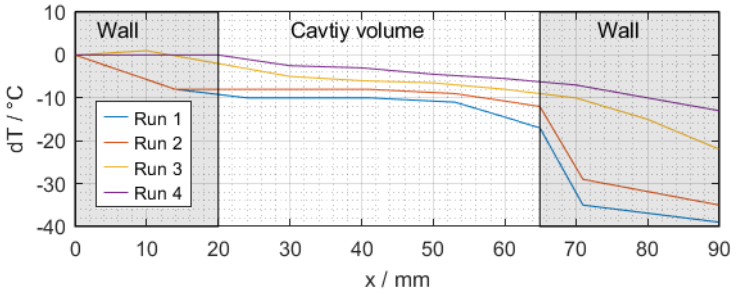

Figure 3.1: Temperature difference along the length of the cavity (adapted from [77]).

3.1.1 Measurement Uncertainties

In this section the measurement uncertainties for the stationary dielectric measurements are shown in Fig. 3.2. They are determined using the eq. 2.8 and eq. 2.9. As can be seen, the uncertainties raise with higher dielectric constants and losses. Over all known errors the loss factor is measured with a relative accuracy of 9.4 % for the virgin PAN fiber. During the stabilization process, the losses rise with increasing temperatures and decrease with the ongoing chemical reaction. The maximum error in the expected range of the loss factor is calculated to be 9.7 %. In the following figures, the uncertainties are not included for easier reading of the measurement values, although, the uncertainties presented in Fig. 3.2 still are to be applied.

3.1.2 Results of Dielectric Measurements in Air

In this section, the results of the performed dielectric measurements are presented and discussed. First the results of an example set of parameters are discussed in more detail before the influence of different process parameters on the dielectric properties are presented. The process parameters that are varied for this purpose are: the heating rate, the process temperature and the holding time, as they have an influence on the reaction progress. If not stated otherwise a heating rate of 30 °C/min is chosen for all measurements. During

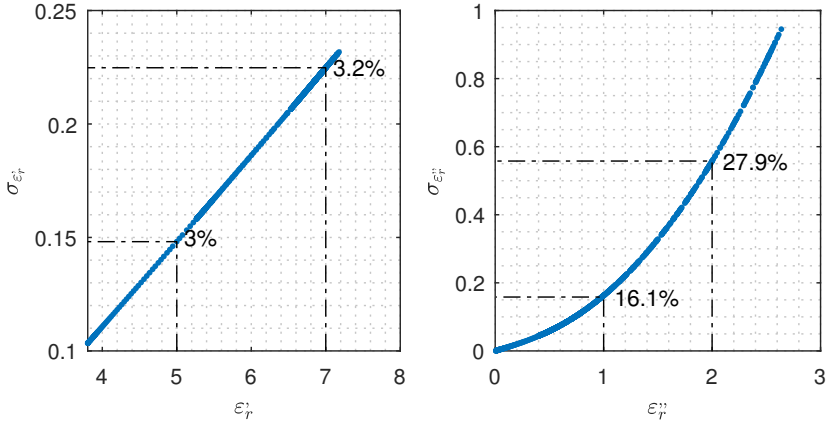

(a) Dielectric constant versus calculated error

(b) Dielectric loss versus calculated error

Figure 3.2: Connection between the calculated errors and the dielectric constant and loss.

the dielectric measurements, the thermocouple temperature measured in front of the entry of the cavity is used as reference value for all measurements.

Dielectric Properties for a Single Parameter Set

In Fig. 3.3, an example for the used process parameters is shown. In the upper graph, the temperature profile is given. A heating rate of 30 °C/min is used (blue line) and a process temperature of 260 °C with a holding time of 70 min (red line) before cooling down (yellow line). In the following graphs, the effect on the dielectric constant $\varepsilon_r^{'}$, the dielectric loss $\varepsilon_r^{''}$ and the loss tangent $\tan\delta$ over time are given, also with the same color code.
The dielectric properties show a strong temperature dependency during the up-heating (blue line). The virgin PAN fiber starts with $\varepsilon_r^{'}$ of 3.80±0.1 and $\varepsilon_r^{''}$ of $8.6{\cdot}10^{-3}{\pm}1.7{\cdot}10^{-3}$. The loss factor rises two orders of magnitude with increasing temperature whereas the dielectric constant rises by about a factor of 1.85 from 3.8 to 7. The changes start at about 100 °C [10] during the heating up phase but continue during the holding time (red line). The loss factor decreases with the ongoing chemical reactions, whereas the dielectric constant nearly remains constant. During the cooling down stage (yellow line),

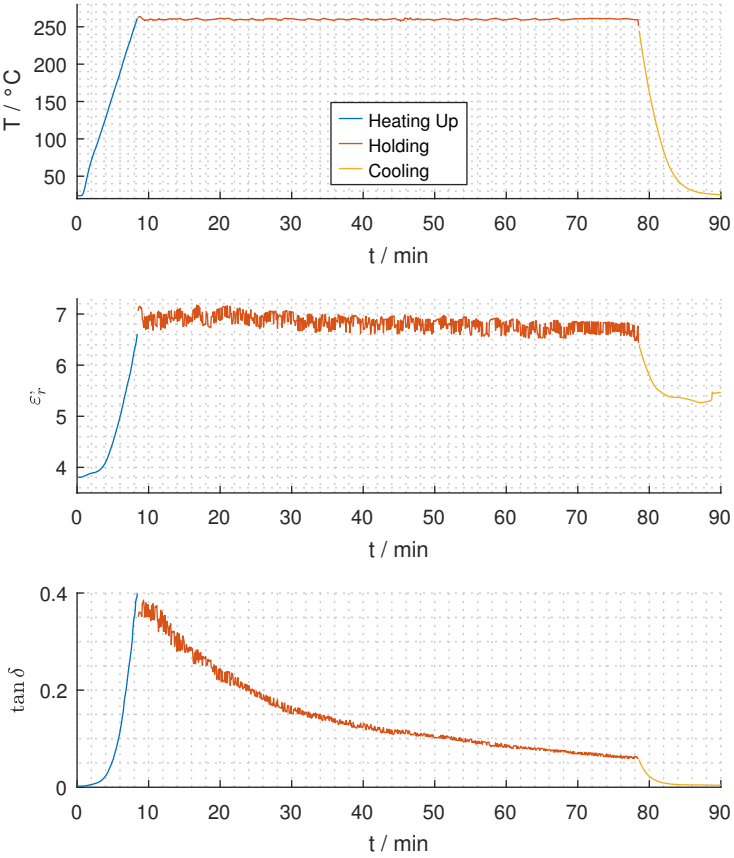

Figure 3.3: Color coded result of dielectric measurement for a heating rate of 30 °C/min, a final temperature of 260 ° and a holding time of 70 min.

the dielectric loss decreases further and ends at 0.022±0.002 which is by a factor of 2.6 higher than before the processing. The dielectric constant also decreases during the cooling down to about 5.46±0.16, which is a factor 1.4 higher than before.

Varying Processing Times

In Fig. 3.4a, the measurement results for a process temperature of 260 °C, a heating rate of 30 °C/min and different processing times can be seen over time. Over all the sets, the strong temperature dependency is the same, as the heat rate is the same. The decrease during the holding time is matching each other in the beginning, showing a good reproducibility. With longer processing times, the dielectric loss is still decreasing, showing that the reaction is still ongoing. The reaction is stopped after the chosen processing time.
Fig. 3.4b shows the differences in dielectric loss and density at room temperature between the virgin PAN fiber at 0 min and after processing for different holding times. The different processing times are distinguishable in the dielectric loss as well as the densities: the longer the processing time, the higher the dielectric loss and density. For shorter holding times a stronger gradient seems to exist between holding times. This could be due to the fact that most chemical changes are taking place at the beginning. The chemical reactions slow down with longer holding times, as most of the molecules have reacted.

Densities in the range from 1.37 g/cm^3 to 1.39 g/cm^3 are given for stabilized fibers by SGL Carbon [78]. Although the exact chemical composition of the used fibers and the SGL carbon fibers is unknown, it is known that both fibers are made from PAN precursors with a PAN content of at least 85 % which influences the overall density. A similar range was proposed by [3]. Densities between 1.36-1.4 g/cm^3 are assumed which depends on the final oxygen content. Similar densities are achieved in the experiments for holding times of 50 min and 70 min. The shorter processing time, compared to industrial ones, which are up to 120 min, is due to the stronger heat rate at the beginning of the process compared to industrial processes where the fiber temperature is increased more slowly, such as 5 °C and 10 °C in [10].

Varying Process Temperatures

In Fig. 3.5, the difference in the development of the dielectric loss for different processing temperatures and the same holding time of 70 min is shown. The heating rate is still set to 30 °C/min although this influences slightly the duration of the heating up phase. Very apparent are the different gradients of the

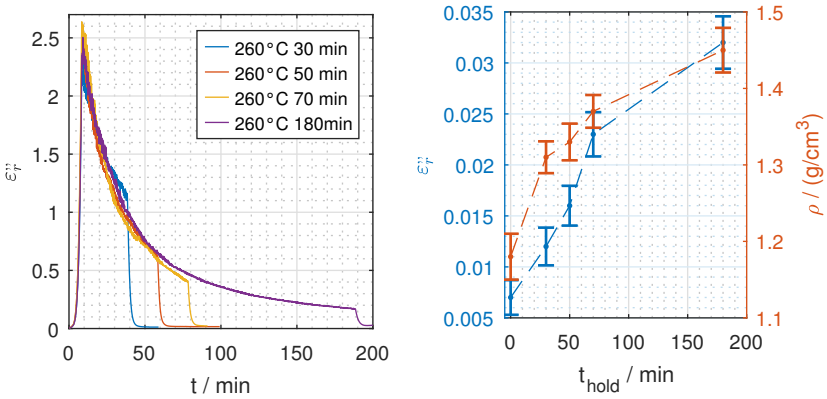

(a) Development of the dielectric loss over time for a temperature profile

(b) Dielectric loss and density before (0 min) and after processing at room temperature

Figure 3.4: Comparison of the dielectric loss and density development with a finale temperature of 260 °C and different holding times.

decreasing of the dielectric loss for the different processing temperatures during the holding time.

Arrhenius proposed in 1889 an exponential relation between the temperature of a reaction and the reaction speed [19]. This leads to the conclusion, that the chemical reaction is taking place at different speeds. After processing, at room temperature, the dielectric loss and density are higher with higher processing temperatures, see Fig. 3.5b.

In Fig. 3.6, long term measurements are displayed. As some parts of the measurement system are exchanged between the measurements and those previously presented, such as the network analyzer, the mounting of the cavity, a bigger quartz tube, a different lab, the maximum dielectric loss differs slightly. This could be due to the fact that the thermocouple placement is changed, leading to a different temperature. Nevertheless, also in this long term measurements, it can be seen, that a higher temperature leads to a steeper decrease of the dielectric loss when the processing temperature is reached.

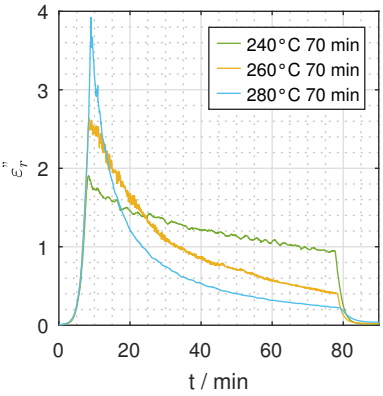

(a) Development of the dielectric loss over time

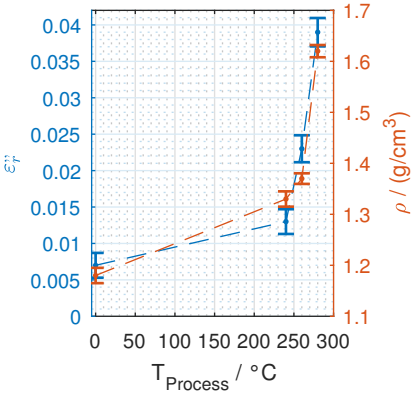

(b) Dielectric loss and density before (0 min) and after processing at room temperature

Figure 3.5: Comparison of the dielectric loss development and density for different process temperatures and a constant holding time of 70 min.

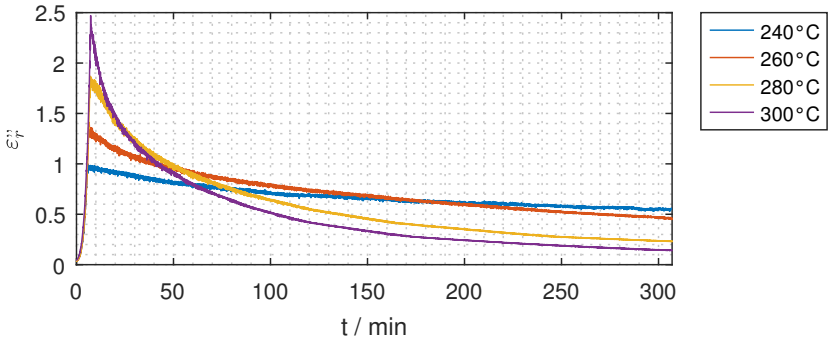

Figure 3.6: Development of the dielectric loss over time, for different processing temperatures and a holding time of 300 min.

Varying Heating Rates

In Fig. 3.7, the effect of varying heat rates on the dielectric loss are shown. Heat rates of 10, 15, 20 and 30 °C/min are chosen. It becomes evident that until around 100 °C only small differences between the four heating rates are visible. According to [79], the glass transition temperature T_g of a PAN homopolymer is in the range of 30 to 104 °C. Similar, in [71], a temperature of approximately 97 to 125 °C is given. The glass transition temperature is the temperature at which a polymer starts to become elastic and stretches easily [5]. Even though, here a PAN fiber with comonomers is used, the starting of an increased spread of the dielectric loss between the heating rates after a temperature of 100 °C could be due to the glass transition temperature. Starting from 140 °C the dielectric loss drifts apart strongly for the different heating rates. According to Heine [10] around that temperature the physical shrinkage is taking place. Between 150 °C and 200 °C, the physical and chemical shrinkage can be overlapping. It can be seen that for slower heating rates, the dielectric loss is raising more than for lower heat rates.

Varying Number of Consecutive Processing

In Fig. 3.8, the measured dielectric loss is shown for multiple processing of the same fiber. The same PAN fiber is heated three times with the same process parameters, a heat rate of 30 °C/min, a holding time of 50 min and a processing temperature of 260 °C, labeled Run 1 to Run 3. The temperature dependency decreases with multiple processing. The biggest difference of the temperature dependency is between Run 1 and Run 2. This is due to the fact that the most of the chemical reaction is taking place during the Run 1. It can be seen even better when it is not shown versus the time but versus the temperature, see Fig. 3.8b. The reduced temperature dependency between Run 2 and Run 3 leads to the conclusion that the dielectric loss of a stabilized fiber, which is chemically transformed, is not as temperature dependent as the PAN precursor, before the chemical reactions take place.

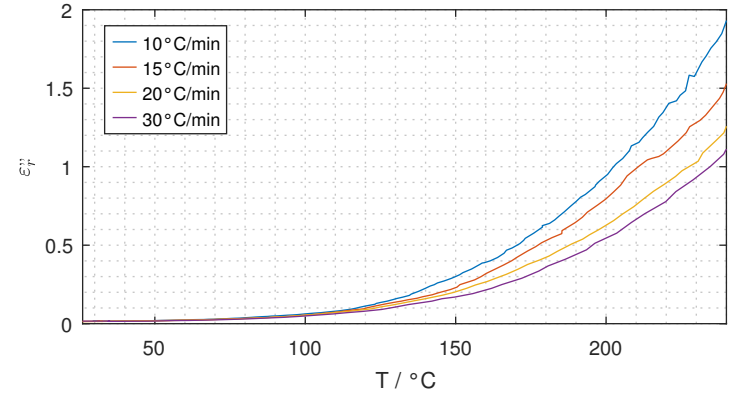

(a) Full view of temperature range of comparison

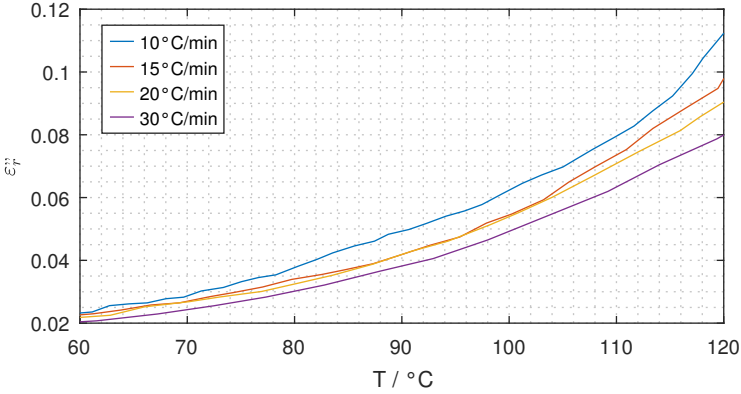

(b) Zoom of temperature range between 60 °C and 120 °C

Figure 3.7: Comparison of dielectric loss as a function of temperature for different heating rates.

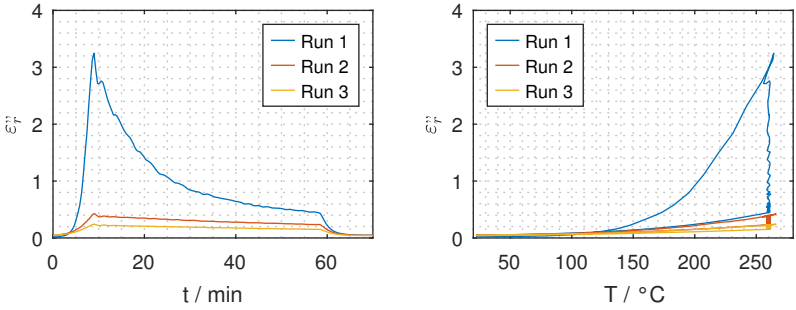

(a) Time dependency (b) Temperature dependency

Figure 3.8: Comparison of the loss factor for consecutive runs of processing the fiber [80].

3.1.3 Results of Dielectric Measurements in Nitrogen

In order to single out the cyclization reaction, N_2 is heated up by the heater and then led through the quartz tube to heat up the fiber. The goal is to see the influence of the cyclization on the dielectric loss. In Fig. 3.9, the optical comparison shows a difference in color. The cyclization is distinguishable from the complete transformation in air as it leads to a more brownish color than the black fiber in air.

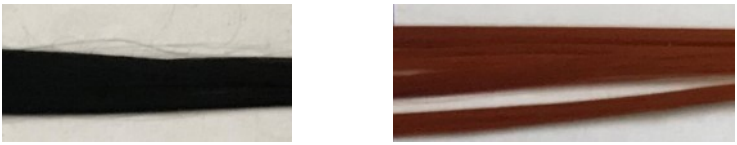

(a) Fiber processed in air (b) Fiber processed in nitrogen

Figure 3.9: Optical comparison of fibers processed in air and in nitrogen at room temperature.

In Fig. 3.10, the dielectric properties of the measurements in air (blue) and N_2 (red) after processing, back at room temperature, are shown for different processing times. The dielectric constant of fibers processed in nitrogen is higher for a holding time of 30 min but lower than the fiber processed in air at 50 min and about the same for a processing time of 70 min. The dielectric loss is higher for the nitrogen processed fiber at 30 and 70 min, and about the same for a processing time of 50 min. This could indicate that the cyclization has a

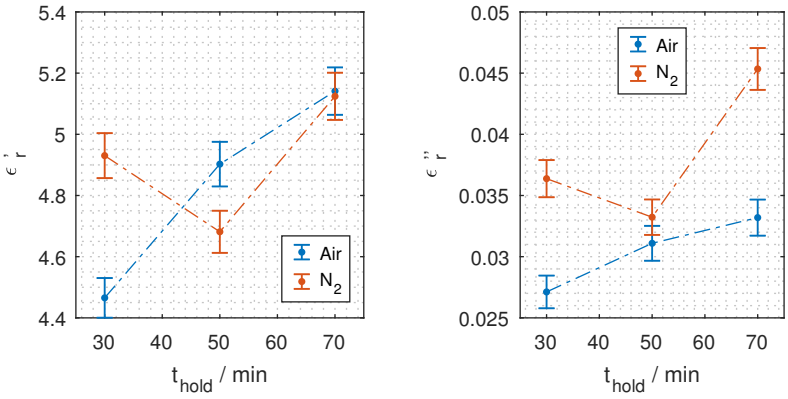

(a) Dielectric constant ε_r'

(b) Dielectric loss ε_r''

Figure 3.10: Comparison of the dielectric properties at room temperature after being processed at 260 °C in air and in nitrogen with different holding times.

larger effect on the dielectric loss. In contrast, the fibers processed in air show an increase in the dielectric properties with longer processing times.
The obtained dielectric properties in nitrogen do not show a consistent behavior at the 50 min processing time mark. One option for the described inconsistency in the results could be due to a difference in temperature. A closer look is taken on the temperature and dielectric loss development over time in Fig. 3.11. The temperature overshooting due to the control is about 4 °C for both curves. Nevertheless, it can be seen in Fig. 3.11b that the dielectric loss differs when the temperature is reached between air and nitrogen from 2.7 to 3.1, respectively. This nearly 15 % increase is followed by a steeper decrease during the constant holding time for nitrogen, which indicates a faster reaction. Another option could be that the fiber tension was not will enough applied, leading to unexpected shrinkage. Measuring the shrinkage could be one option in the future to gather more knowledge.

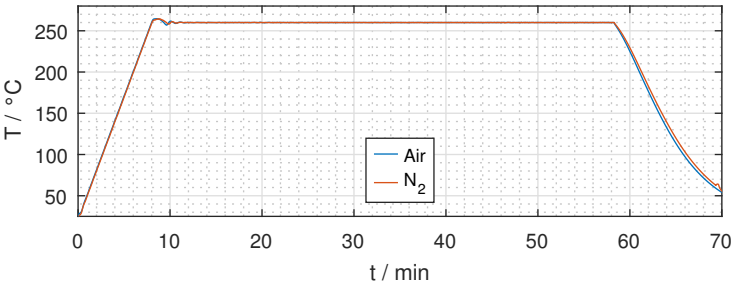

(a) Temperature profile over time

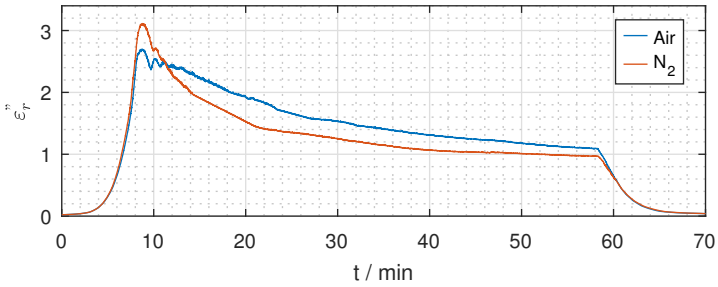

(b) Dielectric loss development over time

Figure 3.11: Comparison dielectric loss in air and in nitrogen with a processing temperature of 260 °C and 50 min holding times.

3.1.4 Stabilization Degree through FTIR

The progression from PAN to a stabilized fiber, also called Oxidized Polyacrylonitrile (PANOX), can be observed in the spectra, see Fig. 3.12. The spectra are taken at room temperature after being processed as described in Chapter 3.1.2. The difference between the different processing times can be seen best at the peak around 1600 cm^{-1} from the C=N bonds, which are formed during the reaction. The other peaks are not as obvious, as the molecules have already existed in the precursor, the concentrations are changing and the peaks of different bonds are overlapping. It can be seen though, that the peaks of the different processing times are in the expected order.
The overlapping, thus broader peaks, can be seen also in Fig. 3.13 where the

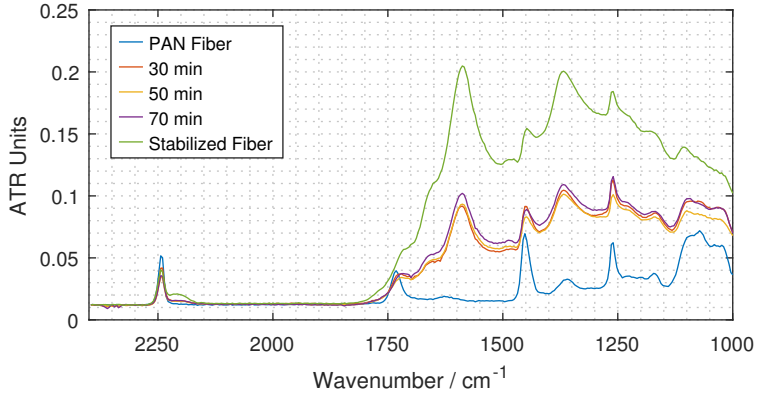

Figure 3.12: Progress of changes in FTIR spectra from PAN precursor and stabilized fiber, processed at 260 °C, FTIR spectra measured at room temperature.

FTIR spectra of a fiber processed in air and a fiber processed in nitrogen, at 260 °C for 50 min holding time, are displayed. The rise around 1600 cm^{-1} is only due to the change in C=N groups for the nitrogen processed fiber and not overlapping with any changes in the other groups.

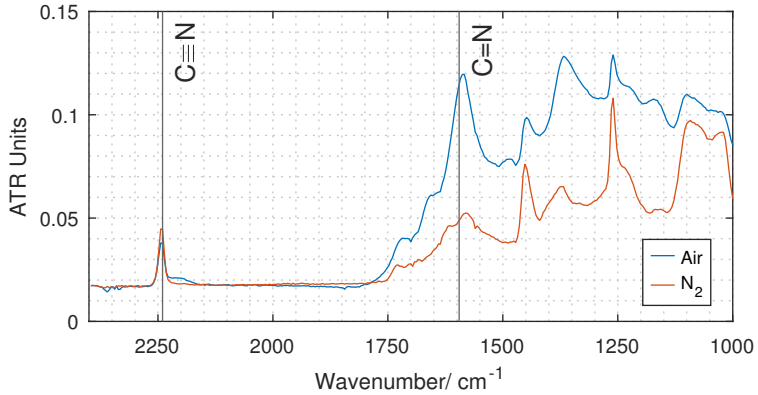

Figure 3.13: Comparison of FTIR spectra of fibers stabilized in air and in nitrogen, processed at 260 °C for 50 min holding time.

With the help of eq. 2.23, the stabilization degrees are evaluated at room temperature after being processed at 260 °C for different holding times and displayed in Fig. 3.14. Each dot represents the mean value of two measurements of the same sample at different positions. Markers at the same holding time, present different measurement runs with the same parameters. The measurement value at 0 min, is obtained from a PAN precursor, which has not been processed. It can be seen that already a stabilization degree of 40 % is measured with this method. Depending on the chemical composition, the fiber can have already some degree of stabilization.
The same slight correlation as with the dielectric loss in Fig. 3.10 can be seen: the stabilization degree of the fibers processed in air, has a tendency to increase with longer processing times. The same is true for the fibers processed in nitrogen, except for a processing time of 50 min. The drop in the stabilization degree for fibers processed for 50 min in nitrogen could be to the same reasons as the drop in Fig. 3.10 as the calculation of the stabilization degree is based on the dielectric loss. For 70 min, the stabilization degree of air and nitrogen is in the same level. The measured stabilization degree at 120 min in nitrogen lies between the 70 min and 180 min stabilization degrees of air.

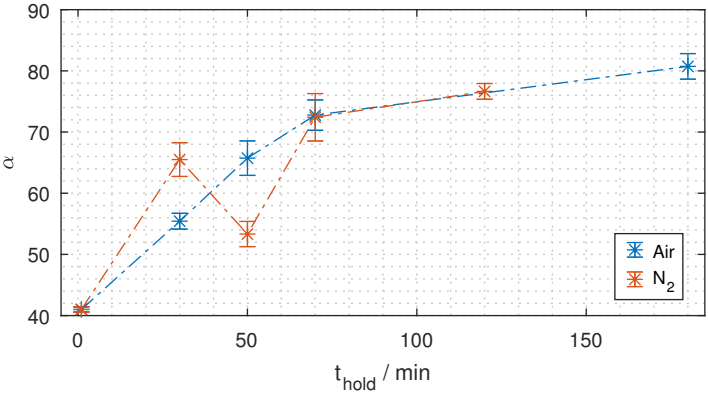

Figure 3.14: Comparison of stabilization degree evaluated by use of FTIR spectroscopy of fibers stabilized in air and in nitrogen at 260 °C.

Comparison of Modeling Results with Measured Dielectric Loss

The process model, set up in Chapter 2, is also tested with a stationary fiber. In Fig. 3.15, the measured dielectric loss is compared to the modeled dielectric loss. The parameters for the model are set to be the same as for the measurement: air temperature of 260 °C, heating ramp of 30 °C/min, stationary, including the exothermic reaction, but no microwave heating. The model fits well to the measured data.

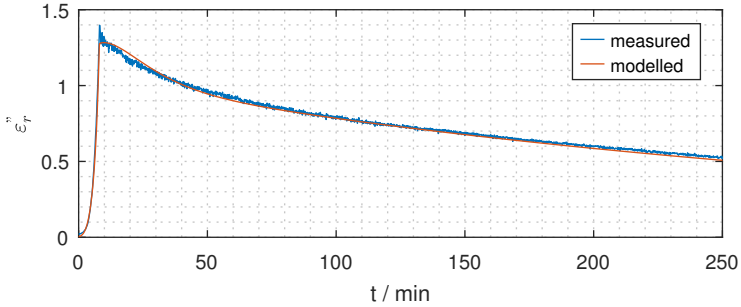

Figure 3.15: Comparison between measured dielectric loss and modeled dielectric loss.

3.2 Results of Continuous Process Measurements

In the following section, results are presented based on a continuous process. The experimental results concerning the color and the process stability are shown.

3.2.1 Process Parameters

As preparation for the experiments, the winding system is used to spin a 3k PAN fiber into a self-spun 12k PAN fiber. The larger fiber bundle is needed for the continuous process as the fiber tensity of the filament winding machine starts at 5 N, where the 3k fiber breaks already when heated.

It is chosen to work in a hybrid mode, combining hot air and microwave heating, to reduce the influence of the strong temperature dependent increase of the dielectric loss. The fiber speed is chosen to be 0.64, 1.28 and 2.56 mm/s, leading to a respective processing time of around 70 s, 35 s and 17 s inside the microwave applicator. The heated air is introduced to the quartz tube before the applicator, so that the processing time in air is longer. The fiber is processed in the heated air, additional to the time, when it is heated also with microwaves. In total the fiber is processed for 123 s , 61 s , 31 s depending on the fiber speed. Air temperatures of 150 °C, 180 °C, 200 °C, 220 °C, and 240 °C are chosen. The air pressure is set to 2 bar and the flow controller is set to 100 ln/min. A weight of 5 N is chosen for all processes. A pre-amplifier with a separate voltage supply is included in the MP2350/700/50MK-A amplifier. It is responsible for the amplification factor of the amplifier and can be varied between 0 V and 5 V. The voltage of the pre-amplifier is set to 4.3 V, assuming a linear correlation with the amplification factor, this results in an amplification factor of 43 dB. The microwave power that is fed into the cavity is varied by changing the bandwidth around the resonance frequency with the help of the network analyzer.

Exemplary Result

An exemplary result with hybrid heating and a continuous process can be seen in Fig. 3.16. A color change from the white precursor to a brownish fiber can be seen. The fiber center is of a darker brown than the borders. This is due to the cooling effect of the air flow and the volumetric microwave heating as well. As the color change is quite visible, and due to difficulties to measure the temperature inside the cavity, in the following section the color is used as an indication to temperature changes and thus the heated amount by the microwave.

3.2.2 Stabilization Degree through Color Study

The exact knowledge of the fiber and air temperatures are key for the process control. Tools to measure the temperature of a moving fiber can be e. g. the infrared (IR) camera and the pyrometer. Using this equipment inside the TM_{010} cavity is not possible, as it is large compared to the used wavelength and would

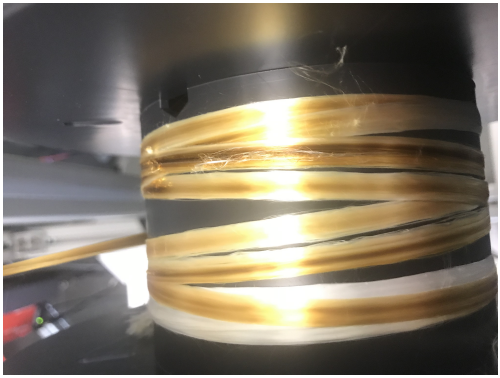

Figure 3.16: Exemplary result of a fiber processed with hot air and microwave heating.

thus disturb the electromagnetic field profile. Using the measurement devices from the outside requires a hole in the cavity wall to focus on the fiber.
The available pyrometer could not look through the quartz tube and measure a temperature of less than 300 °C. Due to those constraints, a second hole in the quartz tube would be needed. A hole in the quartz tube will let the hot air escape. This will lead to a different temperature profile over the length plus heating up the cavity walls, which changes the resonance frequency of the system. Second, in order to be able to drill a hole in the quartz tube, depending on the needed and producible hole diameter, a thicker quartz tube wall is needed, which then in turn influences the electrical field and changes the resonance frequency and quality factor of the system more. It was refrained from drilling a hole in the quartz tube. As alternative, a color study is conducted to get more information on the temperature increase that is obtained by microwaves over the width of the fiber. It is executed as follows: A series of fibers is processed in air without the microwave at different speeds and air temperatures. This series lead to a color reference schema which could then be used to match the color of a hybrid processed fiber to a temperature.

An example of the conventionally processed fibers with different air temperatures and fiber speeds can be seen in Fig. 3.17. It can be seen that with higher temperatures and longer processing times, thus lower speed, the color of the fiber turns from nearly white to yellow to light brown to dark brown. The same color changes can be also observed with ongoing reaction. The color

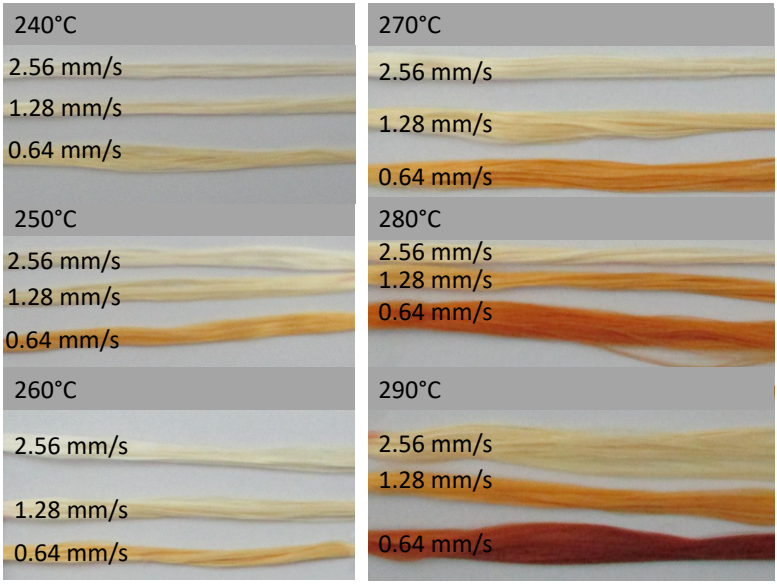

Figure 3.17: Example of conventionally processed fibers with different gas temperatures and fiber speeds and its resulting color changes.

of these fibers builds the reference for the color study. Each parameter set is photographed under the same lighting conditions with a Rebel Xsi camera from Canon and then uploaded in Matlab. The color code is extracted. The resulting color reference scheme can be seen in Fig. 3.18. The reference is then used to compare the color change of the hybrid processed fibers.

The example in Fig. 3.19 is conducted with an air temperature of 220 °C, a processing speed of 2 mm/s and a bandwidth for the network analyzer of 17 MHz. That results in a maximal forward microwave power of around 22 W. The mean absorbed power in the system is around 4.5 W, see eq. 2.28. A picture of the hybrid processed fiber is taken under the same conditions as the reference, see Fig. 3.18. The points for comparison are chosen manually in Matlab, see Fig. 3.19a. Around each color at least three points are used of which the color is extracted, see Fig. 3.19b. The obtained colors are compared to the reference colors of the same speed. According to the reference scheme, the inner part of the fiber has a temperature of 260 °C during processing.

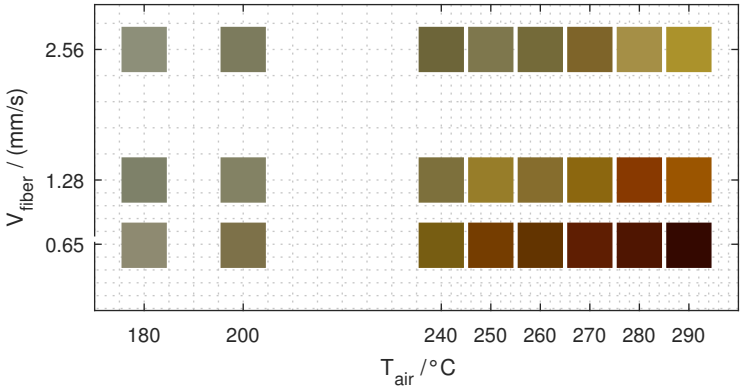

Figure 3.18: Reference schema of the color study.

The outer points have a temperature of 250 °C. Thus the microwave heated at least 30 to 40 °C on top of the hot air flow. This extraction of temperature has some limitations and is thus only a preliminary method to get an idea of the temperatures that are reachable. The accuracy of the results depends on the points picked, as well as the placement of the thermocouple for the temperature measurement both during the reference and also the experiment. In the reference schema, the reference color is determined only for temperature steps of 10 °C and higher. Thus, the temperature of the comparison points can not be more precise than those 10 °C steps either. A difference of 5 °C would not be visible in the results. The taken pictures of the fiber could also influence the results e. g. if the angle is slightly different then the light diffraction might be changed. This could occur if the fiber is not completely flat on the surface.

3.2.3 Process Instability

In this section, the bandwidth, and thus the microwave power, is adapted for different sets of process parameters until it leads to an unstable process, which is defined as a burnt and thus broken fiber.

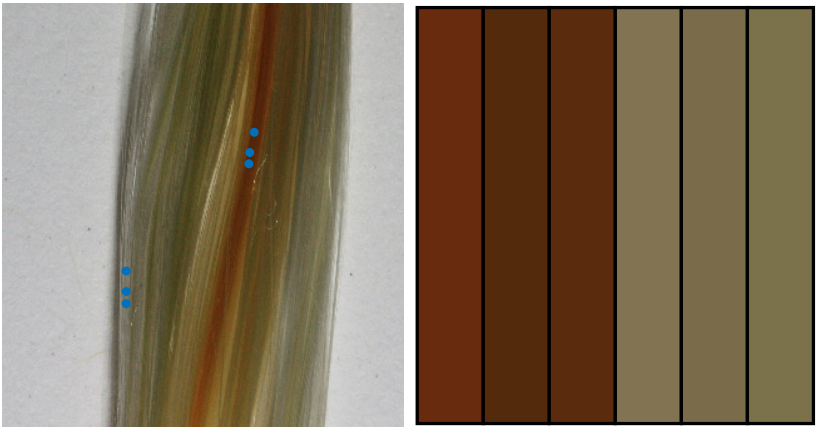

(a) Choosing points by hand (b) Resulting color

Figure 3.19: Steps of the color study a) choosing points b) extracted colors which are compared to reference.

Experimental Results

The uncertainty of the power measurements is calculated according to eq. 2.7, leading to 6 % measurement uncertainty for the incoming and reflected power. The experimental results are shown in Fig. 3.20. The mean power level P_{mean} at which the fiber breaks is given, as well as the air temperatures applied. From Fig. 3.20 it becomes evident that the results are scattered and only a tendency of the behavior can be extracted. Each dot represents a measurement. In black a trend line is shown. The correlation can be best seen for fiber speeds of 1.28 mm/s and 2.56 mm/s. With higher fiber speeds the mean power level increases slightly with the same air temperature. This is to be expected, as a faster moving fiber requires more energy to heat the fiber in a short time to the breaking temperature. With higher air temperatures the mean power level decreases when the fiber breaks. The lower mean power required for higher air temperatures is also to be anticipated as less microwave energy will have a larger impact on the heating due to the increased dielectric loss as presented in Chapter 3. The results for a fiber speed of 0.64 mm/s do not behave as expected. A possible reason is the fact that at this low speed the fiber winding

had some difficulties so that the fiber movement sometimes stopped, which is optically observed.

Wall losses

The absorbed power is left in the complete system, thus it includes losses at the cavity wall. A simulation can help to separate the different beneficiaries of the absorbed power. It was assumed that the fiber is heated up, thus has high dielectric losses. With the help of a CST simulation, it is estimated that around 6 % of the absorbed power is absorbed in the cavity walls, see Fig. 3.21.

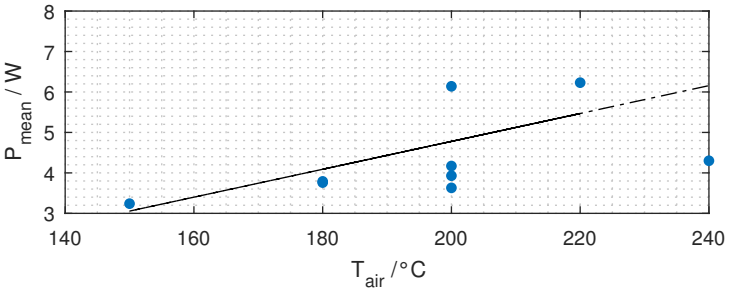

(a) Results for a fiber speed of 0.64 mm/s

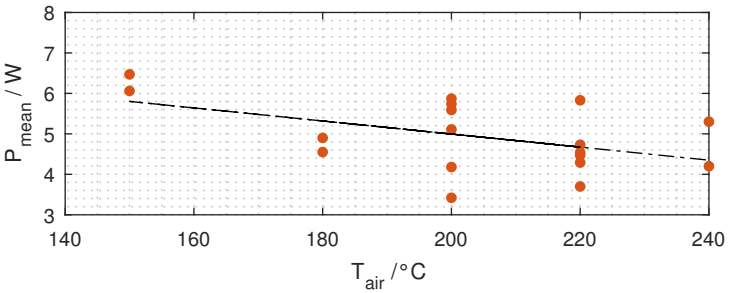

(b) Results for a fiber speed of 1.28 mm/s

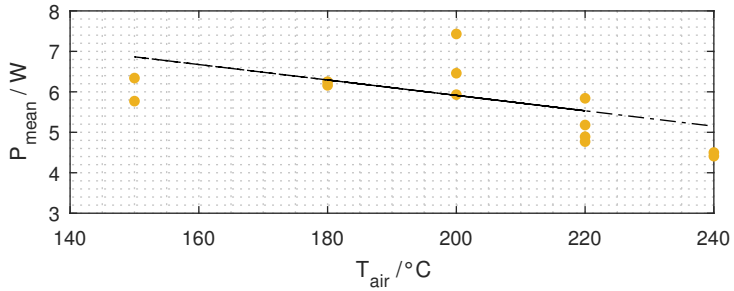

(c) Results for a fiber speed of 2.56 mm/s

Figure 3.20: Experimentally obtained values when the fiber is breaking, comparing the mean power for different fiber speeds.

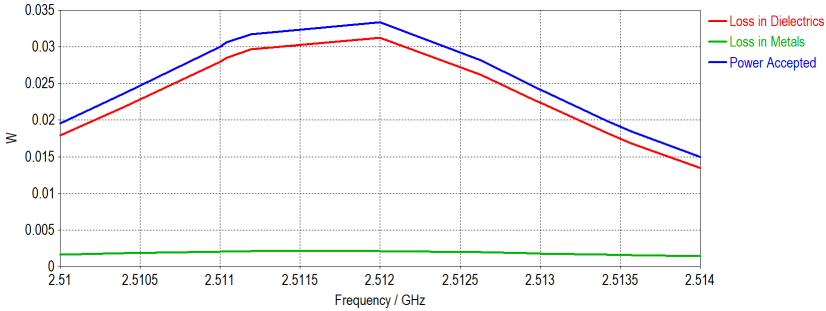

Figure 3.21: CST simulation result for the wall losses, in blue the accepted power inside the system is shown, in red the losses inside the fiber and in green the losses in metals, thus the wall losses.

4 Discussion of the Measured and Modeled Results

In the following chapter, different aspects of the measurement results in Chapter 3 are discussed further. Possible sources of errors such as improvements in the measurements are mentioned. Some results are extended to setup new strategies.

4.1 Dielectric Measurements

In Chapter 3.1, the results of the stationary measurements are presented. It becomes evident that a longer processing time results in a higher degree of chemical transformation, thus a higher stabilization degree. This is not only reflected in the dielectric losses but also the density. The changes in the dielectric loss are strongly temperature dependent and the chemical change is well traceable when the temperature is kept constant. The variation is sufficient to enable the modeling.

Also, as mentioned in Chapter 2.3, the accuracy of the measurements is strongly dependent on the temperature measurement. The accuracy could be improved by a better fixation of the thermocouples. The quartz tube can not be replaced as it is needed to guide the air flow and keep the temperature constant along the length. An insulation inside the cavity might help with any changes over the length in the cavity, but the material would have to be microwave transparent. Even better would be to ensure vacuum inside the cavity. As a vacuum pump and other equipment is needed, this could be tested in future experiments if a more homogeneous temperature inside the cavity is needed.

4.2 Reaction Kinetics

In order to obtain the necessary information between the dielectric loss and the stabilization degree or reaction kinetics, different approaches are possible:

- separation of the individual reactions to see their influence on the dielectric loss,
- determination of the stabilization degree of samples with known dielectric loss,
- direct modeling to multiple data sets for the dielectric loss.

As mentioned before, multiple reactions are taking place during the stabilization stage. As the oxidation and dehydration need O_2, the cyclization can be separated from the other two by using a nitrogen atmosphere instead of oxygen. Thus as a first step dielectric measurements are performed in a N_2 atmosphere. Due to the results in Chapter 3.1.3 and 3.1.4, this approach is not followed further. The direct modeling is explained in more detail in the upcoming section.

4.2.1 Derivation of a Mixing Rule

A mathematical model is setup and directly fitted to experimental dielectric data for different temperature profiles. First the mathematical model is presented. The dielectric loss can be connected to the degree of conversion by the usage of mixing rules. The mixing rules describe how to calculate the effective permittivity of non-homogeneous materials, consisting of a mixture of the original material and the completely transformed material. The shape of the mixed materials, such as spheres or ellipsoids, or homogeneous materials, also play a major role in the calculations [81, 82]. It is chosen to consider the PAN fiber and its transformation stages through the chemical reactions as homogeneous materials.

In a simple scenario, a compound A is transformed into a product C. An effective dielectric loss $\varepsilon''_{\mathrm{eff}}$ is defined which describes the change of the dielectric loss $\varepsilon''_{\mathrm{A}}$ of the material before the reaction took place to the dielectric loss $\varepsilon''_{\mathrm{C}}$ of

the material after the reaction, depending on the degree of conversion α. Different options for calculating the effective permittivity are available from the mixing rules, see [81]. But in a first step it is chosen to use a linear approach, which is expressed as follows [81]:

$$\varepsilon''_{\mathrm{eff}} = \varepsilon''_{\mathrm{A}} - \alpha \cdot \varepsilon''_{\mathrm{A}} + \alpha \cdot \varepsilon''_{\mathrm{C}} = (1-\alpha) \cdot \varepsilon''_{\mathrm{A}} + \alpha \cdot \varepsilon''_{\mathrm{C}}. \tag{4.1}$$

As multiple reactions take place during the stabilization and a separation of the parallel reactions is not successful from a dielectric point of view, the reaction order is simplified for the model. Only two consecutive reactions are considered. It is assumed that, as the dehydration and the cyclization are taking place at the same time, they can be considered as one reaction in the model.
A schematic of the derivation of the connection between the reaction kinetics and the dielectric loss can be seen in Fig. 4.1. Eq. 4.1 is thus extended for a second reaction by introducing an intermediate product material with the dielectric loss $\varepsilon''_{\mathrm{B}}$. Now, there are two degrees of conversion, one for every partial reaction. If the second reaction is not taking place, thus $\alpha_2 = 0$, the overall effective dielectric loss is equal to the dielectric loss of the intermediate product $\varepsilon''_{\mathrm{B}}$. The effective dielectric loss of the second reaction can thus be inserted in the first reaction, instead of $\varepsilon''_{\mathrm{B}}$ to obtain the overall dielectric loss. The final equation for the overall dielectric loss $\varepsilon''_{\mathrm{eff,sum}}$ is stated as:

$$\varepsilon''_{\mathrm{eff,sum}} = (1-\alpha_1) \cdot \varepsilon''_{\mathrm{A}} + \alpha_1 \cdot (1-\alpha_2) \cdot \varepsilon''_{\mathrm{B}} + \alpha_1 \cdot \alpha_2 \cdot \varepsilon''_{\mathrm{C}}, \tag{4.2}$$

where $\alpha_{1,2}$ can be replaced by eq. 2.18. As the dielectric properties show a temperature dependency - as mentioned before - the following equation is used to describe the dielectric losses:

$$\varepsilon''_{\mathrm{A,B,C}} = c_{\mathrm{A,B,C}} \cdot e^{-\frac{b_{\mathrm{A,B,C}}}{T}}, \tag{4.3}$$

where $c_{\mathrm{A,B,C}}$ and $b_{\mathrm{A,B,C}}$ are constants. The final equation, that is used for the parameter fitting, is combining eq. 4.2, eq. 4.3 and eq. 2.18 as well as eq. 2.14 which results in the possibility to obtain the desired reaction kinetics parameter, the pre-exponential factor k_0 and activation energy E_a for each reaction directly through the fitting to the measurements.

In order for the model to work, it has to be assumed that the fiber has the same temperature as the hot air around it. Thus in the heating up stage, the fiber

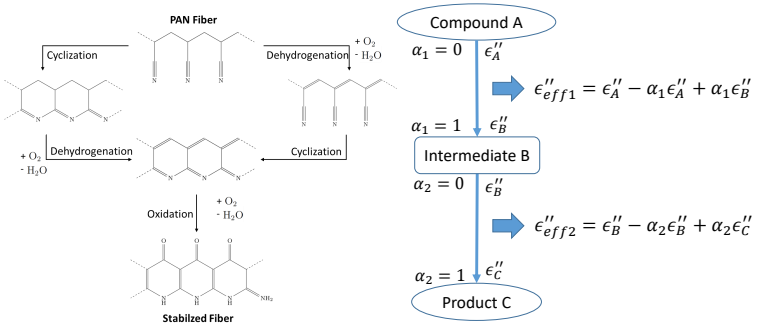

(a) Correlation of reactions and the dielectric loss [67]

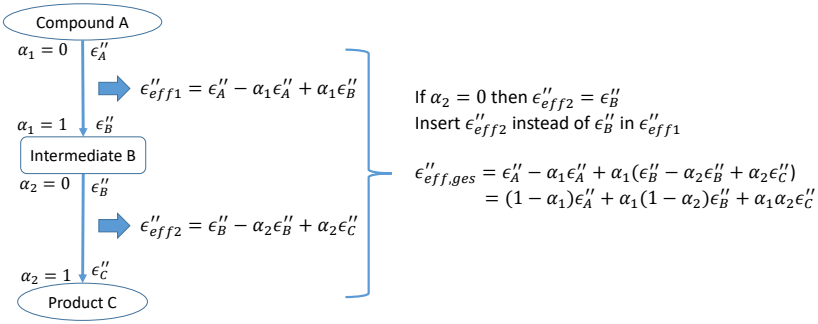

(b) Calculation of the overall dielectric loss

Figure 4.1: Schematic of the setup of the correlation between the chemical reactions and the effective dielectric loss.

has the same temperature as the air temperature at that time step. During the holding time the fiber temperature equals the air temperature as well. It is also presumed that any excess temperature from the exothermic reaction is cooled away instantly, so that the fiber temperature is always constant.

4.2.2 Comparison Fit with Experimental Results

For the fitting, long term measurements are done first, as it can be assumed that the reactions come to an end after a certain time, see Fig. 3.6. Then the aforementioned equations, eq. 4.2, 4.3 are used to fit the reaction kinetics parameters of the two Arrhenius equations, eq. 2.14 and the constants to the measured long term dielectric properties. The fitting toolbox of the software Matlab [83] is used to fit the parameters. The results can be seen in Fig. 4.2 for a linear scale (on the top) and a logarithmic scale (on the bottom). The fitted values are reasonably close to the measured values. The divergence is mostly within the error margin. Only for the data of 280 °C, some modeled values are about 7 % higher. For the data of 300 °C, the dielectric loss smaller than 10^{-2} diverges from the fitted values in the logarithmic display. The logarithmic display is plotted against the threshold towards which the fitted values converge. In case of the data of 300 °C the fitted threshold is not a good fit with the measured data for small values, thus leading to a deviation.

The obtained values including the 95 % confidence interval can be found in Table 4.1. The activation energies are in a similar range as the values provided by Baddi et al. [17], see Table 1.1, for the cyclization and the reduction processes. An activation energy of around 82 kJ/mol is given for the cyclization, compared to roughly 98 kJ/mol and around 40 kJ/mol for the reduction compared to 39 kJ/mol. Of course, the exact value can not be compared as the exact chemical compositions are not known.

Temperature influence

Although the agreement of the measured and simulated values in Fig. 4.2 is very good, the importance of the precise temperature measurement can be verified. It was already mentioned earlier that the fiber temperature is not only increasing when heated in conventional ovens but also through the exothermic reactions. In conventional ovens, the temperature is controlled thoroughly through multiple heating zones. In the experimental setup, a thermocouple is used to measure the air temperature, but the reproducibility of the thermocouple placement inside the quartz tube is not always sufficient. The temperature offset through the thermocouple as well as the exothermic reactions lead to variations of the real fiber temperature, especially between different measurement series.

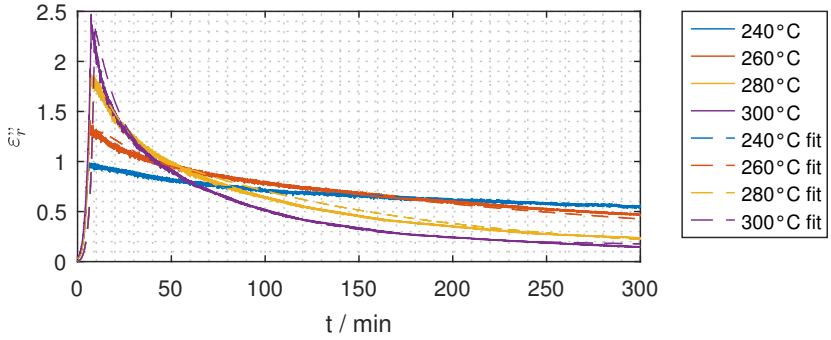

(a) Linear diagram

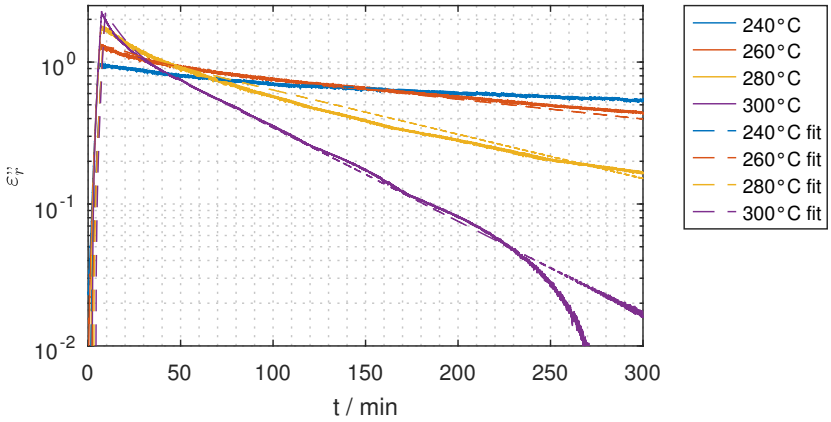

(b) Logarithmic diagram

Figure 4.2: Comparison of measured (solid lines) and modeled (dashed lines) dielectric loss for different temperatures [67].

Parameter	Value	Unit	Confidence Interval	
$k_{0,1}$	$2.44{\cdot}10^5$	1/s	$2.36{\cdot}10^5$	$2.52 \cdot 10^5$
$E_{a,1}$	98.56	kJ/mol	98.42	98.72
$k_{0,2}$	10.2	1/s	9.5	11
$E_{a,2}$	39.2	kJ/mol	38.86	39.52
c_A	1083	-	1068	1099
c_B	3689	-	3681	3696
c_C	2511	-	2115	2907
b_A	2572	K	2485	2658
b_B	$14.5{\cdot}10^8$	K	$9.2{\cdot}10^8$	$19.8{\cdot}10^8$
b_C	$13.1{\cdot}10^3$	K	$12.9{\cdot}10^3$	$13.3{\cdot}10^3$

Table 4.1: Values obtained for the reaction kinetics model [67].

Multiple processing with the same process parameters are conducted. The dielectric loss variations for different runs due to temperature inaccuracy can be seen in Fig. 4.3. The impact is shown for 260 °C and 280 °C. Run 1 refers to the same data as in all following subfigures depending on the temperature (same data $\widehat{=}$ same color).
From Fig. 4.3a and Fig. 4.3b, it is obvious that the dielectric behavior differs significantly over time for the respective runs. The evaluated kinetic parameters for Run 1 will not lead to a good fit for the Run 2 and it can be assumed that the effective temperature in each run is different. The measured temperature is nearly identical as can be seen in Fig. 4.3c and Fig. 4.3d. This is to be expected as the temperature control is set to the preset values. The temperature overshoots are due to the PID controller. This can be due to not ideal PID parameters. Even though the PID parameters for those measurements are set to be the same, a displacement of the thermocouple could lead to a slightly changed temperature measurement, affecting the chosen PID parameters. Even though, the repositioning of the thermocouple was tried to be as accurate as possible, it was done by hand and it is possible that the positioning of the thermocouple is not identical resulting in an effective temperature which is different from the one actually measured.
In order to enhance the fitting of Run 2 and validate the assumption, a new variable T_offset, describing a temperature offset, is utilized to fit the obtained

reaction kinetics parameter to the data of Run 2. In eq. 2.14 and eq. 4.3 the temperature is replaced by $T + T_{\text{offset}}$. According to the fit of the temperature offset, the effective temperature of the 260 °C data in Run 2 is higher by 7.7 °C whereas for the 280 °C data it is lower by 9.7 °C than the temperature in the respective first runs. The resulting fit for Run 2 of 260 °C and 280 °C can be seen in Fig. 4.3e and 4.3f, respectively. The fact that both Run 2 are closer to a temperature of 270 °C is also supported by the peak of the dielectric loss which is in both cases around 1.5. The reasonably close fit with a temperature offset validates the assumption that the temperature measurement and thus also the placement is a major source of uncertainty. It can be concluded that the temperature measurement needs to be improved in the future.

Stabilization degree

With the obtained values for the reactions kinetics, it is now possible to look at the connection between the dielectric loss and the stabilization degree. In Fig. 4.4, the stabilization degree of the effective reaction kinetics is displayed versus the time for a heating ramp of 30 °C/min and a holding time of 300 min, while the process temperature is set to 260 °C in Fig. 4.4a and 300 °C in Fig. 4.4b. The original material with dielectric loss ε''_{A} (blue line) declines while the intermediate (red line) and final products (yellow line) increase. The intermediate product with dielectric loss ε''_{B} is transformed directly into the final product ε''_{C}, once it is formed. This shows the immediate correlation between the reactions and the difficulty to separate the reactions from a dielectric point of view. Also it can be very well seen, that with 260 °C, after 300 min, the stabilization degree only reaches about 60 % while it has nearly completely reacted for a temperature of 300 °C.

In Fig. 4.5, the FTIR results are compared to the model for a temperature of 260 °C. The degree of the cyclization obtained with the FTIR spectroscopy are around 0.1 higher than the modeled results. Even though a similar course can be seen, this shows again the difficulties, when obtaining and comparing stabilization degrees, also with literature values.

The usage of the dielectric properties in an industrial process to determine the fiber quality is, with this knowledge, possible but will require a calibration consisting of dielectric measurements and the fit of the reaction kinetics for

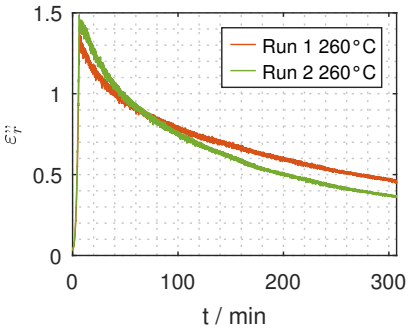

(a) Comparison dielectric loss for 260 °C

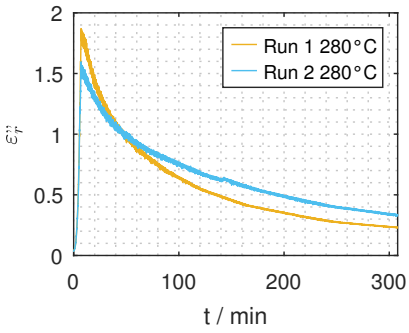

(b) Comparison dielectric loss for 280 °C

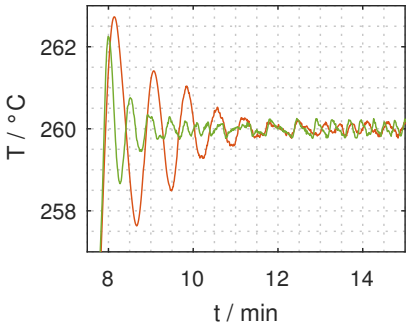

(c) Closeup of temperature profile at 260 °C

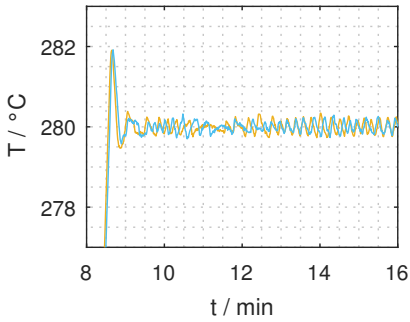

(d) Closeup of temperature profile at 280 °C

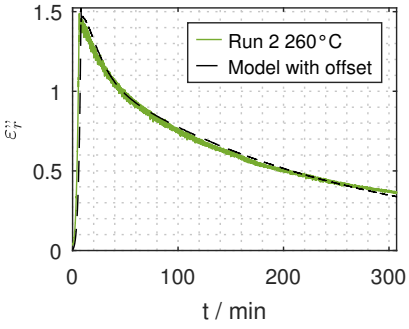

(e) 260 °C fit with temperature offset

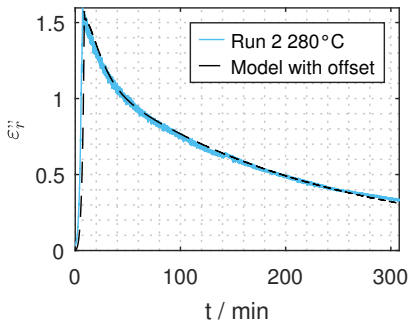

(f) 280 °C fit with temperature offset

Figure 4.3: Dielectric loss of the same process parameters measured at different days and fit with temperature offset [67].

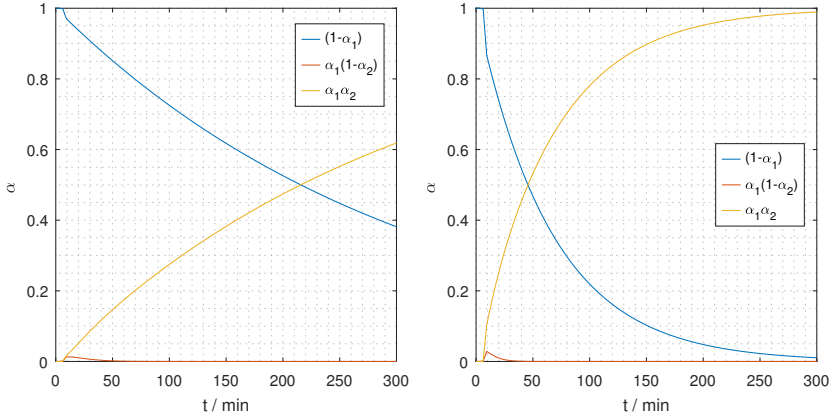

(a) 260 °C (b) 300 °C

Figure 4.4: Development of the modeled stabilization degree α for a temperature profile with a heating rate of 30 °C/min and a holding time of 300 min and different process temperatures [67].

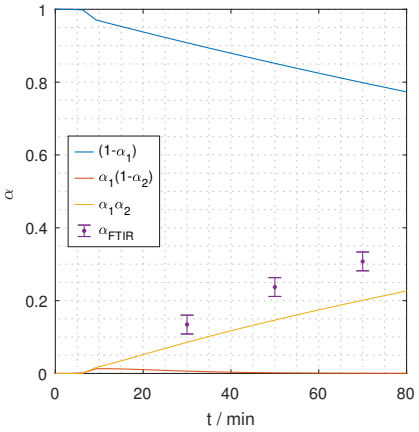

Figure 4.5: Development of the modeled stabilization degree α for a temperature profile with a heating rate of 30 °C/min and a holding time of 300 min and a process temperature of 260 °C compared to the stabilization degree obtained from FTIR measurements.

different chemical compositions. Additionally, a calibration needs to be made to correlate the dielectric stabilization degree with the produced material. Usually the stabilization does not need to be finished completely before the fiber goes on to the carbonization. Furthermore, to avoid the overheating of the fiber in industrial production, the fiber must pass multiple heating zones to slowly increase the temperature. This has also to be respected in the calibration. A higher heating rate in this work is chosen in a first step to decrease the time of the chemical transformation in the heating up stage. The approach presented in this work uses simplifications and trade-offs. Possible revisions from the simplifications are:

- Simplification: Combining dehydration and cyclization to one reaction
  Revision: Separate the reaction kinetics with the help of other methods, such as DSC measurements, to determine the activation energy and pre-exponential factor.

- Simplification: Assuming that the air and fiber temperature are equal
  Revision: Extend the measurement setup to allow the measurement of the fiber temperature e. g. through fiber Bragg sensors. Then a separation of the actual fiber temperature from the air temperature is possible and can be introduced in the model. This might also be followed by an exchange of the function of the degree of conversion [60].

- Simplification: Using only a linear approach as mixing rule for the effective dielectric loss
  Revision: Different mixing rules, such as e. g. Power Law model, Lichtenecker formula, Maxwell-Garnett-Rule [81] could be an option to calculate the effective dielectric loss of the two parallel reactions. Also the influence of the hot air flow between the filaments could be taken into account with the help of the mixing rules. As it is shown in 1.2, second order reactions use oxygen as catalysator for the reactions.

- Simplification: Assuming that the reaction is finished after 300 min of processing
  Revision: Determine the degree of conversion after 300 min through other tools, such as DSC or FTIR measurements, to determine the degree of conversion. This may help to get a better understanding of the oxidation and its reversible reaction, the reduction reaction. It is pos-

sible, that there is no definite end of the processing as oxidation and reduction are in balance.

- Simplification: Leaving out the influence of the cooling of the quartz tube on dielectric measurements
  Revision: Including calibration measurements for the cooling down phase, for different ambient temperatures and their effect on the quartz tube cool down behavior. This allows to include the temperature dependent dielectric properties of the stabilized fiber without further processing of the fibers.

A first reaction kinetics model has been proposed and gives results that are in good agreement with literature and the measured data. The assumptions and simplifications that are made can be refined in future work if dielectric properties are used as measurement method for the stabilization degree in industry.

4.3 Process Model

The susceptibility of the stabilization process parameters for microwave heating is, to the knowledge of the author, not been well documented. However, understanding the impact any change of the process parameters has on the fiber temperature, is helpful to setup the experimental layout. Process parameter ranges and accuracies can be investigated beforehand through simulation with the process model. In this section, the process parameters are varied in a certain range and its effect on the temperature are tracked. The fiber speed, air temperature, and microwave power are used as parameters. In the following section, the goal temperature for the stabilization process is assumed to be 260 °C±5 °C. The melting point, according to [79] is around 320 °C for the homopolymer PAN. In this work a precursor including copolymers is used. For this reason, as a worst case scenario, the abortion criteria for the simulation is set to temperatures above 340 °C. The simulation is stopped once this temperature is reached and the process declared as unstable.

As an example for an air temperature of 200 °C, the temperature of the last most inner axial mesh cell, in the center of the fiber, see Fig. 2.14, is visualized in Fig. 4.6. On the x-axis the electric field resulting from the applied microwave

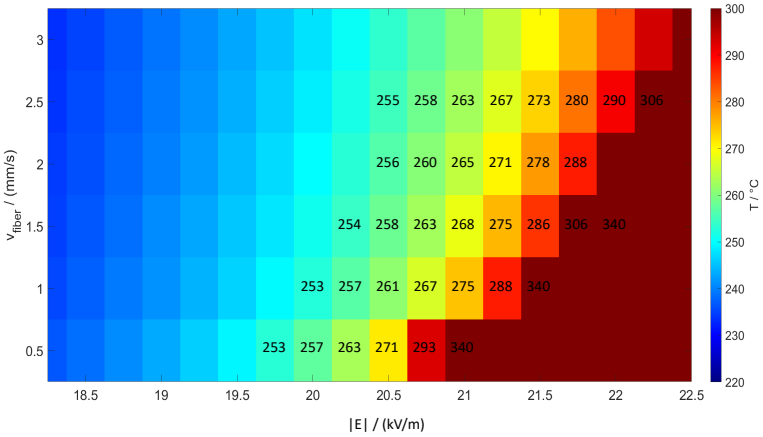

Figure 4.6: Simulated influence of the variation of process parameters on the temperature of the last cell element inside the fiber for an air temperature of 200 °C.

heating with different power levels is shown and on the y-axis the fiber speed. The electrical field is increased in 0.25 kV/m steps and the fiber velocity in 0.5 mm/s steps. Temperature readings of a few selected cells are added in the figure to facilitate the understanding of the impact and as the color legend uses steps of 10 °C.

First, it can be noticed that a few parameter combinations fulfill the requirement to reach 260 °C±5 °C. Second, for lower fiber speeds, every increase in the electrical field, results in a larger temperature increase. This is due to the higher dielectric losses at higher temperatures. But it also shows, that with every increase it is more likely for the process to become unstable. The nonlinear increase in temperature can be an indicator for the thermal runaway effect which was already mentioned in Chapter 2 and is a common control problem in numerous microwave heating applications [84]. However, with the help of a mathematical analysis some stability criteria or stable ranges can be found. For low fiber speeds, the desired 260 °C are close to the instability. A 0.25 kV/m increase can result in temperature increases of 10 °C and more. While higher fiber speeds are better to achieve the desired temperature, it also has to be kept in mind, that a faster speed translates to a longer applicator design if the processing time is supposed to be the same.

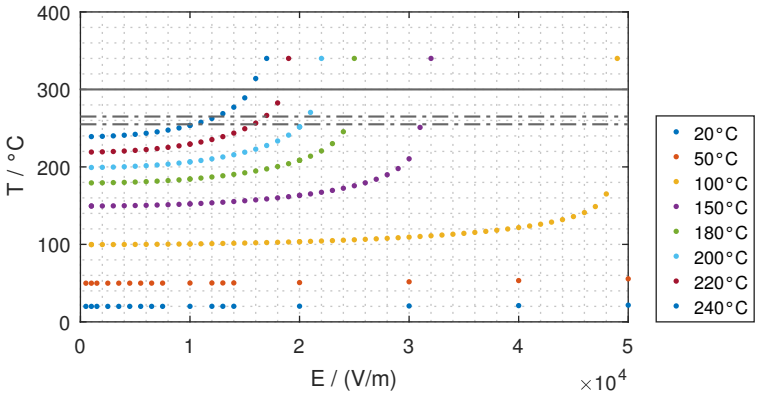

Figure 4.7: Simulated influence on fiber temperature at cavity exit with a fiber speed of 1.28 mm/s and varying air temperature and microwave power.

Through the air temperature surrounding the fiber, the range of stable process parameters is also impacted as well as the precision needed for each parameter. In Fig. 4.7, a fiber speed of 1.28 mm/s is chosen, the air temperature and the microwave power are varied to investigate the influence on the fiber temperature. The temperature displayed refers to the last most inner mesh cell at the end of the fiber. The desired temperature range is marked with dashed lines, between 255 and 265 °C. The solid line shows again the 340 °C mark where it is assumed that the fiber melts resulting in a broken fiber. It becomes evident that for air temperatures of over 200 °C the desired range is achievable more easily, as at least one simulation point is in the desired range and the curvature of the simulation points is not yet in the critical range of process parameters which lead to the thermal runaway.

In Fig. 4.8, the influence of varying fiber speeds on the process can be seen. The air temperature 150 °C , 200 °C , and 240 °C are chosen. With lower air temperatures and power levels, the fiber speed seems to have only a very small influence. With increasing power levels as well as air temperatures, the fiber speed influence gets visible. At slower speeds, the fiber gets warmer, as it has more time to pass through the microwave heating area and to develop the exothermic reaction. The exothermic reaction has thus also more time to add heat to the fiber.

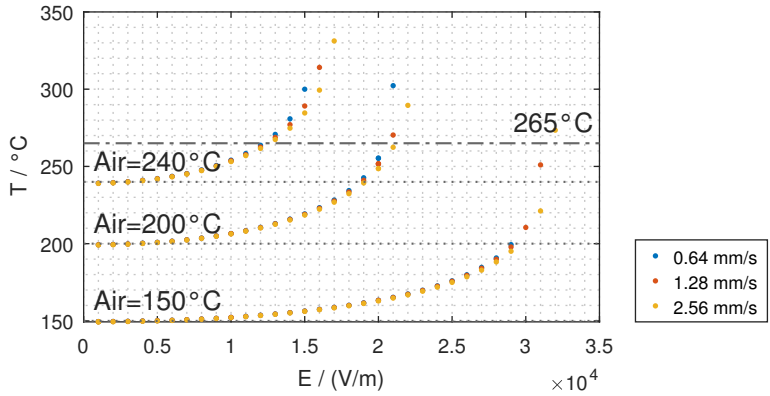

Figure 4.8: Simulated influence on fiber temperature at the cavity exit with varying fiber speeds, air temperatures and electrical field strengths.

The reaction kinetics model is included in the process model. This allows to calculate the fiber temperature including microwave heating. This establishes the opportunity to investigate the interaction between the microwaves and PAN fibers before starting any experiments. It gives first insights on the needed specifications for the devices used in the experimental setup. A study of the influences from the surrounding air temperature, the fiber speed and electrical field strength shows the small parameter combinations which lead to a stable process, see Chapter 4.3.

As conclusion the process parameters have to be controlled in the range of a few mm/s for the fiber speed, here 0.64 up to 2.56 mm/s, in order to get the desired temperature. Also one of the key elements is the temperature measurement for the air, as it can have a large impact on the fiber temperature changes and how close the operating point is to the instability. A hybrid process with air temperatures starting from 200 °C is beneficial to increase stability and reduce the thermal runaway range. The electrical field strength needs to be controlled within a few kV/m, depending on the air temperature and fiber speed, here in the range of 10 to 20 kv/m.
Future work on the model has different options. First, the full length of the heating and the quartz tube could be included in the model to also included the influence of any stabilization progress made before entering the cavity or after leaving it. Secondly, it could include an adaptation of the electrical

field in order to design a suitable applicator for a desired process, a more through study with e. g. multiple heating zones with different air temperatures and microwave powers or optimize heating profiles for minimal energy usage. Thirdly, it can also be an option to use the model in a model predictive control loop in an experiment. The influences of changes of process parameters could be calculated and then the parameters adapted accordingly.

4.4 Stabilization Degree

In the following part of the chapter, the different methods for the determination of the stabilization degree are discussed, as well as the changes that could improve the measurements.

4.4.1 FTIR Spectroscopy

Due to the obtained data, see Chapter 3.1.4, it is abstained from using FTIR as method to determine the stabilization degree further. In the future, the accuracy could be increased with a peak fitting analysis and ideally with industrially produced intermediate steps to avoid any influences of inaccurate temperature measurements on the fiber. This would also allow to calculate the stabilization degree for each of the three reactions. Comparison with literature is difficult as most of the times the exact chemical composition is unknown and different aspects are investigated. Also the definition of the stabilization degree may differ.

In [36] a fiber is passing multiple zones with a heating time per zone of three minutes. At a temperature of 240 °C and 12 min processing, the fiber has a cyclization index, equal to the stabilization degree with FTIR in this work, of roughly 50 %, and of 65 % at 260 °C. In [85] after 60 min processing at 230 °C, a cyclization index of roughly 70 % is obtained. The stabilization degrees for fibers processed in air in this work, see Fig. 3.14, lay in the range of 56 % up to 74 %. A direct comparison with literature values is thus not possible and individual measurements are necessary as well as calibrations for every new chemical composition. In future investigations it would be beneficial to define calibration standards for the research field.

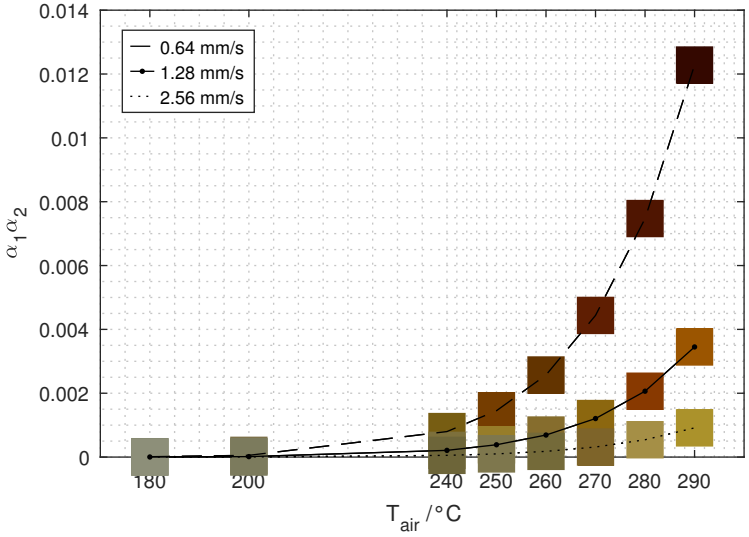

Figure 4.9: Color reference correlated with the stabilization degree $\alpha_1 \alpha_2$ for different air temperatures and fiber speeds.

4.4.2 Color Study

Based on the reference color graph, Fig. 3.18 and the process model, the reference is adapted to also include the stabilization degree $\alpha_1 \cdot \alpha_2$, depending on the color. In Fig. 4.9, color for different air temperatures and fiber speeds are displayed together with the corresponding stabilization degree. It can be seen that lower fiber speeds and higher temperatures lead also to higher stabilization degrees.

In a next step, the extracted temperatures of the experiment, presented in section 3.2.2 are examined in correlation to the process model results, thus the temperature and the stabilization degree. The temperature results of the simulation are shown in Fig. 4.10. The air temperature is displayed in blue and the quartz temperature in green. In the simulation the filament bundle is depicted as cylindrical fiber. However, the calculation is done for individual mesh cells along the length and radius of the effective fiber. This allows to give insights in the temperature distribution in the fiber and thus the filament

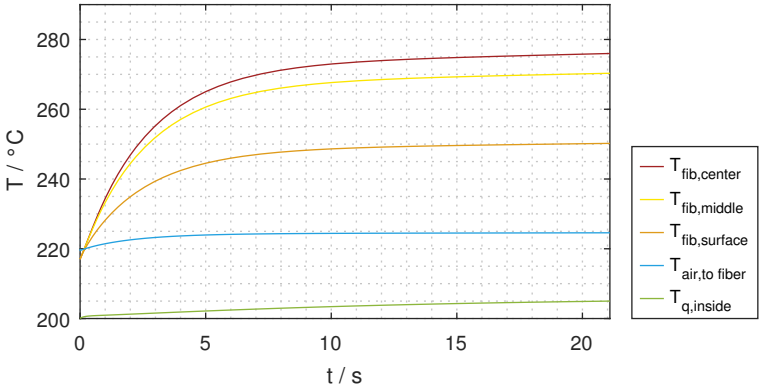

Figure 4.10: Simulation of fiber temperature evolution for an air temperature of 220 °C and a fiber speed of 2.56 mm/s.

bundle. For the fiber three different mesh cells are chosen, the most inner mesh cell, thus the center at around 275 °C, in red, a middle cell in between the center and the surface in yellow reaching 270 °C and the surface in orange with a temperature of 250 °C, see Fig. 4.10. Thus a difference between the fiber center and surface temperature of around 25 °C is occurring. The simulation allows also to calculate the stabilization degree of Fig. 4.10 and it drops from $8.59 \cdot 10^{-5}$ (red) to $6.28 \cdot 10^{-5}$ (yellow) to $1.96 \cdot 10^{-5}$ (orange). This shows that the stabilization degree inside the effective fiber is around 4 times higher than at the surface of the fiber. It can be assumed that it is similar for the filament bundle.
Compared to the results of the color study, to be seen in Fig. 3.19, the surface temperature of the experimental color study and the simulation are in agreement concerning the difference between inner and outer temperature of the fiber. The simulation is around 10 °C higher than in the color study at the center of the fiber, but the outer temperature is in both cases at 250 °C.

The same steps are done for the measurement results obtained with an air temperature of 220 °C and a speed of 1.28 mm/s, see Fig. 4.11. The color changes shown in the picture results from a forward power of around 18.6 W and an mean absorbed power in the system of around 5.5 W. The chosen points lead with the color study to temperatures of 250 °C, 280 °C and 280 °C. The simulated temperatures are around 280 °C in the center, and 250 °C at the

surface. So also for this case, the color study and the simulation are in good agreement. The results indicate an increase of 30 °C to 40 °C through the microwave heating with a stabilization degree that drops from $4.79 \cdot 10^{-4}$(red) to $3.39 \cdot 10^{-4}$ (yellow) to $9.51 \cdot 10^{-5}$ (orange), which is around 5 times lower than inside the fiber.

As can be seen from Fig. 3.19a and Fig. 4.11a, the radial transformation homogeneity is reduced by the microwave heating. This results in the need to optimize the process further, e. g. the use of a higher air temperature. If the microwave then still provides an advantage such as energy saving or a better chemical transformation thus structural integrity of the fibers has to be evaluated in future work.

As these findings of the color study in comparison with the simulated temperatures lead to a good agreement, it shows that hybrid microwave heating is possible. In future work, improvements to the temperature measurement could be done by using fiber Bragg sensors which can be used inside the fiber bundle inside the microwave cavity and thus get more accurate fiber temperatures. Also an upgrade could be made to the pictures by using a microscope to take the pictures. Nevertheless, the color study can be used as a first indication of the influence of the microwave heating on the temperature and thus the processing of the fiber.

4.5 Process Stability and Comparison to the Model

As the results in Fig. 3.20 show a large spread, the possible reasons are discussed in this section. Furthermore, the experimental results are compared to the modeled results.
In Fig 4.12, the experimentally obtained mean power (in blue) is compared with the absorbed power (in red) which was simulated with the presented process model. Different air temperatures are used, and fiber speed of 2.56 mm/s is applied. Multiple results of the absorbed power are due to different electrical field strengths in the simulation. The mean power of the experiment also includes the losses in the cavity wall and the quartz tube, whereas the absorbed power only comprises the power absorbed in the fiber. For the simulated results, only

(a) Choosing points by hand

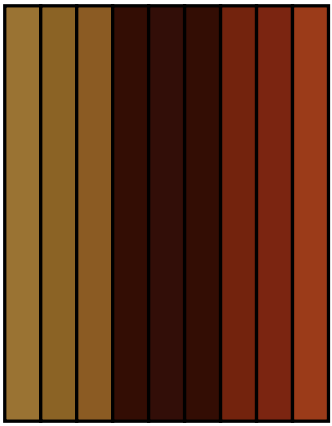

(b) Resulting color

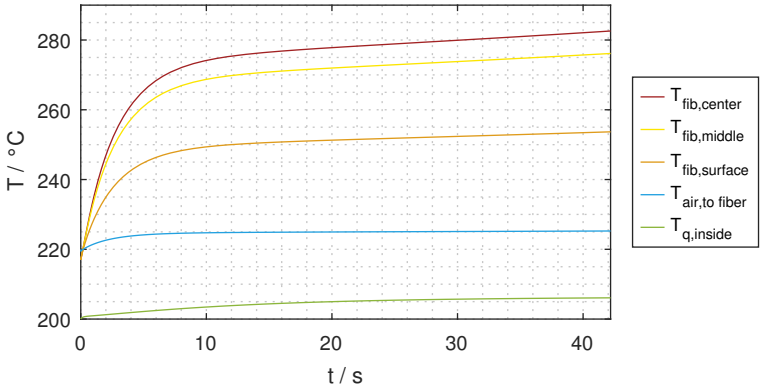

(c) Simulation of fiber temperature evolution for an air temperature of 220 °C and a fiber speed of 1.28 mm/s

Figure 4.11: Color study for an air temperature of 220 °C and a fiber speed of 1.28 mm/s a) choosing points b) extract color and compare to reference c) temperature simulation.

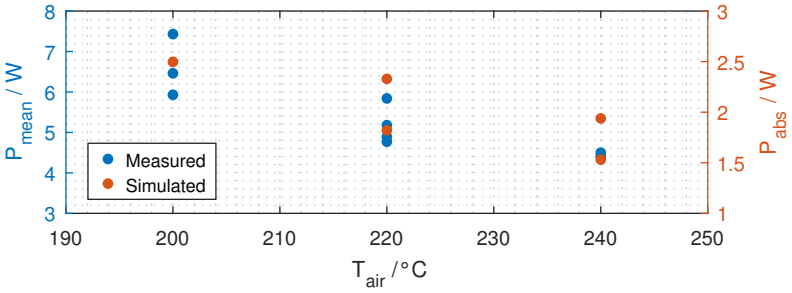

Figure 4.12: Comparison of the mean power level (blue) in the experiment and the absorbed power level from the simulation (red) for a fiber speed of 2.56 mm/s.

results with a temperature higher than 280 °C are chosen to mimic the burning of the fiber, that was seen in the experiment.
The course of both power levels is similar, see Fig 4.12. However, the overall level of both differ around 4 W. Although, a higher value of the experimental results is to be expected as they have have not been corrected by the wall losses, even with a correction of the mentioned 6 % the values between experiment and simulation still are not a match. It is possible that the wall losses are higher with higher temperatures of the cavity. This could be investigated in future work.

In order to find an explanation for the spreading in the results in Fig. 3.20, the following aspects are opportunities to reduce the spread:

- Pulsed power input
  As mentioned before, the amplification factor can be adapted by changing the voltage of the pre-amplifier. It was first set to 4.3 V for all measurements, resulting in a maximum power level of around 24.6 V. However, this lead to larger bandwidths to avoid burning the fiber. A reduction of the pre-amplifier voltage, results in a smaller amplification factor leading to a reduced peak power level. But in order to ensure the same mean power level, the bandwidth needs to be reduced. A diminished bandwidth ensures thus a more equal power input over time. This could lead to a more precises information on the mean power when the fiber breaks.

To test this, the pre-amplification is reduced to 1.5 V, leading to a maximum power level of around 10.5 V. A comparison of the experimental runs with both amplifications can be seen in Fig. 4.13. The changes made on the bandwidth, thus the frequency span around the resonance frequency, are shown, as well as its influence on the mean power. It is shown that with decreasing bandwidths the mean power level is increasing. However, for the larger amplification (4.3 V), the mean power level as more variations when the bandwidth is kept constant (in blue). The results show that for the lower amplification (in red), the mean power level has less fluctuation. This is a favorable indication, that a reduced amplification could have a positive effect on the spreading of the results. The study could thus be repeated with a smaller amplification factor.

- Difference in the air temperature
  As discussed previously, thermocouple placement has a big influence on the final air temperature, which then in turn influences the process. Thus the air temperature could be an influential factor for the spreading.

- System temperature
  In Fig. 4.14, a comparison is shown between different runs with the same process parameters, an air temperature of 200 °C, with a fiber speed of 1.28 mm/s, on different days.
  The cavity and the quartz tube temperature are seen on the right hand side. They have a slightly different time scale as the data is acquired through a second Matlab program. The experiment is started when the input temperature is at the desired process temperature. The quartz temperature of all runs are similar, but the cavity temperature of the first run is around 3 °C higher, than the second run and around 0.5 °C as the third, as the cavity temperature is not controlled in these experiments.
  Where the bandwidth, quality factor and frequency measurements abruptly end, the fiber is torn apart and left the resonator. For Run 1, this took place at a bandwidth of 10.5 MHz. During Run 2 the fiber broke at 12 MHz and for Run 3 at 10.2 MHz. The mean power at which the fiber broke is around 0.6 W higher between Run 1 and 2 and around 0.2 W higher between Run 3 and Run 1.
  As the temperatures of Run 1 and 3 are closer together and also the mean power levels at which the fibers tore, it is possible that the cavity tem-

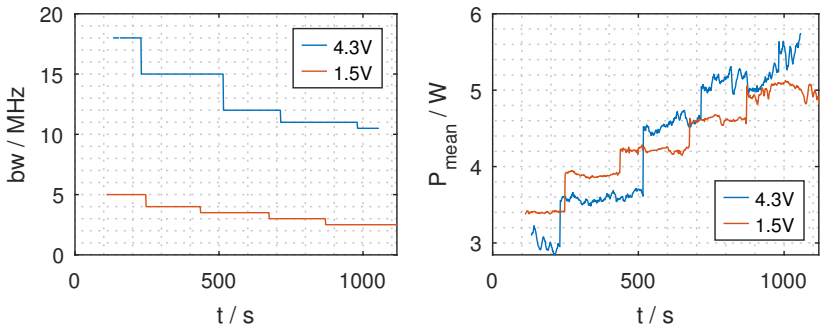

(a) Bandwidth changes

(b) Mean power level

Figure 4.13: Comparison between high (4.3 V) and low (1.5 V) amplification and otherwise the same parameters: air temperature of 200 °C, a fiber speed of 1.28 mm/s.

perature has an impact on the measurements and should be controlled as well in future experiments.

It is not possible to explain the spread only by one of the mentioned factors. It is probable though that multiple of them overlap. Next step to improve the measurements could include to repeat the measurements with the lower amplification factor or switch to a microwave power source, which can be operated at a single frequency instead of amplifying the network analyzer signal. Also, as mentioned before, a reproducible temperature measurement is needed. The cavity could be cooled again to stabilized the temperature and thus the resonance frequency of the system. Any frequency shifts are then only produced by changes in the dielectric constant of the fiber.

Next steps for the experiment could include a more detailed analysis of the actual needed power for the experiments. The lab scale experimental setup has the option to use both heating methods, conventionally and hybrid with microwaves. This allows to compare the energy needed for both methods on a lab scale level. However, it is of interest not only to know the power supplied to each of the equipment, but also to include, where possible, the knowledge on the efficiency and power losses e. g. as heat.

Further steps in the experimental investigations of the stabilization with microwaves could include to change to a Matlab control with a PID controller,

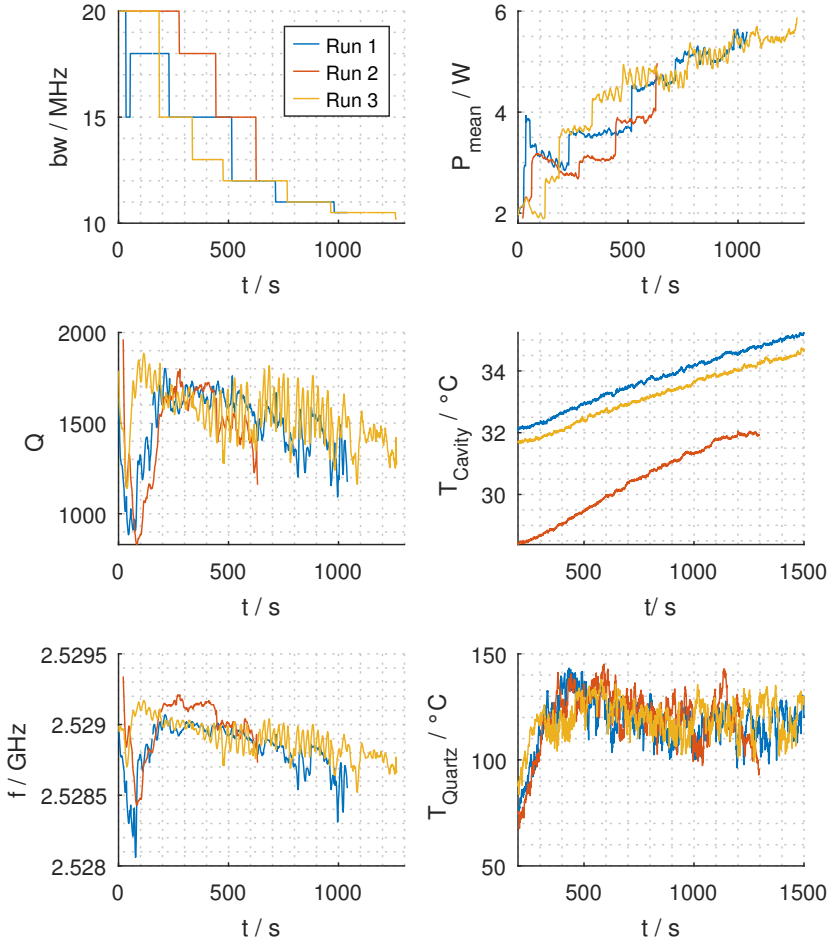

Figure 4.14: Comparison of the measurement data between different runs with the same process parameters (air temperature of 200 °C, a fiber speed of 1.28 mm/s) on different days.

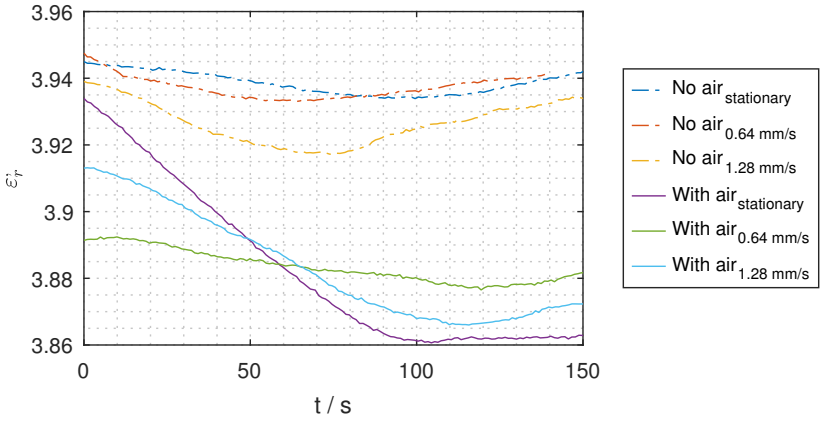

(a) Dielectric constant versus different speeds with and without air

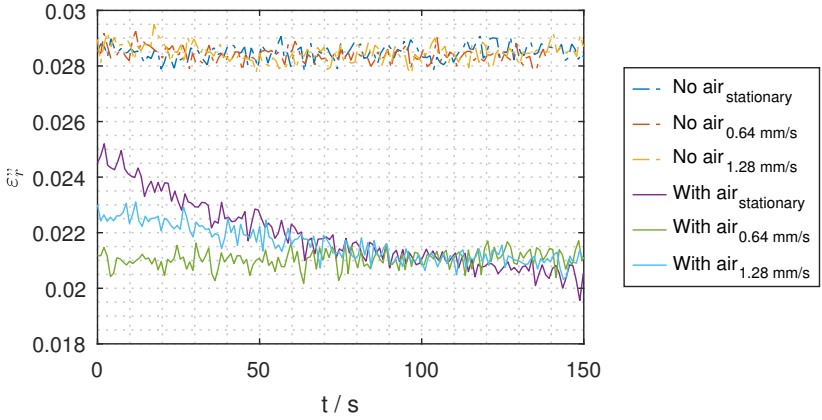

(b) Dielectric loss versus different speeds with and without air

Figure 4.15: Influence of fiber speed and air flow on the measurement of the dielectric properties.

leading to a fixed mean power level, at which the fiber is reaching a desired stabilization degree. Also the improvement of the radial homogeneity should be considered in future investigations.

5 Optimization of Waveguides for Microwave Stabilization

In the process model, a constant electrical field is applied to the fiber as the cavity in the experiment has also a constant field strength along the length. But as it is seen from the experiment e. g. from the color, the processing time of the cavity is too short to get a fully stabilized (black) fiber. For this reason, an extended cavity is desirable which can be used for the complete stabilization. A varying electrical field over the fiber length is needed to compensate the behavior of the dielectric loss. That can be achieved either by using multiple resonators of varying sizes and frequencies or by using one resonator with multiple steps of different geometric specifications. As individual resonators would also need multiple microwave sources, in a first step the approach to design one resonator with multiple steps is chosen. It allows a certain tunability too, as individual segments can be exchanged or added. For calculating and designing such a resonator different options are available, such as commercial available software such as CST Studio [51], μWave Wizard from Mician GmbH [86]. Alternatively, an in-house-developed simulation tool, using a simple approach such as the generalized scattering matrix method, can be used. The μWave Wizard software also uses as basis scattering matrix calculations, while CST Studio software is based on the Finite Integration Technique [87]. The advantages of the scattering matrix option is a faster computation time, as well as if setup in Matlab, there is the option to combine it in Matlab with the process model calculations. The implementation of a scattering matrix code for cylindrical waveguides has been done already at the IHM, called SMart Program [88]. It is chosen to use the code and extend it to be able to calculate the electrical field profile of cylindrical resonators [89]. Also the combination with an optimization algorithm is implemented. Combining the extended scattering matrix code with the process model, varying electrical field profiles depending on a desired temperature profile can be optimized [89].

In the first section of this chapter, the theory behind the scattering matrix code is explained shortly and the adaptation that is made to fulfill the desired criteria of using a cylindrical resonator are presented. It explains the setup of the generalized scattering matrix (GSM) code and the mode matching technique to calculate the resonance frequency and electrical field profile of arbitrary cylindrical resonators. In the second section, the setup for the optimization is given as well as simulation results.

5.1 Calculating an Electrical Field Profile with the GSM Code

The wave propagation can be described by the Helmholtz equations and can be derived from the Maxwell equations, which can be found in literature, e. g. in [59]. The Helmholtz equations are:

$$\vec{\nabla}^2\vec{H} + \omega^2\mu\varepsilon\vec{H} = 0 \tag{5.1a}$$

$$\vec{\nabla}^2\vec{E} + \omega^2\mu\varepsilon\vec{E} = 0, \tag{5.1b}$$

where $\vec{H}$ is the magnetic field, $\vec{E}$ the electric field, ω the angular frequency, μ the permeability, and ε the permittivity. From the wave equations, the axial and traversal field components can be obtained for the electrical and magnetic component. The calculations can be done for any coordinate system, such as rectangular or circular waveguides only by changing the coordinate system. Applying the boundary conditions as well as the separation of variables leads to the formulation of the transverse electric (TE) and the transverse magnetic (TM) waves. The field of a source field or inside a straight waveguide can be described by a superposition of its TE and TM eigenmodes. For the field of resonators, the irrotational modes have to be taken into account as well. In any case, the eigenmodes form the complete base of the field [59]. Each waveguide step can be specified by its own scattering matrix which is done in the generalized scattering matrix (GSM) approach [59, 88].
In the following, only cylindrical axially aligned waveguides are considered. Depending on the desired frequency range, radius and length, the dominant mode is the TM_{010} or the TE_{111}. The already used TM_{010} mode has the advantage that the electrical field strength is maximal in the center of the cavity.

This allows to tune the electrical field for the fiber easily with a combination of multiple cavities of different sizes. However, the approach stays the same for TE modes.

Scattering Matrix for Discontinuities

A waveguide with multiple discontinuities and waveguide segments of different geometrical properties can be approximated by multiple straight waveguides which are disrupted by the step discontinuities. Each segment and step cross section can be described by its own scattering matrix which then can be cascaded to describe the whole structure. At the mutual cross section of the discontinuities, the continuity of the transversal electrical and magnetic field needs to be applied.

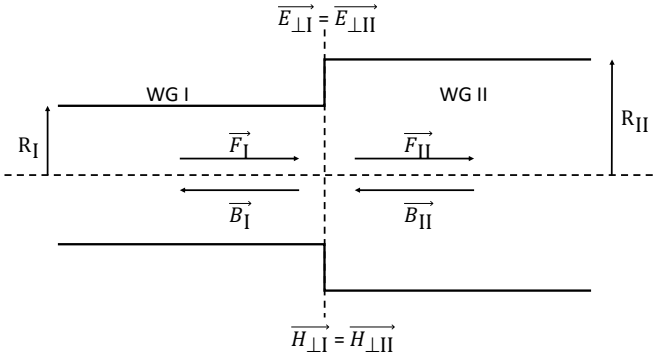

Figure 5.1: 2D cut of a step discontinuity of a waveguide [89].

Fig. 5.1 shows the discontinuity between two waveguide (WG) segments in a 2D cut which is rotational symmetrical, where R_I and R_{II} are the radii of the respective waveguide segments, F_I and F_{II} the forward traveling waves in the

segments and B_{I} and B_{II} the backwards traveling waves [89]. The scattering matrix for this example can be written as [90]:

$$\begin{pmatrix} B_{\mathrm{I}} \\ F_{\mathrm{II}} \end{pmatrix} = \begin{bmatrix} S_{11} & S_{12} \\ S_{21} & S_{22} \end{bmatrix} \begin{pmatrix} F_{\mathrm{I}} \\ B_{\mathrm{II}} \end{pmatrix}, \tag{5.2}$$

where S_{ij} is the relation between amplitudes of the incident a and transmitted or reflected b wave from the port j to i [55]:

$$S_{ij} = \left. \frac{b_i}{a_j} \right|_{a_k = 0 \text{ for } k \neq j}. \tag{5.3}$$

The scattering matrices of the straight waveguide segments have to include the modes according to the length and propagation constants. The scattering matrices of the discontinuity have to describe the coupling between all modes. Different geometric parameters lead to different modes that are above or below cut-off frequency in those segments. As higher-order eigenmodes, below cut-off, are attenuated, they can be neglected when combining the scattering matrices of two segments that are sufficiently far away from each other. For this reason, here, only a finite number of modes is included in the calculations. The mode matching technique can be used to calculate the coupling coefficients [90]. Through model expansion, the electric and magnetic fields in the circular waveguide WG I can be written as [90]:

$$\vec{E}_{\mathrm{I}} = \sum_{i=1}^{\infty} \left[F_{\mathrm{iI}} + B_{\mathrm{iI}} \right] \vec{e}_{\mathrm{iI}} \tag{5.4a}$$

$$\vec{H}_{\mathrm{I}} = \sum_{i=1}^{\infty} \left[\frac{F_{\mathrm{iI}} - B_{\mathrm{iI}}}{Z_{\mathrm{iI}}} \right] \vec{h}_{\mathrm{iI}}, \tag{5.4b}$$

where F_{iI} and B_{iI} contain the amplitude and phase of the forward and backward traveling waves, Z_{iI} is the wave impedance and $\vec{e}_{\mathrm{iI}}$ and $\vec{h}_{\mathrm{iI}}$ are the eigenmodes of the electric and magnetic fields of the i-th mode inside the waveguide I. Equally the field in the second waveguide WG II can be defined [90].
At the discontinuity, both waveguides share a common cross section. Their

tangential E and H fields have to fulfill the continuity law. The tangential electric field on the larger waveguide wall must vanish [90], resulting in:

$$[P][F_{\mathrm{I}} + B_{\mathrm{I}}] = [I][F_{\mathrm{II}} + B_{\mathrm{II}}] \tag{5.5a}$$

$$[Z_{\mathrm{I}}][P]^t[Y_{\mathrm{II}}][F_{\mathrm{II}} - B_{\mathrm{II}}] = [I][F_{\mathrm{I}} - B_{\mathrm{I}}], \tag{5.5b}$$

where the matrix $[P]$ contains the mode coupling coefficients, the diagonal matrix $[Z_{\mathrm{I}}]$ the wave impedances in the first waveguide and the diagonal matrix $[Y_{\mathrm{II}}]$ the wave admittances in the second waveguide [90]. The coupling coefficients are defined by the integral:

$$P_{ij} = \int_{s_{\mathrm{I}}} \vec{E}_{j,\perp,\mathrm{II}} \cdot \vec{E}^*_{i,\perp,\mathrm{I}} \mathrm{d}s_1, \tag{5.6}$$

with the tangential electric fields $\vec{E}_{j,\perp,\mathrm{I}}$ and $\vec{E}_{j,\perp,\mathrm{II}}$ in both waveguides. The individual calculation steps e. g. for the coupling coefficients for the different modes can be found in [59] and [88] for axially aligned cylindrical waveguides. From equations 5.5 and 5.2 the scattering parameters of a discontinuity can be written as [90]:

$$S_{11} = \left[[I] + [Z_{\mathrm{I}}][P]^t[Y_{\mathrm{II}}][P]\right]^{-1} \left[[I] - [Z_{\mathrm{I}}][P]^t[Y_{\mathrm{II}}][P]\right] \tag{5.7a}$$

$$S_{12} = 2\left[[I] + [Z_{\mathrm{I}}][P]^t[Y_{\mathrm{II}}][P]\right]^{-1} [Z_{\mathrm{I}}][P]^t[Y_{\mathrm{II}}] \tag{5.7b}$$

$$S_{21} = 2\left[[I] + [P][Z_{\mathrm{I}}][P]^t[Y_{\mathrm{II}}]\right]^{-1} [P] \tag{5.7c}$$

$$S_{22} = -\left[[I] + [P][Z_{\mathrm{I}}][P]^t[Y_{\mathrm{II}}]\right]^{-1} \left[[I] - [P][Z_{\mathrm{I}}][P]^t[Y_{\mathrm{II}}]\right]. \tag{5.7d}$$

Cascading Multiple Scattering Matrix

The next step is to cascade each scattering matrix from the center outwards, which is schematically represented in Fig. 5.2, where S^l is the left side scattering matrix and S^r the right one. The two scattering matrices are cascaded to a new one $\tilde{S}$, including the scattering parameters of the sub matrices S^l and S^r,

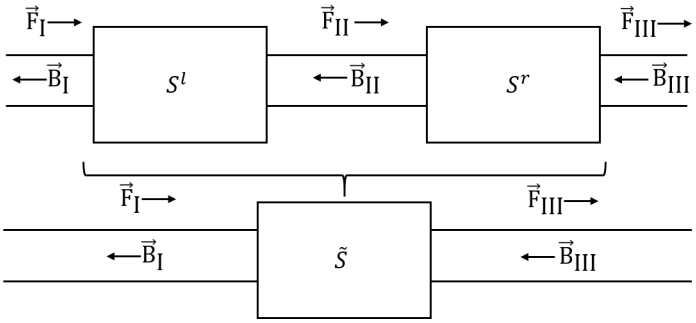

Figure 5.2: Cascading of scattering matrices.

where each matrix has the ports 1 and ports 2. The cascaded matrix can be calculated as follows [91]:

$$\tilde{S}_{11} = S^l_{12}\left([I] - S^r_{11}S^l_{22}\right)^{-1} S^r_{11}S^l_{21} + S^l_{11} \tag{5.8a}$$

$$\tilde{S}_{21} = S^r_{21}\left([I] - S^l_{22}S^r_{11}\right)^{-1} S^l_{21} \tag{5.8b}$$

$$\tilde{S}_{12} = S^l_{12}\left([I] - S^r_{11}S^l_{22}\right)^{-1} S^l_{21} \tag{5.8c}$$

$$\tilde{S}_{22} = S^r_{21}\left([I] - S^l_{22}S^r_{11}\right)^{-1} S^l_{22}S^r_{12} + S^r_{22}. \tag{5.8d}$$

A complete derivation can be found in [91]. This process is repeated as often as necessary, depending on the number of discontinuities.

Adapting the Scattering Matrix Code for Resonators

In the scope of this work, the existing scattering matrix code for circular waveguides [88] is extended to enable the calculation of cylindrical resonators with arbitrary geometrical parameters according to the steps presented by Neilson et al. [90]. For the calculations only a finite amount of modes is considered. As start values 20 TE and TM modes are chosen for the waveguide section with the smaller radius and 20·R1/R2 for the larger waveguide section. First the ends of the desired structure are terminated by a short. The respective

scattering matrix is added to scattering matrices of the first and last segment. Then the configuration of all segments is split in two parts which are cascaded into the single scattering matrices of the right S_{11}^R and left S_{11}^L side, resulting in:

$$B^R = S_{11}^R \cdot F^R \tag{5.9a}$$

$$B^L = S_{11}^L \cdot F^L. \tag{5.9b}$$

A resonance is obtained inside the cavity, when the forward and backward traveling waves at the split are equal. The eigenvalue equation can then be written as [90]:

$$B^R = S_{11}^R \cdot S_{11}^L \cdot B^R, \tag{5.10}$$

which leads to

$$\det(S_{11}^R \cdot S_{11}^L - \mathrm{I}) = 0. \tag{5.11}$$

Eq. 5.11 is the condition used to check if a frequency is resonant. The resonance frequency can be found through a loop over the desired frequency range for the lossless closed system. Only for the resonance frequency, the eq. 5.11 is solvable, thus true. After the resonance frequency is obtained, the amplitudes in all segments can be calculated by back-cascading from the eigenvector $\vec{B^R}$ with the help of eq. 5.5. The electric field profile can then be determined from the calculated amplitudes of all segments and the eq. 5.4a.

Comparison of the Scattering Code with CST Simulation

In Fig. 5.3, the normalized electrical field profile is compared between the SMart code and a simulation in CST. As geometrical properties a stepped resonator with 5 steps is chosen. The first and the last step have a radius of 6 mm and a length of 20 mm. The middle segments each have a length of 50 mm and decreasing radii from 50 mm to 40 mm to 30 mm. No coupling is used in the CST simulation.
The resonance frequency calculated by the extended SMart code [89] is 2.4277 GHz and of the CST simulation 2.4275 GHz. The difference in the resonance frequency is due to the discretization in the CST simulation, but a higher discretization leads also to longer simulation times. The current discretization lead to a simulation time in CST of 1 hour and 50 min where as the

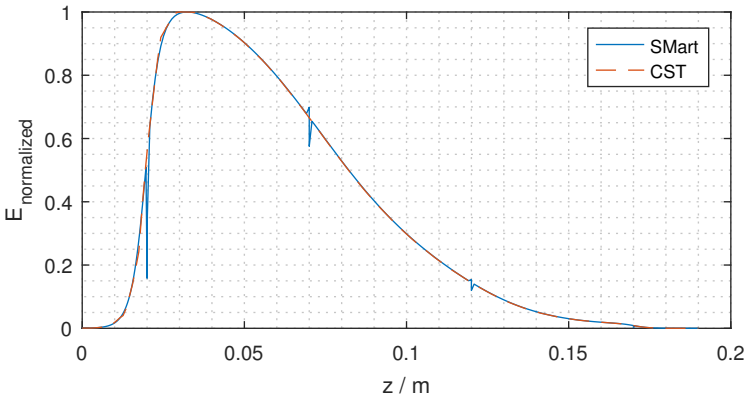

Figure 5.3: Comparison of normalized electrical profile obtained by the SMart code and CST simulation.

calculation with the SMart code took 12.8 s. The step peaks which can be seen in Fig. 5.3 from the SMart code occur only at the waveguide discontinuities. This is due to the applied assumption that strongly attenuated modes can be neglected in the waveguide. Even though they are attenuated in the waveguide, they are not yet attenuated at the step, which leads to those numerical errors. As the attenuation increases strongly with distance to the step, the error has only the local effect. It was decided to continue to setup an applicator optimization with the extended SMart code.

5.2 Workflow for the Optimization of an Applicator Design

In this section the general workflow is presented to understand how the program parts connect to each other. The extended scattering matrix code allows to calculate the electrical field profile for cylindrical segments with arbitrary geometric parameters. In combination with the process model, this allows to optimize applicators for different process parameters. The optimization uses fixed values for the size of the cavity and the number of segments that are designed as well as preset ranges for the geometry of the segments. This allows

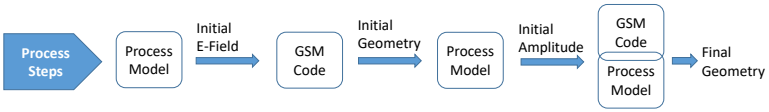

Model input parameters	Heatrate Goal fiber temperature Air temperature Fiber speed Processing time	Number of segments Geometry ranges for segments Frequency range	... + Electrical field profile	... + Amplitude estimation of the electrical field
Model output parameters	Temperature profile	Geometry for each segment frequency	Temperature profile	Temperature profile
Description	Adapt electrical field with 5 supporting points	Calculate geometry parameters to fit electrical field	Estimate amplitude for electrical field	
Optimization	Adapted manually	Global genetic algorithm	Estimated manually	Local algorithm for constrained nonlinear multivariable functions

Figure 5.4: Overview of the optimization steps.

to keep in mind the manufacturing process so that segments can be e. g. large or small enough for the available machinery or standard sizes of cylindrical pipes could be used to reduce the manufacturing effort.

In Fig. 5.4, the general workflow is described. In total there are four steps which will be explained on an example in more detail. At first, the desired temperature profile has to be defined, through heating rate, processing time. Together with a preset fiber speed, the length of the cavity and thus the processing time are preset in advance. Independent from the number of segments, five supporting points for the electrical field are scattered along the cavity length for the optimization. Two extra points are added at the entry and exit of the cavity with a reduced electrical field which represent the openings in the cavity wall through which the fiber enters and leaves the cavity. The first step is to adapt the level of the electrical field strength for each supporting point by hand to obtain a temperature profile close to the desired one. This simplifies to computational effort later on.

The temperature profile is divided in two parts for the optimization: heating up ramp and holding stage. This simplifies the identification of the starting values for the optimization and shortens the computing time, as the heating up

ramp and the holding stage need different electrical field profiles. Due to the hybrid heating, the dielectric loss has already increased, when the fiber enters the microwave assisted heating stage. Nevertheless, to heat the fiber up to the desired target temperature, a slight increase in the electrical field is needed. Also during the holding phase, the electrical field needs to compensate the drop in the dielectric loss with ongoing reaction.
As an example the workflow will be shown in more detail with the following parameters for the heating up ramp only. The temperatures and fiber speed are chosen based on the experimental results in Chapter 3. The number of segments and the cavity length are chosen at random.

- Heating rate: 30 °C/min
- Target fiber temperature: 260 °C
- Air temperature: 200 °C
- Fiber speed: 1.28 mm/s
- Number of segments: 8
- Cavity length: 25 cm

A TM_{010} mode is used in the calculations. Fig. 5.5a shows the electrical field of the chosen supporting points in blue and the interpolated electrical field in red over the length of the cavity. Next the modeled temperature profile is compared to the desired goal temperature profile, see Fig. 5.5b. It can be seen that it follows the general profile but the temperature is not quite as high as needed. In a first step this is sufficient, as the electrical field profile will be again optimized later and only starting values are needed. The temperature drop at the end is due to the reduced size and electrical field strength of the wall supporting point. Only the temperature profile is used for the optimization, the stabilization degree is not considered.

The second step is to calculate a geometry for the obtained electrical field profile with the help of the extended SMart Program. The genetic algorithm (ga) in Matlab [92] is used for the approximation of the geometry. The resulting geometry for the example, a 2D cut through the inside of the cavity, can be seen in Fig. 5.6a. Two waveguide sections seem rather small compared to the rest, this could be optimized in the future through reducing the number of steps and

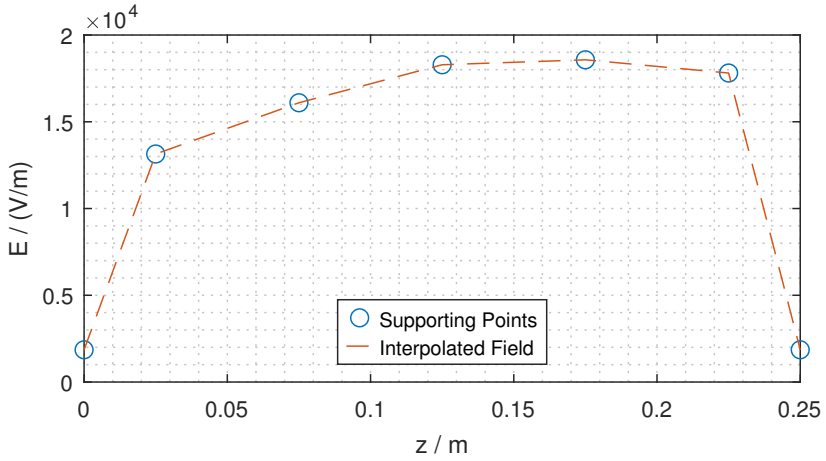

(a) Electrical field profile with supporting points.

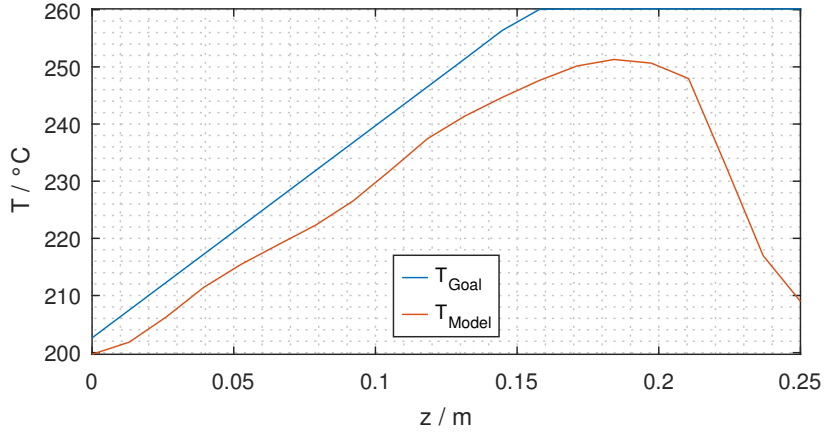

(b) Desired (red) and simulated (blue) temperature profile based on the electrical field profile

Figure 5.5: First step: setting supporting points by hand to approximate desired temperature profile.

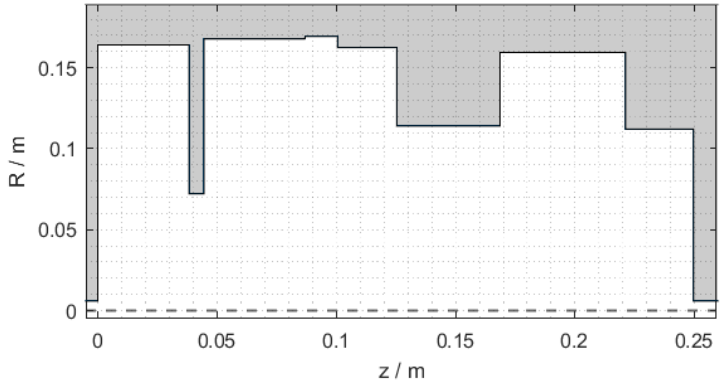

(a) Geometry based on supporting points

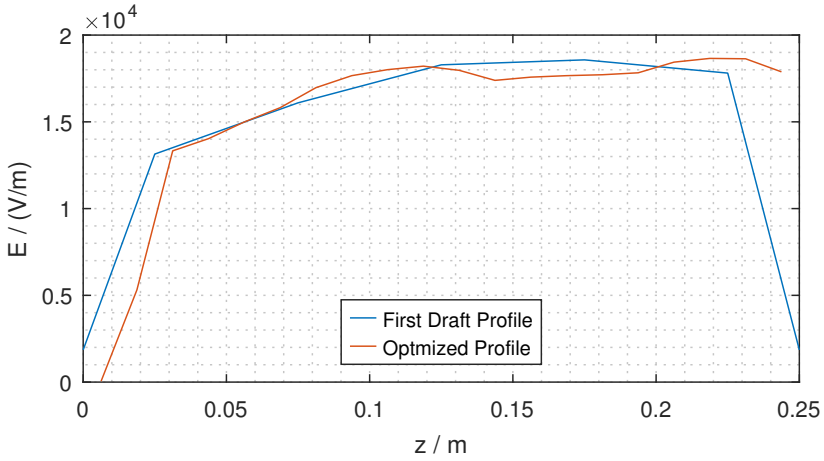

(b) Electrical field based on supporting points and calculated geometry

Figure 5.6: Second step: calculate a first geometry approximated from the supporting points from the first step.

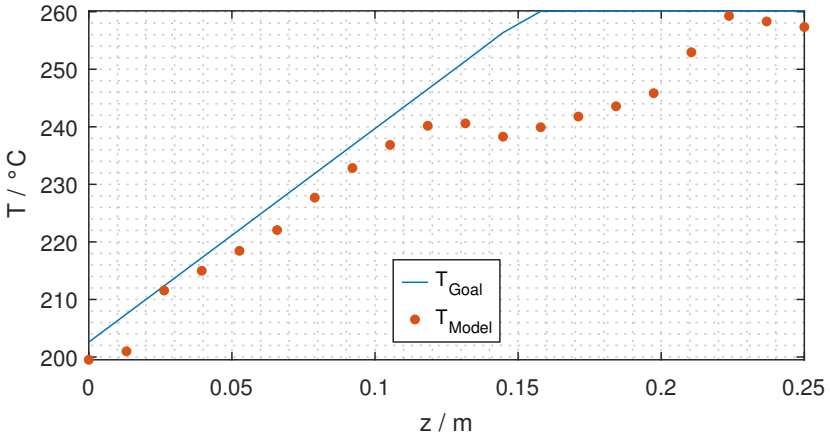

Figure 5.7: Third step: adjust the amplitude to bring simulation and desired profile closer together.

increasing the minimal size of a step. Fig. 5.6b shows the comparison between the interpolated electrical field (in blue) from the supporting points and the absolute electrical field of the empty resonator (in red). The slight variations between the draft profile and the profile based on the obtained geometry are tolerable, as in the final step the geometry is optimized again.

As the SMart Programm uses a normalized amplitude for calculations, the third step is to estimate a factor for the amplitude and run the process model with the guess. A reasonably close guess is enough, as the parameter will be also optimized in the final step. The calculated temperature profile has to be in the range of the desired profile, see Fig. 5.7.

At last the amplitude and the geometry are directly optimized together with the process model in the fourth step. A local algorithm, called „fmincon“ [83] in Matlab, is chosen to find the minimum. A comparison between the first draft geometry and the final result is shown in Fig. 5.8. A very small segment can be seen, which might not be easily manufactured. In a further optimization of the geometry a larger minimum segment size could be accounted for to improve producibility.
Fig. 5.9 shows the final temperature profile that is obtained through this optimization process which is a close fit. To summarize, the workflow is adapting supporting points by hand, obtaining a first geometry design with the extended

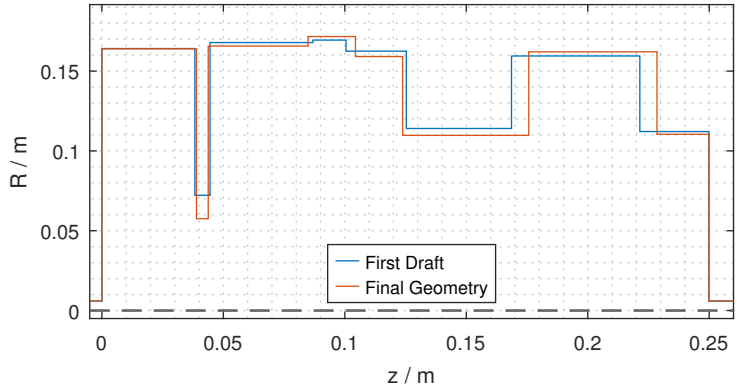

Figure 5.8: Comparison of first draft geometry and the final optimized geometry.

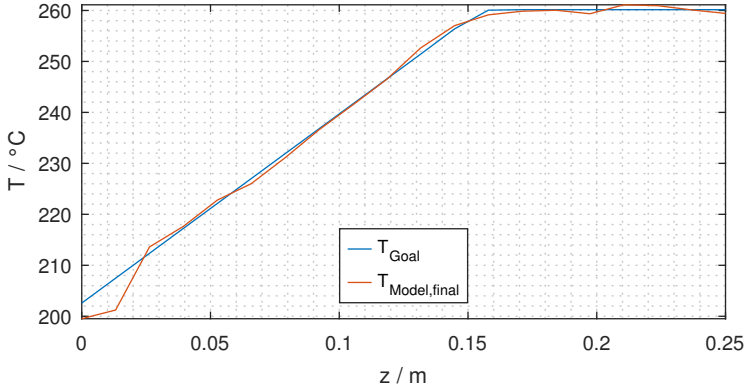

Figure 5.9: Fourth step: final optimization of the geometry and the amplitude inside the process model.

scattering matrix code, adjusting the amplitude and directly optimizing the electrical field profile together with the scattering matrix code. It is shown that a desired heating up ramp could be followed. The approach of designing multiple segments, allows for the consideration of the manufacturing as well as the tunability, as individual segments can be exchanged or added.

5.3 Applicator Designs for Different Parameters

In the following, the influence of different optimization parameters on the final design are shown. If not otherwise specified, the same parameters as listed above are chosen. In Fig. 5.10, different air temperatures are chosen for a total of six waveguide segments. Due to the preset heating rate of 30 °C/min the heating up time is increased with lower air temperatures. Nevertheless, it can be shown that a close following of the desired temperature profiles is achievable. Also the comparison between six, eight and ten segments in Fig. 5.11 shows a good agreement with the desired profile. As there are only minimal changes in temperature depending on the number of segments, it becomes clear that six segments are enough to satisfy the needed electrical field strength. The standard deviation for six segments is 2.2, for eight segments 1.87 and for ten segments 1.79. It is not possible to get a sufficient solution with four segments. The geometries are very different from each other and the resonance frequency varies in between 2.40 GHz and 2.48 GHz, see Fig. 5.12. It can be seen, that some segments are rather abrupt. This could be due to reasons such as not enough modes that are considered or no convergence acceleration was implemented. Also the allowed size of the segments could have been to small. Still, depending on the available possibilities for manufacturing, the desired resonance frequency and accuracy of the temperature profile different options are available through the optimization process.
Next steps can be to include the fiber speed, cavity length and the number of segments as variables in the optimization process. This could help to avoid unnecessary segments. A fixed variable would then be the duration of the stabilization in order to optimize an applicator for the full stabilization process. Also it could be of interest to include the optimization depending on the desired stabilization degree. Finally, next steps should include an experimental validation.

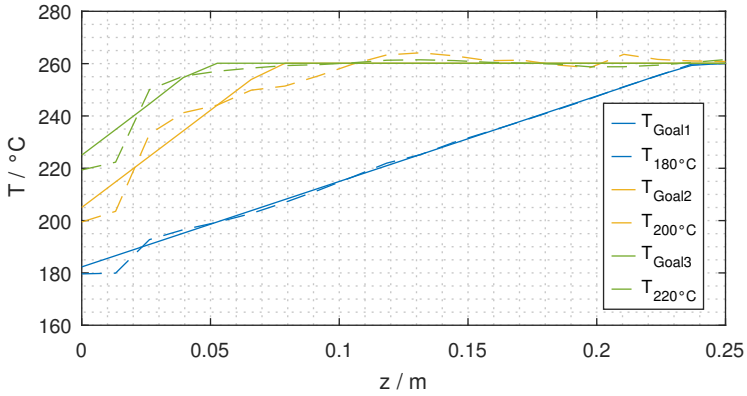

Figure 5.10: Comparison of resulting temperature profile for varying air temperatures with six segments.

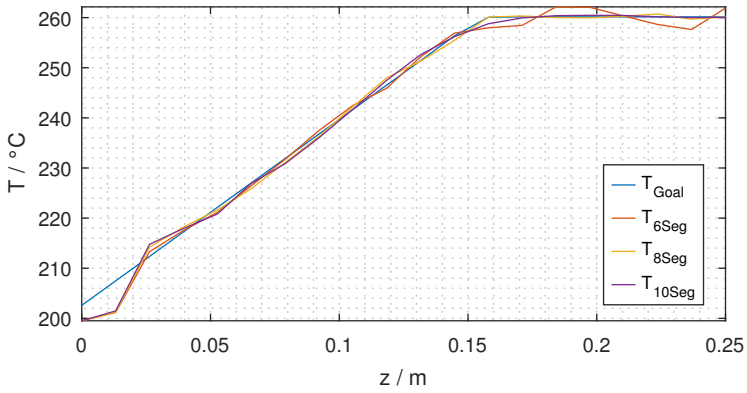

Figure 5.11: Comparison of resulting temperature profile for varying number of segments.

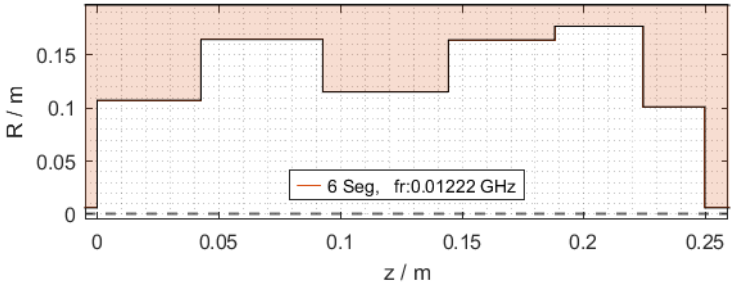

(a) Geometry based on six segments

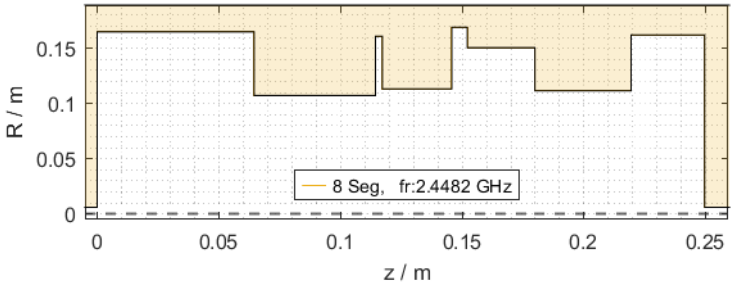

(b) Geometry based on eight segments

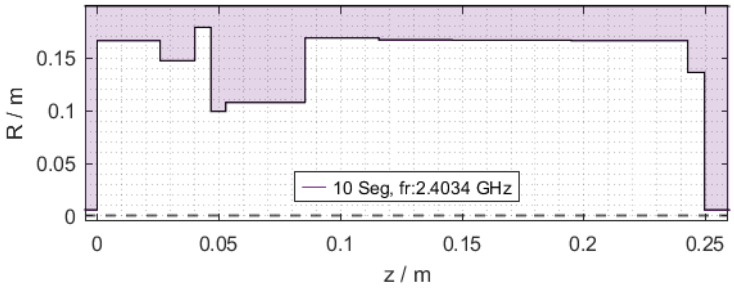

(c) Geometry based on ten segments

Figure 5.12: Comparison of resulting geometries for varying number of segments and their corresponding resonance frequency.

6 Conclusion and Outlook

The carbon fiber production and processing of carbon fibers is a wide field with different interdisciplinary aspects. The focus of this work is on the first production step, the stabilization stage, since the maximum energy saving potential is to be expected in this step. The stabilization requires the fiber to be heated up to 200-300 °C. To the knowledge of the author, today the fiber is only heated up conventionally or with plasma heating in production. In this work the first steps towards a microwave assisted stabilization of PAN fibers are discussed.

For the first time, full in-situ dielectric measurements are performed, providing the basis for understanding the challenges encountered when using dielectric heating. The results show a strong temperature dependency of the dielectric properties during heating and a decrease with ongoing chemical reaction as well as a decrease in temperature dependency when the fiber is processed. These findings have to be kept in mind for the design of a suitable applicator. Also, the measurements reveal the possibility to use dielectric properties as indicator for the stabilization degree.

In a second step, a first mathematical model which combines the reaction kinetics with the dielectric loss is proposed. A linear approach has been chosen to connect the dielectric properties to the degree of conversion. The degree of conversion is then combined to the reaction kinetic also with a linear approach. Although other definitions for the connection exist and different mixing rules are available, for the presented data the results are in good agreement with the linear approach.

Thirdly, for the first time a mathematical model which evaluates the temperature changes inside the fiber bundle and on the surface as a result of microwave heating as well as the heat transfer and exothermic heat, is set up. The reaction kinetics model is integrated in the multi-physics model of the stabilization. The model allows to calculate the development of the fiber temperature with regard

to the processing parameters. Investigating how the changes of the process parameters, such as fiber speed, air temperature and microwave power, affect the fiber temperature allowed to gather information on the process stability. Due to the influence of the dielectric loss and the exothermic reactions which add again more heat, a thermal runaway is very likely with certain parameter combinations. The model illustrates that only very few lead to the desired temperature range.

For a validation of the developed model, a prototype system is set up for a first test of stabilization with microwave heating. As the fiber temperature inside the cavity could not be measured, a color study is performed which helps to gain insights on the temperature raise and final stabilization degree that is caused by microwave heating. The results of the study compared to the model are in good agreement. However, the stability experiments show a rather large scattering of the results. Some reasons are discussed but for a full validation of the model the analysis needs to be repeated with an adapted setup.

In the experiments and the modeling, so far, a constant electrical field is used, but as the dielectric properties change with the ongoing reaction, this results in the need for changing electrical field strength during the process. For this reason, the multi-physics model is combined with an extended scattering matrix code. The unified code is able to calculated and optimize arbitrary electrical fields and applicator geometries for desired temperature profiles. This allows to design a suitable applicator for continuing experiments.

Outlook

These initial steps towards a stabilization with microwave heating show also that some improvements could be considered for future investigations. Those shall be summarized in the following.

Temperature measurements The temperature measurement is quite essential for collecting the best data. In this work a thermocouple is used which is placed by hand. This could already be improved by melting the thermocouple through the quartz so that only the tip is inside the tube. But not only the air temperature is of interest and needs to be reproducible and precise, but also the fiber temperature is of interest. The usage of infrared cameras or pyrometers

is difficult when working with microwaves and quartz tubes in a low temperature range. Although it is possible to drill a hole in the cavity wall and the quartz tube to see directly onto the fiber, this might lead to disturbances for the electrical field and temperature profile. In an applicator with varying electrical field strength, a hole in a section with lower field strength might be possible. Another option might be the usage of fiber Bragg sensors.

Dielectric properties for quality control Although it is shown in this work, that dielectric properties have the ability to reflect the degree of stabilization, a calibration is needed for every chemical composition. For the calibration, the usage of other methods such as the FTIR or DSC should not be disregarded, especially as the evaluation of the FTIR results can be improved with peak fitting methods. It could also be of interest to see if other mixing rules or approaches to the connection between stabilization degree and reaction kinetics are more useful. And at last it should be considered if all three reactions need be included in the model when a calibration for industrial purposes is made.

Fiber shrinkage and fiber tension The fiber tension is mentioned as important factor for the final stabilization grade. A more thorough analysis might be of interest as with higher fiber tensions the fiber shrinkage will decrease and this will have an effect on the permittivity, the density and the fiber diameter.

Up-scaling, building a suitable applicator In this work, only a short applicator is used which could not cover the needed process time. Up-scaling the applicator to the required process time will lead to a more spacious applicator, here the filament guiding system should be kept in mind to ensure a constant fiber tension over the length.

A Appendix

A.1 Derivation of eq. 2.26 and eq. 2.27

From Fig. 2.12 it can be seen that the powers measured with the power meter P2 and P3 respectively, can be calculated as:

$$P_2 = P_1 \cdot S_{21}^2 + P_{\text{refl}} \cdot S_{42}^2, \tag{A.1a}$$

$$P_3 = P_1 \cdot S_{31}^2 + P_{\text{refl}} \cdot S_{43}^2. \tag{A.1b}$$

After solving eq. A.1a for P_1, it can be inserted in eq. A.1b and solved for P_{refl}:

$$P_1 = \frac{P_2 - P_{\text{refl}} \cdot S_{42}^2}{S_{21}^2}$$

$$P_3 = \frac{P_2 - P_{\text{refl}} \cdot S_{42}^2}{S_{21}^2} \cdot S_{31}^2 + P_{\text{refl}} \cdot S_{43}^2$$

$$P_3 \cdot S_{21}^2 = P_2 \cdot S_{31}^2 - P_{\text{refl}} \cdot S_{42}^2 \cdot S_{31}^2 + P_{\text{refl}} \cdot S_{43}^2 \cdot S_{21}^2$$

$$P_{\text{refl}} = \frac{P_3 \cdot S_{21}^2 - P_2 \cdot S_{31}^2}{S_{43}^2 \cdot S_{21}^2 - S_{42}^2 \cdot S_{31}^2} \tag{A.2}$$

The incoming power at port 4 can be calculated as:

$$P_{\text{inc}} = P_1 \cdot S_{41}^2. \tag{A.3}$$

Solving for P_1 allows to insert in eq. A.1a and solve for P_{inc}:

$$
\begin{aligned}
P_1 &= \frac{P_{\text{inc}}}{S_{41}^2} \\
P_2 &= \frac{P_{\text{inc}}}{S_{41}^2} \cdot S_{21}^2 + P_{\text{refl}} \cdot S_{42}^2 \\
P_2 \cdot S_{41}^2 &= P_{\text{inc}} \cdot S_{21}^2 + P_{\text{refl}} \cdot S_{42}^2 \cdot S_{41}^2 \\
P_{\text{inc}} &= \left(P_2 - P_{\text{refl}} \cdot S_{42}^2 \right) \frac{S_{41}^2}{S_{21}^2} \qquad \text{(A.4)}
\end{aligned}
$$

Bibliography

[1] T. Ellringmann, C. Wilms, M. Warnecke, G. Seide, and T. Gries, "Carbon fiber production costing: a modular approach," *Textile Research Journal*, vol. 86, no. 2, pp. 178–190, 2016. [Online]. Available: https://doi.org/10.1177/0040517514532161

[2] Dragon Plate, "Carbon fiber vs aluminum," 2021-10-21. [Online]. Available: https://dragonplate.com/carbon-fiber-vs-aluminum/

[3] P. Morgan, *Carbon fibers and their composites*. CRC press, 2005.

[4] F. L. Paulauskas, C. D. Warren, and C. C. Eberle, "Novel precursor materials and approaches for producing lower cost carbon fiber for high volume industries," *17. ICCM Conference*, 2009.

[5] S.-J. Park, *Carbon fibers*. Dordecht: Springer, 2015.

[6] Zoltek, "Sporting goods applications," 2022-02-03. [Online]. Available: https://zoltek.com/applications/sporting-goods/

[7] H. Eickenbusch and O. Krauss, "Kurzanalyse Nr.3: Kohlenstofffaserverstärkte Kunststoffe im Fahrzeugbau," *Zentrum Ressourceneffizienz*, 2013. [Online]. Available: https://www.ressource-deutschland.de/service/publikationen/detailseite/ka-3-kohlenstofffaserverstaerkte-kunststoffe-fahrzeugbau/

[8] H. Liddell, C. Dollinger, A. Fisher, S. Brueske, A. Carpenter, and J. Cresko, "Bandwidth study on energy use and potential energy saving opportunities in u.s. carbon fiber reinforced polymer manufacturing," 2017.

[9] S. Rana and R. Fangueiro, Eds., *Fibrous and Textile Materials for Composite Applications*, 1st ed., ser. Textile Science and Clothing Technology. Singapore: Springer Singapore, May 2016, doi:10.1007/978-981-10-0234-2.

[10] M. Heine, "(De) Optimierung der Reaktionsbedingungen von thermoplastischen Polymerfasern zur Kohlenstoffaser-Herstellung am Beispiel

von Polyacrylnitril," Doctoral thesis, 1989, Technische Universität Karlsruhe, Falk-Verlag Ötigheim.

[11] S. Carbon, "PANOX Oxidierte PAN-Fasern," 2021-11-30. [Online]. Available: https://www.sglcarbon.com/loesungen/material/sigrafil-carbon-endlosfasern/

[12] E. Fitzer, A. Foley, W. Frohs, T. Hauke, M. Heine, H. Jäger, and S. Sitter, *Fibers, 15. Carbon Fibers*. American Cancer Society, 2012, doi:10.1002/14356007.o11-o04.

[13] D. Sunter, W. Morrow, III, J. Cresko, and H. Liddell, "The manufacturing energy intensity of carbon fiber reinforced polymer composites and its effect on life cycle energy use for vehicle door lightweighting," *20th International Conference on Composite Materials*, 2015.

[14] R. Fruehan, O. Fortini, H. Paxton, and R. Brindle, "Theoretical minimum energies to produce steel for selected conditions," *Technical Report*, 2000.

[15] S. Horikoshi, R. Schiffmann, J. Fukushima, and N. Serpone, *Microwave Chemical and Materials Processing: A Tutorial*, 01 2018, doi:10.1007/978-981-10-6466-1.

[16] H. Khayyam, M. Naebe, O. Zabihi, R. Zamani, S. Atkiss, and B. Fox, "Dynamic prediction models and optimization of polyacrylonitrile (pan) stabilization processes for production of carbon fiber," *IEEE Transactions on Industrial Informatics*, vol. 11, pp. 887–896, 2015.

[17] K. Badii, G. Golkarnarenji, A. S. Milani, M. Naebe, and H. Khayyam, "A comprehensive chemical model for the preliminary steps of the thermal stabilization process in a carbon fibre manufacturing line," *React. Chem. Eng.*, vol. 3, pp. 959–971, 2018, doi:10.1039/C8RE00164B.

[18] J. Gandert, "Model set up for the stabilization of pan fibers - implementation of the reaction kinetics and analysis of heat input and heat transfer," Master thesis, Karlsruhe Insitute of Technology (KIT), 2020.

[19] E. Keszei, *Reaction Kinetics*. Springer Nature Switzerland AG, 2021, doi:10.1007/978-3-030-68574-4.

[20] O. Levenspiel, *Chemical Reaction Engineering*. Wiley, 1999.

[21] G. Emig and E. Klemm, *Chemische Reaktionstechnik*, ser. Springer-Lehrbuch. Springer-Verlag GmbH Deutschland, 2017.

[22] J. Liu, S. Xiao, Z. Shen, L. Xu, L. Zhang, and J. Peng, "Study on the oxidative stabilization of polyacrylonitrile fibers by microwave heating," *Polymer Degradation and Stability*, vol. 150, pp. 86–91, 02 2018, doi:10.1016/j.polymdegradstab.2018.02.017.

[23] F. L. Paulauskas, T. S. Bigelow, and T. T. Meek, "Diagnostic monitor for carbon fiber processing," Patent, US6375875B1, 2002.

[24] A. A. Kharitonov, "Technique of high-strengh and high-modulus carbon riber receiving," Patent, RU2343235C1, 2009.

[25] B. Wohlmann, M. Woelki, C. Hunyar, and et al., "Stabilization of polyacrylonitrile precursor yarn," Patent, EP2475812 B1, 2012.

[26] F. L. Paulauskas, T. L. White, and D. M. Sherman, "Apparatus and method for oxidation and stabilization of polymeric materials," Patent, US7534854B1, 2009.

[27] F. L. Paulauskas, T. L. White, and D. M. Sherman, "Apparatus and method for oxidation and stabilization of polymeric materials," Patent, US7786253B2, 2010.

[28] F. L. Paulauskas, A. K. Naskar, and T. A. Bonds, "Advanced oxidation method for producing high-density oxidized polyacrylonitrile fibers," Patent, US20150252501A1, 2015.

[29] V. Shmyrev, "Method for stabilizing a carbon-containing fibre and method ofr producing a carbon fibre," Patent, EP2460915B1, 2014.

[30] F. L. Paulauskas and T. L. White, "Temperature-dependent dielectric measurements of polyacrylonitrile fibers during air oxidation," in *International SAMPE Symposium and Exhibition, Long Beach, California*, vol. 16. Citeseer, May 2004.

[31] F. L. Paulauskas, C. D. Warren, and J. A. Carpenter, "Oxidative stabilization of pan fiber precursor," *Automotive Lightweighting Materials, FY 2004 Progress Report*, 2004.

[32] S. W. Lee, H. Y. Lee, S. Y. Jang, S. M. Jo, H. S. Lee, and S. H. Lee, "Tensile properties and morphology of carbon fibers stabilized by plasma treatment," *Carbon letters*, vol. 12, pp. 16–20, 03 2011, doi:10.5714/CL.2011.12.1.016.

[33] S. W. Lee, H. Y. Lee, S. Y. Jang, S. Jo, H. S. Lee, W. H. Choe, and S. Lee, "Efficient preparation of carbon fibers using plasma assisted stabilization," *Carbon*, vol. 55, pp. 361

– 365, 2013, doi:10.1016/j.carbon.2012.10.062. [Online]. Available: http://www.sciencedirect.com/science/article/pii/S0008622312008755

[34] C. Zhang, J. Liu, S. Guo, S. Xiao, Z. Shen, and L. Xu, "Comparison of microwave and conventional heating methods for oxidative stabilization of polyacrylonitrile fibers at different holding time and heating rate," *Ceramics International*, vol. 44, no. 12, pp. 14 377 – 14 385, 2018, doi:10.1016/j.ceramint.2018.05.047. [Online]. Available: http://www.sciencedirect.com/science/article/pii/S0272884218311799

[35] S. Soulis, G. Konstantopoulos, E. P. Koumoulos, and C. A. Charitidis, "Impact of alternative stabilization strategies for the production of pan-based carbon fibers with high performance," *Fibers*, vol. 8, no. 6, 2020, doi:10.3390/fib8060033. [Online]. Available: https://www.mdpi.com/2079-6439/8/6/33

[36] G. Zhao, J. Liu, L. Xu, and S. Guo, "Study on structure evolution and reaction mechanism in microwave pre-oxidation," *Journal of Inorganic and Organometallic Polymers and Materials*, pp. 1–10, 2021.

[37] H.-W. Chao, H.-C. Hsu, Y.-R. Chen, and T.-H. Chang, "Characterizing the dielectric properties of carbon fiber at different processing stages," *Scientific Reports*, vol. 11, no. 1, pp. 1–7, 2021.

[38] M. Dunham and D. Edie, "Model of stabilization for pan-based carbon fiber precursor bundles," *Carbon*, vol. 30, no. 3, pp. 435–450, 1992.

[39] S. Das, A. Mukhopadhyay, S. Datta, and D. Basu, "Prospects of microwave processing: An overview," *Bulletin of Materials Science*, vol. 32, pp. 1–13, 12 2009, doi:10.1007/s12034-009-0001-4.

[40] H. Khayyam, R. N. Jazar, S. Nunna, G. Golkarnarenji, K. Badii, S. M. Fakhrhoseini, S. Kumar, and M. Naebe, "Pan precursor fabrication, applications and thermal stabilization process in carbon fiber production: experimental and mathematical modelling," *Progress in Materials Science*, vol. 107, p. 100575, 2020.

[41] B. M. Terra, D. A. de Andrade, and R. N. de Mesquita, "Characterization of polyacrylonitrile thermal stabilization process for carbon fiber production using intelligent algorithms," *Polymer Testing*, vol. 100, p. 107238, 2021.

[42] M.-J. Yu, Y.-J. Bai, C.-G. Wang, Y. Xu, and P.-Z. Guo, "A new method for the evaluation of stabilization index of polyacrylonitrile fibers," *Materials Letters*, vol. 61, no. 11-12, pp. 2292–2294, 2007.

[43] Y. Xue, J. Liu, and J. Liang, "Correlative study of critical reactions in polyacrylonitrile based carbon fiber precursors during thermal oxidative stabilization," *Polymer Degradation and Stability*, vol. 98, pp. 219–229, 01 2013, doi:10.1016/j.polymdegradstab.2012.10.018.

[44] W. Dang, J. Liu, X. Wang, K. Yan, A. Zhang, J. Yang, L. Chen, and J. Liang, "Structural transformation of polyacrylonitrile (pan) fibers during rapid thermal pretreatment in nitrogen atmosphere," *Polymers*, vol. 12, no. 1, 2020, doi:10.3390/polym12010063. [Online]. Available: https://www.mdpi.com/2073-4360/12/1/63

[45] H. Wei, X. Suo, C. Lu, and Y. Liu, "A comparison of coagulation and gelation on the structures and stabilization behaviors of polyacrylonitrile fibers," *Journal of Applied Polymer Science*, vol. 137, 11 2019, doi:10.1002/app.48671.

[46] S. B. Warner, L. Peebles, and D. R. Uhlmann, "Oxidative stabilization of acrylic fibres," *Material Science*, vol. 14, pp. 556–564, 1997, doi:10.1007/BF00772714.

[47] A. Gupta and I. Harrison, "New aspects in the oxidative stabilization of pan-based carbon fibers," *Carbon*, vol. 34, no. 11, pp. 1427–1445, 1996, doi:10.1016/S0008-6223(96)00094-2.

[48] D. Edie, "The effect of processing on the structure and properties of carbon fibers," *Carbon*, vol. 36, no. 4, pp. 345–362, 1998, doi:10.1016/S0008-6223(97)00185-1.

[49] E. Fitzer, W. Frohs, and M. Heine, "Optimization of stabilization and carbonization treatment of pan fibres and structural characterization of the resulting carbon fibres," *Carbon*, vol. 24, pp. 387–395, 01 1986, doi:10.1016/0008-6223(86)90257-5.

[50] S. Soulis, D. A. Dragatogiannis, G. Konstantopoulos, and C. Charitidis, "Application of pan fiber length change as the oxidative stabilization process control parameter," *Materials Today: Proceedings*, vol. 5, no. 14, Part 1, pp. 27 645–27 652, 2018, 11th Panhellenic Scientific Conference on Chemical Engineering, 25-27 May 2017.

[51] Dassault Systems, "Cst studio suite 2018," 2021-11-30. [Online]. Available: https://www.3ds.com/de/produkte-und-services/simulia/produkte/cst-studio-suite/

[52] Verein deutscher Ingenieure, *VDI-Wärmeatlas*, 11th ed., VDI e.V., Ed. Berlin Heidelberg: Springer, 2013, doi:10.1007/978-3-642-19981-3.

[53] M. Mehdizadeh, “Chapter 1 - the impact of fields on materials at microwave and radio frequencies,” in *Microwave/RF Applicators and Probes (Second Edition)*, second edition ed., M. Mehdizadeh, Ed. Boston: William Andrew Publishing, 2015, pp. 1–33, doi:10.1016/B978-0-323-32256-0.00001-4. [Online]. Available: https://www.sciencedirect.com/science/article/pii/B9780323322560000014

[54] T. Matsushita, *Electricity and Magnetism: New Formulation by Introduction of Superconductivity*, 01 2021, doi:10.1007/978-3-030-82150-0.

[55] D. M. Pozar, *Microwave engineering; 4th ed.* John Wiley & Sons, 2012.

[56] L.-F. Chen, C. Ong, C. Neo, V. Varadan, and V. K. Varadan, *Microwave electronics: measurement and materials characterization*. John Wiley & Sons, 2004.

[57] H. Schiefer and F. Schiefer, *Statistics for Engineers*. Springer Wiesbaden, 2021, doi:10.1007/978-3-658-32397-4.

[58] Joint Committee for Guides in Metrology (JCGM), “Evaluation of measurement data —guide to the expression of uncertainty in measurement,” 2008.

[59] R. Collin, *Foundations for Microwave Engineering*. McGraw Hill Book, Singapore, 1966.

[60] S. Vyazovkin, A. K. Burnham, J. M. Criado, L. A. Perez-Maqueda, C. Popescu, and N. Sbirrazzuoli, “Ictac kinetics committee recommendations for performing kinetic computations on thermal analysis data,” *Thermochimica Acta*, vol. 520, no. 1, pp. 1–19, 2011, doi:10.1016/j.tca.2011.03.034.

[61] H. Baehr and K. Stephan, *Wärme- und Stoffübertragung*. Springer Berlin Heidelberg, 2010, doi:10.1007/978-3-642-10194-6.

[62] Sartorius Lab Instruments GmbH, “Laboratory balance,” 2023-05-21. [Online]. Available: https://www.sartorius.com/en/products/weighing/laboratory-balances

[63] Sartorius Lab Instruments GmbH , “Weighing application compendium - density determination,” 2023-05-21. [Online]. Available: https://www.sartorius.com/en/products/weighing/lab-weighing-resources/weighing-application-compendium-density-determination

[64] S. K. Sharma, Ed., *Handbook of Materials Characterization*. Springer Cham, 2018, doi:10.1007/978-3-319-92955-2.

[65] G. Konstantopoulos, S. Soulis, D. Dragatogiannis, and C. Charitidis, “Introduction of a methodology to enhance the stabilization process of pan fibers by modeling and advanced characterization,” *Materials*, vol. 13, p. 2749, 06 2020, doi:10.3390/ma13122749.

[66] S. Dalton, F. Heatley, and P. M. Budd, “Thermal stabilization of polyacrylonitrile fibres,” *Polymer*, vol. 40, no. 20, pp. 5531–5543, 1999, doi:10.1016/S0032-3861(98)00778-2.

[67] J. Hofele, G. Link, and J. Jelonnek, “Reaction kinetics and process model of the polyacrylonitrile fibers stabilization process based on dielectric measurements,” *Materials*, vol. 15, no. 3, 2022, doi:10.3390/ma15031222. [Online]. Available: https://www.mdpi.com/1996-1944/15/3/1222

[68] Thermocoupleinfo, “Thermocouple accuracies,” 2021-11-30. [Online]. Available: https://www.thermocoupleinfo.com/thermocouple-accuracies.htm

[69] Heraeus Holding, “Properties of fused silica,” 2023-05-21. [Online]. Available: https://www.heraeus.com/en/hca/fused_silica_quartz_knowledge_base_1/properties_1/properties_hca.html#tabs-608478-8

[70] J.-H. Park and J.-G. Park, “Uncertainty analysis of q-factor measurement in cavity resonator method by electromagnetic simulation,” *SN Applied Sciences*, vol. 2, 2020. [Online]. Available: https://doi.org/10.1007/s42452-020-2819-8

[71] Polymerdatabase, “Poly(acrylonitrile),” 2023-02-17. [Online]. Available: https://polymerdatabase.com/polymers/polyacrylonitrile.html

[72] T. E. Toolbox, “Thermal expansion - linear expansion coefficients,” 2023-03-01. [Online]. Available: https://www.engineeringtoolbox.com/linear-expansion-coefficients-d_95.html

[73] Anritsu, “Anristsu power measrument uncertainty calculator,” 2023-03-01. [Online]. Available: https://www.anritsu.com/en-US/test-measurement/support/downloads/software/dwl003263

[74] Comsol, “Comsol multiphysics,” 2021-06-30. [Online]. Available: https://www.comsol.de/

[75] F. Moukalled, L. Mangani, and M. Darwish, *The Finite Volume Method in Computational Fluid Dynamics: An Advanced Introduction with OpenFOAM® and Matlab*. Springer Cham, 2015, doi:10.1007/978-3-319-16874-6.

[76] The MathWorks, Inc., "ode15s - solve stiff differential equations and daes," 2023-01-04. [Online]. Available: https://de.mathworks.com/help/matlab/ref/ode15s.html

[77] J. Hofele, J. M., G. Link, and J. Jelonnek, "Dielectric monitoring of the PAN fiber stabilization process," in *17th International Conference on Microwave and High Frequency Heating (Ampere)*, September 2019, pp. 365–372, doi:10.4995/Ampere2019.2019.9788.

[78] SGL Carbon, "PANOX PAN-Fasern," 2021-11-30. [Online]. Available: https://www.sglcarbon.com/loesungen/material/panox-oxidierte-pan-fasern/

[79] D. Veit, *Fibers*. Springer Cham, 2023, doi:0.1007/978-3-031-15309-9.

[80] J. Hofele, G. Link, and J. Jelonnek, "Dielectric measurements of PAN precursor and stabilized fibers," in *2020 German Microwave Conference (GeMiC)*, March 2020, pp. 192–195.

[81] A. Sihvola, *Electromagnetic Mixing Formulas and Applications*, 1999, doi:10.1049/PBEW047E.

[82] A. Sihvola, "Homogenization principles and effect of mixing on dielectric behavior," *Photonics and Nanostructures - Fundamentals and Applications*, vol. 11, no. 4, pp. 364–373, 2013, doi:10.1016/j.photonics.2013.01.004.

[83] I. The MathWorks, "Matlab r2019b," 2021-11-30. [Online]. Available: https://de.mathworks.com/products/matlab.html

[84] G. Roussy, A. Mercier, J.-M. Thiebaut, and J.-P. Vaubourg, "Temperature runaway of microwave heated materials: Study and control," *Journal of Microwave Power*, pp. 47–51, 1985, doi:10.1080/16070658.1985.11720279.

[85] J. Wang, L. Hu, C. Yang, W. Zhao, and Y. Lu, "Effects of oxygen content in the atmosphere on thermal oxidative stabilization of polyacrylonitrile fibers:," *RSC Adv.*, vol. 6, 08 2016, doi:10.1039/C6RA15308A.

[86] Mician GmbH, "μwave wizard," 2021-11-30. [Online]. Available: https://www.mician.com/products/

[87] C. S. SUITE, "The simulation method," 09.12.2022. [Online]. Available: http://www.mweda.com/cst/cst2013/advanced/the_simulation_method.htm

[88] M. Engler, “Implementation of a flexible scattering matrix code for the design and optimization of circular waveguide components,” Master thesis, Karlsruhe Insitute of Technology (KIT), 2018.

[89] J. Hofele, M. Engler, G. Link, and J. Jelonnek, “Combination of scattering matrix code and process model to optimize a microwave applicator suitable for the stabilization phase during the production of PAN fibers,” in *14th German Microwave Conference (GeMiC)*, May 2022, pp. 232–235.

[90] J. M. Neilson, P. E. Latham, M. Caplan, and W. G. Lawson, “Determination of the resonant frequencies in a complex cavity using the scattering matrix formulation,” *IEEE Transactions on Microwave Theory and Techniques*, vol. 37, no. 8, pp. 1165–1170, Aug. 1989, doi:10.1109/22.31074.

[91] T. Itoh, *Numerical Techniques for Microwave and Millimeter-Wave Passive Structures*. John Wiley & Sons, Hoboken, 1989.

[92] The MathWorks, Inc., “What is the genetic algorithm?” 2022-12-09. [Online]. Available: https://de.mathworks.com/help/gads/what-is-the-genetic-algorithm.html

[93] Y. Xue, J. Liu, and J. Liang, “Correlative study of critical reactions in polyacrylonitrile based carbon fiber precursors during thermal-oxidative stabilization,” *Polymer Degradation and Stability*, vol. 98, no. 1, pp. 219–229, 2013.

[94] O. Lab, “Peak analysis,” 2022-01-05. [Online]. Available: https://www.originlab.com/index.aspx?go=products/origin/dataanalysis/peakanalysis

[95] Anritsu, “Power meters and power sensors ma2400xa,” 2023-03-01. [Online]. Available: https://dl.cdn-anritsu.com/en-us/test-measurement/files/Brochures-Datasheets-Catalogs/datasheet/11410-00423M.pdf

[96] V. Ramopoulos, “Energy-efficient, scalable and modular industrial microwave applicator for high temperature alkaline hydrolysis of PET,” Doctoral thesis, 2019, Karlsruhe Institute of Technology (KIT).

Acknowledgment

"It takes a whole village to raise a child." African proverb

I think this proverb also fits very well with any Ph.D. project. My Ph.D. would not have been possible without many people who have supported me in various ways. I greatly appreciate every form of support I have received, because each part fits into the overall Ph.D. mosaic and only as a whole can the mosaic shine. Not all people accompany you the whole way on your promotion, and yet they have also supported you. Please know, that I am thankful for all of you. I want to show my gratitude for some individuals who help me and my Ph.D. in extraordinary ways in the following.

I started my Ph.D. journey as research assistant at the Institute for Pulsed Power and Microwave Technology (IHM) at the Karlsruhe Institute of Technology (KIT). Prof. Dr.-Ing. John Jelonnek gave me a home for my research on material processing with microwaves and guided my towards the final thesis. His enthusiasm for research helped my move forward. Thank you, for your continued support and valuable input not only concerning my work and research direction but also for the valuable life lessons!
I would like to sincerely thank my group leader Dr. Guido Link for his help and his constructive comments during group meetings or the review of my papers and the final thesis.

My time at the institute would not have been the same without my Ph.D. colleagues, thanks to Dr. Vasileios Ramopoulos, Dominik Neumaier, Dr. Tobias Ruess, Dr. Alexander Marek, Benjamin Ell, Moritz Engler, Dr. Sebastian Ruess, Lukas Feuerstein, Max Vöhringer, Lucas Silberer, Laurent Krier, Dr. Parth Kalaria and Dr. Chuanren Wu, I had always someone to talk to about my ideas and ask how-to-questions. I will always value our time together at the institute. More than warm thanks to you all!

As my Ph.D. topic includes a lot of experiments, I had tremendous help building and reshaping the experimental setups from Volker Nuss and Thomas Seitz. The mechanical and electrical workshop of the IHM, particularly Kai Schäfer, Alexander Sivkovich, Davide Quattrocchi, Kevin Paulus and Klaus Baumann manufactured individual components of the setups. My experimental setups were possible thanks to you. I thank you for your ideas, time and help.

Many discussions shaped my work. They would not have been possible without my colleagues. Among others, I thank Prof. Dr. rer. nat. Dr. h.c. Manfred Thumm, Dr. Sergey Soldatov, Dr. Nanya Li for their time and support. Sincere thanks also to Prof. Dr.-Ing. Ralf Moos for volunteering as co-referee of this thesis. Thanks to Martina Huber and Melanie Mai, I always had someone to count on for administrative (and Zumba) support. As my time at the institute is completed, I would like to thank all the IHM colleagures for the good working atmosphere at the institute.

Even though my time at the institute was very impactful for my Ph.D. , there are also a lot of persons outside the institute who gave me moral support and helped me become the person I am today. Thank you Petra Fürst for teaching me NLP. My friends from all stages of my life where also there for me and accepted my unwillingness to answer any questions on when my Ph.D. will be finished. Thank you for our ongoing journey through life! And finally, I could not have done it without the relentless support of my family. Your belief in me is truly inspirational, my deepest gratitude for believing in my endurance, thank you so much!

KARLSRUHER FORSCHUNGSBERICHTE AUS DEM
INSTITUT FÜR HOCHLEISTUNGSIMPULS- UND MIKROWELLENTECHNIK
(ISSN 2192-2764)

Band 1 MATTHIAS BERINGER
Design Studies towards a 4 MW 170 GHz Coaxial-Cavity Gyrotron.
ISBN 978-3-86644-663-2

Band 2 JENS FLAMM
Diffraction and Scattering in Launchers of
Quasi-Optical Mode Converters for Gyrotrons.
ISBN 978-3-86644-822-3

Band 3 MATTIA DEL GIACCO
Investigation of Fretting Wear of Cladding Materials in Liquid Lead.
ISBN 978-3-86644-960-2

Band 4 AMITAVO ROY CHOUDHURY
Investigations of After Cavity Interaction in Gyrotrons
Including the Effect of Non-uniform Magnetic Field.
ISBN 978-3-7315-0129-9

Band 5 MICHAEL BETZ
The CERN Resonant WISP Search (CROWS).
ISBN 978-3-7315-0199-2

Band 6 ANDREAS SCHLAICH
Time-dependent spectrum analysis of high power gyrotrons.
ISBN 978-3-7315-0375-0

Band 7 DHIDIK PRASTIYANTO
Temperature- and Time-Dependent Dielectric Measurements
and Modelling on Curing of Polymer Composites.
ISBN 978-3-7315-0424-5

Band 8 YIMING SUN
Adaptive and Intelligent Temperature Control of Microwave
Heating Systems with Multiple Sources.
ISBN 978-3-7315-0467-2

Die Bände sind unter www.ksp.kit.edu als PDF frei verfügbar oder als Druckausgabe bestellbar.

Band 9 JIANGHUA ZHANG
Influence of Emitter surface roughness and Emission inhomogeneity on Efficiency and stability of high power Fusion gyrotrons.
ISBN 978-3-7315-0578-5

Band 10 ANTON MALYGIN
Design and Experimental Investigation of a Second Harmonic 20 kW Class 28 GHz Gyrotron for Evaluation of New Emitter Technologies.
ISBN 978-3-7315-0584-6

Band 11 JOACHIM FRANCK
Systematic Study of Key Components for a Coaxial-Cavity Gyrotron for DEMO.
ISBN 978-3-7315-0652-2

Band 12 PARTH CHANDULAL KALARIA
Feasibility and Operational Limits for a 236 GHz Hollow-Cavity Gyrotron for DEMO.
ISBN 978-3-7315-0717-8

Band 13 CHUANREN WU
Conceptual Studies of Multistage Depressed Collectors for Gyrotrons.
ISBN 978-3-7315-0934-9

Band 14 MARTIN HOCHBERG
A high-voltage pulsed power modulator for fast-rising arbitrary waveforms.
ISBN 978-3-7315-0958-5

Band 15 SEBASTIAN RUESS
Pushing the KIT 2 MW Coaxial-Cavity Short-Pulse Gyrotron Towards a DEMO Relevant Design.
ISBN 978-3-7315-1024-6

Band 16 VASILEIOS RAMOPOULOS
Energy-efficient, scalable and modular industrial microwave applicator for high temperature alkaline hydrolysis of PET.
ISBN 978-3-7315-1099-4

Band 17 ALEXANDER MAREK
New Type of sub-THz Oscillator and Amplifier Systems Based on Helical-Type Gyro-TWTs.
ISBN 978-3-7315-1250-9

Band 18 TOBIAS RUESS
A First 2 MW-Class (136)/170/204 GHz Multi-Frequency Gyrotron Pre-Prototype for DEMO: Design, Construction and Key Components Verification.
ISBN 978-3-7315-1309-4

Band 19 FABIAN WILDE
Automated Mode Recovery and Electronic Stability Control for Wendelstein 7-X Gyrotrons.
ISBN 978-3-7315-1160-1

Band 20 JULIA HOFELE
Multi-Physics Modelling towards the Stabilization of PAN Fibers with Microwaves Based on Experimental Data.
ISBN 978-3-7315-1350-6

Karlsruher Forschungsberichte aus dem Institut für Hochleistungsimpuls- und Mikrowellentechnik

Herausgeber: Prof. Dr.-Ing. John Jelonnek

High energy demand is one of the major reasons for the high production costs of carbon fibers. One possible option to decrease the energy demand during the production is to use microwave heating instead of conventional convective heating. In this work, steps towards a microwave assisted process during the stabilization phase are presented. In-situ dielectric measurements are performed as basis for the understanding of the microwave – material interaction. As chemical reactions are taking place to transform the fiber, a reaction kinetics model is setup in connection to the dielectric loss. This allows to calculate the stabilization degree and fiber temperatures ahead of the experiments, leading to a basic understanding of the needed parameter ranges in order to set up a stable process. The findings allow to design a custom-made applicator for lab scale production tests.

Julia Hofele received the B. Sc. degree in Medical Engineering form the Friedrich-Alexander University Erlangen – Nürnberg (FAU) in 2014 and the M.Sc. in Electrical Engineering and Information Technology from Karlsruhe Institute of Technology (KIT) in 2017. In 2017, she joined the Institute for Pulsed Power and Microwave Technology (IHM), as a research assistant until 2022. Julia Hofele received the Dr.-Ing. degree in Electrical Engineering and Information Technologies in 2024.

ISSN 2192-2764
ISBN 978-3-7315-1350-6